

**BACHELOR THESIS IN  
AERONAUTICAL ENGINEERING  
15 CREDITS, BASIC LEVEL 300**

**Aerodynamic Investigation of Air Inlets on Aircrafts with  
Application of Computational Fluid Dynamics**

Author: **Marcus Lejon**

Report code: MDH.IDT.FLYG.0233.2011.GN300.15HP.Ae



## Abstract

Air inlets in some form are used on all commercial airliners today. The type of air inlet investigated in this report is a NACA inlet submerged into a surface. This surface is within this thesis a test section wall of a wind tunnel. The considered wind tunnel is TWG in Göttingen (Germany) that operates in transonic speeds. Submerged inlets have the main advantage of low aerodynamic drag from the inlet itself. The importance of reducing drag, and the attention given to this subject is increasing as fuel prices rise as well as public awareness of environmental impact by all of us.

The outcome of this thesis contributes to the government-funded project ECOCENTS which deals with the design of innovative new aircraft cooling systems and the detailed flow analysis of these systems. This thesis was carried out at the company Airbus in Bremen, Germany.

The main objective of this report was the evaluation of the ram pressure efficiency of four different ramp angles of a NACA inlet and the estimation of the drag caused by these geometries with the use of Computational Fluid Dynamics (CFD). The flow solver used was TAU, a Reynolds-Averaged Navier-Stokes (RANS) solver developed by the German Aerospace Center (DLR). The inlet consisted of one ramp section where the ramp angle was fixed at 7 degrees, and a second variable ramp section. The following different angles were investigated: 4, 7, 10 and 15 degrees. These configurations were evaluated at a velocity of Mach 0.8 and a Reynolds number of  $10 \cdot 10^6$ . The ramp angle of 7 degrees was evaluated at two additional velocities (Mach 0.73 and Mach 0.87) and at two additional Reynolds numbers ( $5 \cdot 10^6$  and  $15 \cdot 10^6$ ) at Mach 0.8.

The inlet efficiency outcome of this study was located between two other investigations. The results of this RANS computation predicted a higher total pressure at the inlet throat plane compared to a previous CFD investigation where a different RANS solver at the same geometry was used. In comparison to an estimation method mainly based on experimental data (ESDU method), the recent study showed a lower total pressure at the inlet throat plane. The aerodynamic drag that arised by the presence of the inlet system was calculated within this thesis to be higher than the outcome of the experimental data based (ESDU) method.

The advantage of using a NACA type inlet was observed to be highly related to the ramp angle. Vortices are originated and develop along the edges of the intake ramp walls. These two vortices help to transport higher energy flow from the free stream into the inlet and therefore reduce the boundary layer thickness in the inlet region. For lower mass flows (0.10 - 0.20 kg/s) a ramp angle of 7 degrees was seen to be preferred in view of ram pressure efficiency. At a higher mass flow (0.25 kg/s) the 10 degrees ramp angle was preferred, followed by the 15 degrees ramp angle at the highest investigated mass flows (0.30 - 0.35 kg/s). In view of drag, the lowest ramp angle possible for a given mass flow was seen to be most advantageous.

Future work on this subject will include simulation of an inlet in combination with a heat exchanger and a ram air outlet. This arrangement will be the same as in the investigation at the TWG test campaign and therefore comparable. The difference in outcome of the separate CFD analysis was discussed within this investigation but could not be completely cleared.



## Sammanfattning

Luftintag av något slag används på alla kommersiella trafikflygplan idag. Den typ av luftintag som undersöks i den här rapporten är ett NACA luftintag nedsänkt i en plan yta. I det här examensarbetet är den här ytan en vägg i en vindtunnel. Den aktuella vindtunneln för den här studien är TWG i Göttingen (Tyskland) som kan simulera luftflöde i det transoniska området. Nedsänkta luftintag har fördelen med ett lågt luftmotstånd orsakat av själva luftintaget. Vikten av att reducera luftmotstånd ökar i takt med stigande bränslepriser och ökad medvetenhet om vår inverkan på miljön.

Resultaten från det här examensarbetet bidrog till det myndighetsfinansierade projektet ECOCENTS som handlar om design av innovativa nya kylsystem för flygplan samt ingående analyser av luftflödet i dessa system. Det här examensarbetet utfördes på företaget Airbus i Bremen, Tyskland.

Det huvudsakliga målet med den här rapporten var att göra en utvärdering av effektiviteten hos fyra olika vinklar av den ramp som leder ner till luftintaget samt luftmotståndet som orsakas av dessa med hjälp av Computational Fluid Dynamics (CFD). Det program som användes för att utföra beräkningarna heter TAU och är en Reynolds-Averaged Navier-Stokes lösare utvecklad av German Aerospace Center (DLR). Luftintaget består av en rampsektion där vinkeln mellan rampen och ytan som luftintaget är nedsänkt i är konstant 7 grader, och en sektion där vinkeln kan ändras. Följande vinklar undersöktes: 4, 7, 10 och 15 grader. Dessa konfigurationer utvärderas vid en hastighet av Mach 0.8 och ett Reynolds tal på  $10 \cdot 10^6$ . Rampen med en vinkel på 7 grader utvärderades vid ytterligare två hastigheter (Mach 0.73 och Mach 0.87) och ytterligare två Reynolds tal ( $5 \cdot 10^6$  och  $15 \cdot 10^6$ ) i Mach 0.8.

Effektiviteten hos luftintaget beräknades i den här studien till att ligga mellan två andra undersökningar. Resultaten från RANS-beräkningar uppskattade ett högre totaltryck vid "inlet throat plane" jämfört med en tidigare undersökning gjord på samma geometri med ett annat program för RANS-beräkningarna. I jämförelse med en metod baserad på experimentella resultat (ESDU metoden), så visade studien i det här examensarbetet på ett lägre totaltryck. Det luftmotstånd som uppstår på grund av luftintaget och tillhörande komponenter av luftintagssystemet beräknas i det här arbetet till att vara högre än den uppskattning som gjordes baserad på experimentella data (ESDU).

Fördelen med att använda ett NACA luftintag observerades vara nära relaterad till rampvinkeln hos luftintaget. Luftvirvlar bildas och utvecklas längs de övre kanterna till väggarna av rampen. De här två luftvirvlarna hjälper till att föra luft med högre energi från friströmmen ner i luftintaget och därför även reducera tjockleken hos det gränsskikt som finns i luftintaget. För låga massflöden (0.10 - 0.20 kg/s) så var en konstant 7 graders rampvinkel den optimala konfigurationen med avseende på effektivitet. Vid ett högre massflöde (0.25 kg/s) så presterade 10 graders konfigurationen bäst, följt av konfigurationen med en 15 graders rampvinkel för de högsta massflödena som undersöktes (0.30 - 0.35 kg/s). Med avseende på luftmotstånd så var alltid en så liten vinkel som möjligt det mest fördelaktiga alternativet.

Framtida arbete kring det här ämnet kommer att involvera simulering av ett luftintag i kombination med en värmeväxlare och ett luftutblås. Det här arrangementet kommer att vara desamma som undersöks vid TWG och resultaten är därför jämförbara. Skillnader i resultaten från de olika CFD analyserna diskuterades men kunde inte redas ut helt i den här undersökningen.



Date: **8 July 2011**

Carried out at: **Airbus Operations GmbH**

Supervisor and Examiner at MDH: **Gustaf Enebog**  
Lecturer and Program Coordinator of the  
Bachelor Program in Aeronautical Engineering  
School of Innovation, Design and Engineering  
Mälardalen University  
Email: gustaf.enebog@mdh.se

Advisor at Airbus: **Udo Krause**  
Research Engineer in Aircraft Aerodynamic Design  
Aerodynamics Department - EGACAB  
Airbus Operations GmbH  
Email: udo.krause@airbus.com





## **Acknowledgements**

I would like to thank Udo Krause for all his help with this thesis and for making me feel very welcome to Germany and the Airbus company.

Thank you to Bruno Stefes who shared his expertise on intakes and aerodynamics in general.

Thank you to everyone at the Aerodynamics department at Airbus in Bremen for being very friendly and giving me a good place to perform my studies.

Thank you to Linda van Leeuwen, my partner, who has been very supportive during this undertaking.



# Contents

<b>Abbreviations</b>	<b>viii</b>
<b>Symbols and Subscripts</b>	<b>ix</b>
<b>List of Tables</b>	<b>x</b>
<b>List of Figures</b>	<b>xi</b>
<b>1 Introduction</b>	<b>1</b>
1.1 Background . . . . .	1
1.1.1 Project ECOcents . . . . .	2
1.2 Purpose . . . . .	3
1.3 Scope of work . . . . .	5
<b>2 Theory</b>	<b>7</b>
2.1 Boundary Layer Theory . . . . .	7
2.2 Drag . . . . .	8
2.3 Flight Mechanics . . . . .	9
2.4 Ram Pressure Efficiency . . . . .	10
2.5 Ram Recovery Ratio . . . . .	10
2.6 Mass Flow Ratio . . . . .	10
2.7 Navier-Stokes Equations . . . . .	11
2.8 Reynolds-Averaged Navier-Stokes Equations . . . . .	12
2.9 Spatial Discretisation . . . . .	13
2.9.1 Computational Grids . . . . .	14
2.9.2 Discretisation Methods . . . . .	15
2.9.3 Central and Upwind Schemes . . . . .	15
2.10 Time Discretisation . . . . .	16
<b>3 Methodology</b>	<b>17</b>
3.1 Preliminary Studies . . . . .	17
3.1.1 Inlets . . . . .	17
3.1.2 Flush Inlets . . . . .	17
3.1.3 NACA Curved-Divergent Inlet . . . . .	19
3.1.4 Design Parameters . . . . .	21
3.1.5 Inlet Drag . . . . .	24
3.1.6 Plenums . . . . .	26
3.2 Geometry Preparation . . . . .	27
3.3 Mesh Generation . . . . .	29
3.4 Numerical Computation . . . . .	33
3.5 Post Processing . . . . .	37
3.6 Empirical Method Analysis . . . . .	39
<b>4 Results and Discussion</b>	<b>41</b>
4.1 Pressure and Mach number Analysis . . . . .	41
4.2 Boundary Layer Analysis . . . . .	43
4.2.1 Ramp wall edges . . . . .	49
4.3 Ram Pressure Efficiency . . . . .	50

4.4	Ram Recovery Ratio . . . . .	53
4.5	Drag investigation . . . . .	54
4.6	Internal Air Duct After the Plenum . . . . .	61
4.7	Analysis of the Vortices Formed by the NACA Inlet . . . . .	63
4.8	Conclusions and Recommendations of Future Work . . . . .	67
<b>References</b>		<b>70</b>
<b>A APPENDIX</b>		<b>71</b>
A.1	Computational Models and Tools . . . . .	71
A.1.1	CENTAUR . . . . .	71
A.1.2	TAU . . . . .	75
A.1.3	Tau.BL . . . . .	75
A.1.4	CATIA . . . . .	76
A.1.5	Tecplot 360 . . . . .	76
A.1.6	RAMAIR . . . . .	76
A.2	Figures . . . . .	77
A.2.1	Introduction . . . . .	77
A.2.2	Measurements . . . . .	79
A.2.3	Geometry Preparation . . . . .	84
A.2.4	Mesh Generation . . . . .	86
A.2.5	Post Processing . . . . .	88
A.2.6	Results and Discussion . . . . .	96
A.3	Lessons Learned and Best Practice Settings . . . . .	101
A.3.1	Mesh Generation . . . . .	101
A.3.2	Numerical Computation . . . . .	110
A.4	Calculations . . . . .	111
A.5	Tables . . . . .	114
A.6	Transonic Wind tunnel Göttingen . . . . .	116
A.7	Input Files . . . . .	117
A.7.1	CENTAUR . . . . .	117
A.7.2	TAU . . . . .	118
A.7.3	Others . . . . .	131

## Abbreviations

<b>BL</b>	Boundary Layer
<b>CAD</b>	Computer Aided Design
<b>CATIA</b>	Computer Aided Threedimensional Interactive Application (a commercial CAD software)
<b>CFD</b>	Computational Fluid Dynamics
<b>CSM</b>	Computational Solid Mechanics
<b>DLR</b>	German Aerospace Center
<b>ECOCENTS</b>	Efficient Cooling Center for Aircraft Systems
<b>ESDU</b>	Engineering Sciences Data Unit
<b>FOD</b>	Foreign Object Damage
<b>NACA</b>	National Advisory Committee for Aeronautics
<b>NS</b>	Navier-Stokes (equations)
<b>NWB</b>	Low-Speed Wind tunnel Braunschweig
<b>RANS</b>	Reynolds-Averaged Navier-Stokes (equations)
<b>TWG</b>	Transonic Wind tunnel Göttingen

## Symbols and Subscripts

### Dimensionless Coefficients

$C_D$	Drag coefficient
$C_L$	Lift coefficient
$c_p$	Pressure coefficient
$c_v$	Specific heat at constant volume
dc	Drag count. 1 drag count is equal to 0.0001 $C_D$

### Roman Symbols

$A_1$	Inlet throat area
c	The fuel consumption
$c_t$	The thrust-specific fuel consumption
D	The drag expressed in Newton
e	Internal energy due to random molecular motion
L	The lift expressed in Newton
$P_{T0}$	Free stream total pressure
$P_{T1}$	Average total pressure at the inlet throat plane
$p_0$	Free stream static pressure
R	The specific gas constant
$q_0$	Free stream dynamic pressure
S	The wing area of an aircraft
T	Flow temperature
$V_0$	Free stream velocity
$V_1$	Inlet throat flow velocity
$W_0$	The weight of an aircraft with full fuel tanks
$W_1$	The weight of the aircraft with empty fuel tanks
$y^+$	Non-dimensional distance from a surface

### Greek Symbols

$\alpha$	Angle of attack
$\delta$	The boundary layer thickness
$\eta$	Ram pressure efficiency
$\eta_p$	Propeller efficiency
$\rho_0$	Free stream flow density
$\rho_1$	Inlet throat flow density
$\tau_w$	The shear friction at the surface of a solid
$\theta$	Boundary layer displacement thickness

## List of Tables

Table	Description	Page
3.1	Ramp coordinates for NACA curved-divergent planform .....	20
3.2	Inlet drag and ram pressure efficiency estimated with the help of ESDU paper 86002 .....	39
A.4.1 -		
A.4.2	Ram pressure efficiency calculation tables .....	108-109
A.4.3 -		
A.4.8	Inlet drag calculation tables .....	109-110
A.5.1	Geometry for different ramp angles .....	111
A.5.2	Diffuser angles for different ramp angles .....	112

## List of Figures

Figure	Description	Page
1.1	Air cooling and supply system on an aircraft body .....	1
1.2	ECOCENTS Logo .....	2
1.3	NACA type flush inlet .....	3
1.4	Cross section of an inlet .....	3
2.1	Velocity profile through a boundary layer .....	7
2.2	Boundary layer growth along a flat plate .....	7
2.3	Forces .....	8
2.4	Balance of Forces for Steady Level Flight .....	9
2.5	Flush Inlet Denotations .....	10
2.6	Rectangular grid segment .....	14
2.7	Unstructured grid segment .....	14
3.1	Scoop inlet .....	17
3.2	Flush inlet .....	17
3.3	Flush inlets with convergent walls, divergent walls and parallel walls respectively	18
3.4	Vortices formed along the edges of a ush inlet with divergent walls .....	19
3.5	NACA curved-divergent planform .....	20
3.6	NACA curved-divergent inlet .....	20
3.7	Arrangement of the submerged NACA inlet in Reference [14] .....	21
3.8	Resulting change of the ramp from a change of ramp angle .....	22
3.9	Surface parallel to the free stream and a ramp section .....	23
3.10	Deflectors .....	24
3.11	The effect of mass flow ratio on the entry streamtube .....	25
3.12	Plenum classic .....	26
3.13	Plenum base .....	26
3.14	Original wind tunnel geometry .....	27
3.15	The wind tunnel geometry with an extension aft of the test section .....	27
3.16	The boundary of the module .....	28
3.17	The module ready to be imported into CENTAUR .....	28
3.18	The inlet system with coordinate axis .....	29
3.19	Illustration of the extension made to the duct prior to the outlet .....	29
3.20	Geometrical sources in the test section of the wind tunnel .....	30
3.21	Surface mesh at the inlet .....	32
3.22	The contour of the prismatic layers inside the inlet .....	31
3.23	The mesh at $x = 135$ .....	32
3.24	The mesh at $x = 180$ .....	32
3.25	The wind tunnel geometry with extensions .....	33
3.26	Computational grid at the additional outlet .....	34
3.27	Velocity profiles at the additional outlet .....	34
3.28	Schematic set-up of the numerical wind tunnel simulation .....	34
3.29	Close-up of the mesh at the wind tunnel test section .....	35
3.30	Side view of the wind tunnel showing the pressure distribution in Tecplot 360 ...	37
3.31	Side view of the wind tunnel showing the Mach number in Tecplot 360 .....	37
3.32	Residual plot for the clean wind tunnel setup .....	38
3.33	Residual plot for the wind tunnel with an inlet .....	38



<b>Figure</b>	<b>Description</b>	<b>Page</b>
4.1	Side view in the symmetry plane of an inlet showing the Mach number .....	41
4.2	Side view in the symmetry plane of an inlet showing the Mach number .....	41
4.3	Side view in the symmetry plane of an inlet showing the static pressure .....	42
4.4	Side view in the symmetry plane of an inlet showing the total pressure .....	42
4.5	Top view of the inlet with the positions of the cuts shown in Figure 4.6 - 4.8 ....	43
4.6	Side view in the symmetry plane of the inlet with streamlines. Cut 1 .....	43
4.7	Side view in the symmetry plane of the inlet with streamlines. Cut 2 .....	43
4.8	Side view in the symmetry plane of the inlet with streamlines. Cut 3 .....	43
4.9	Side view of the inlet with points showing the positions investigated in Tau BL and Tecplot 360 .....	44
4.10	Velocity profiles 260 mm prior to the inlet .....	45
4.11	Velocity profiles 50 mm prior to the inlet .....	46
4.12	Velocity profiles 15 mm aft of the inlet lip .....	46
4.13	Detailed velocity profile 15 mm aft of the inlet lip with the inlet present .....	47
4.14	Velocity profiles 285 mm aft of the inlet lip .....	48
4.15	Velocity profile inside the inlet at the inlet throat plane .....	48
4.16	Streamtraces placed at the NACA submerged inlet from a Tau BL solution as seen in Tecplot 360 .....	49
4.17	Ram pressure efficiency comparison at Mach 0.2 for different turbulence models .	50
4.18	Ram pressure efficiency comparison for different estimation methods .....	51
4.19	Ram pressure efficiency comparison for different mass flows .....	52
4.20	Ram pressure efficiency for different inlet ramp angles in relation to the mass flow .....	52
4.21	Ram recovery ratio for different inlet ramp angles in relation to the mass flow ...	53
4.22	Naming of the different inlet system assembly parts in this thesis .....	54
4.23	Naming of the wind tunnel test section parts in this thesis .....	54
4.24	Drag comparison for the 7 degrees ramp angle configuration .....	55
4.25	Drag comparison for the different ramp angles at Mach 0.8 .....	56
4.26	Side view in the symmetry plane of an inlet showing the Mach number .....	56
4.27	Drag comparison for the different angles for the complete inlet system at Mach 0.8 .....	57
4.28	Drag comparison for 7 degrees ramp angle for the complete inlet system at different Mach numbers .....	58
4.29	Drag comparison for 7 degrees ramp angle for complete inlet system at different Reynolds numbers .....	59
4.30	Drag contribution of different components of the inlet system and increase of drag on surrounding floor panels. Percentage of total drag. ....	60
4.31 -		
4.39	The inlet system and pressure plots in the inviscid section .....	61-62
4.40	Plot of the vorticity at x-coordinate 135 for an inlet with 15 degrees ramp angle. Streamtraces showing surrounding flow entering the inlet. ....	63
4.41	ISO Pressure-surface 73250 Pa. Mach 0.8. Reynolds number: 10e6 .....	64
4.42 -		
4.45	Vorticity plots for 7 degrees ramp angle at Mach 0.8 and a mass flow of 0.20 kg/s	64
4.46	Inlet vorticity gradient .....	64
4.47	Sideview of the inlet system with x-positions .....	64

<b>Figure</b>	<b>Description</b>	<b>Page</b>
A.1.1	Control volume borders on a triangle .....	72
A.1.2	Control volume borders on a quadrilateral .....	72
A.1.3	Control volume borders in a hexahedron .....	73
A.1.4	Control volume borders in a prism .....	73
A.1.5	Control volume borders in a tetrahedron .....	75
A.1.6	Control volume borders in a pyramid .....	74
A.1.7	Streaklines and the pressure distribution is visualised on a 2D view of a cylinder	76
A.2.1	Example of an air cooling and supply system .....	77
A.2.2	Air cooling and supply system inside the belly fairing of an airplane .....	78
A.2.3	Measurements of the NACA submerged inlet investigated in this report .....	79
A.2.4	X-coordinates at different locations of the inlet .....	79
A.2.5	Side view of the wind tunnel geometry with measurements in millimeters .....	80
A.2.6	Side view of the wind tunnel test section with measurements in millimeters .....	80
A.2.7	Side view of the wind tunnel test section with measurements in millimeters .....	81
A.2.8	Top view of the wind tunnel test section with measurements in millimeters .....	81
A.2.9	Measurements in millimeters of the additional inlet geometry which was later removed .....	82
A.2.10	Measurements in millimeters of the original and additional inlet geometry which was later removed .....	83
A.2.11	Part of the wind tunnel geometry prior to CAD Cleaning .....	84
A.2.12	Part of the wind tunnel geometry after CAD Cleaning had been performed .....	84
A.2.13 -		
A.2.16	Side view of the air inlet at different ramp angles as seen in CATIA .....	85
A.2.17	The prismatic layers getting chopped down in the vicinity of the corners of the duct at x-position 45. 7 degrees ramp angle. ....	86
A.2.18	Transition from triangular to hexahedral elements after the bend of the duct ...	86
A.2.19	The Prismatic layers prior to the inlet. 7 degrees ramp angle .....	86
A.2.20	The prismatic layers aft of the lip of the inlet .....	87
A.2.21	The prismatic layers in the extension with inviscid walls prior to the outlet .....	87
A.2.22 -		
A.2.31	Vorticity plots for an inlet with the variable inlet ramp angle set to 4 degrees ...	88
A.2.32 -		
A.2.39	Vorticity plots for an inlet with the variable inlet ramp angle set to 7 degrees ...	89
A.2.40 -		
A.2.47	Vorticity plots for an inlet with the variable inlet ramp angle set to 10 degrees .	90
A.2.48 -		
A.2.55	Vorticity plots for an inlet with the variable inlet ramp angle set to 15 degrees .	91
A.2.56 -		
A.2.65	Mach plots for an inlet with the variable inlet ramp angle set to 4 degrees .....	92
A.2.66 -		
A.2.75	Static pressure plots for an inlet with the variable inlet ramp angle set to 4 degrees .....	93
A.2.76 -		
A.2.84	Mach plots for an inlet with the variable inlet ramp angle set to 7 degrees .....	94
A.2.85 -		
A.2.93	Static pressure plots for an inlet with the variable inlet ramp angle set to 7 degrees .....	95

<b>Figure</b>	<b>Description</b>	<b>Page</b>
A.2.94 -		
A.2.96	Solution span for the last 20 000 iterations. 7 degrees ramp angle. Mach 0.8. Mass flow: 0.10 kg/s .....	96-97
A.2.97	Ram recovery ratio comparison for the 7 degrees ramp angle at different Mach numbers .....	97
A.2.98	Ram recovery ratio comparison for the 7 degrees ramp angle at different Mach numbers .....	98
A.2.99	Ram pressure efficiency comparison for different mass flow ratios .....	98
A.2.100	Ram pressure efficiency comparison for different Mach numbers .....	99
A.2.101	Drag for the inlet with different ramp angles for different mass flow ratios .....	99
A.2.102	Drag for the inlet system with different inlet ramp angles for different mass flow ratios .....	100
A.3.1	The wind tunnel floor prior to the inlet with 35 prismatic layers .....	101
A.3.2	The wind tunnel floor prior to the inlet where 31 prismatic layers transitions to 28 prismatic layers .....	101
A.3.3	The wind tunnel floor aft of the inlet with 35 prismatic layers .....	101
A.3.4	The wind tunnel floor aft of the inlet where 28 prismatic layers transitions to 31 prismatic layers .....	102
A.3.5	Side view of the geometrical sources at the wind tunnel test section .....	102
A.3.6	The inlet system with coordinate axis .....	102
A.3.7	Side view of the sources prior to and aft of the inlet .....	104
A.3.8	Side view of the prismatic layers in the inlet for the 7 degrees constant ramp angle configuration as seen in Tecplot 360 .....	104
A.3.9	The iterative process of attaining the prismatic mesh settings inside the inlet ....	105
A.3.10	The inlet of the wind tunnel geometry. Sources shown in purple .....	106
A.3.11	Side view of the prismatic mesh at the bend of the internal duct .....	107
A.3.12	Bottom view of the prismatic mesh with no surface refinement in the corners as seen in Tecplot 360 .....	107
A.3.13	Side view of the prismatic mesh at the bend of the internal duct .....	107
A.3.14	Bottom view of the prismatic mesh with surface refinement in the corners as seen in Tecplot 360 .....	108
A.3.15	Bottom view of the prismatic mesh with surface refinement in the corners as seen in Tecplot 360 when generated with the modular meshing feature .....	108
A.3.16	Mesh comparison when using modular meshing .....	109
A.5.1	Cross section of the inlet and diffuser section .....	115



# 1 Introduction

## 1.1 Background

The cabin of a commercial aircraft needs to be pressurized at high altitudes in order to provide a comfortable and safe environment for the passengers inside. This pressurization is realized by taking pressurized air from the engines. When the pressure of the air is increased in the engines prior to the combustion chamber, a rise of temperature occurs. The air taken from the engines is often referred to as bleed-air and the temperature of this air is in the temperature region of around 200 degrees Celsius. This air needs to be cooled and this is achieved by air cooling systems. These air systems get their needed cold air by the use of so called RAM air inlets. These inlets supply air from the free stream outside of the aircraft to a heat exchanger where the air from the engine can be cooled. At a cruising altitude of 35 000 ft the surrounding air is approximately -55 degrees Celsius.

The overall need for air supply on an airplane can be divided into two parts:

- System needs (e.g. cooling, pressurization and air supply)
- Passenger needs (e.g. fresh air contribution and air conditioning)

An air inlet can protrude from the aircraft surface or be submerged into the aircraft body. A submerged inlet has in general lower aerodynamic drag than an inlet that protrudes from the surface of an aircraft and is therefore the most preferred design option to the flight industry.

An air inlet should ideally not decrease the total pressure of the air which enters and at the same time only give rise to a minimum amount of additional aerodynamic drag.

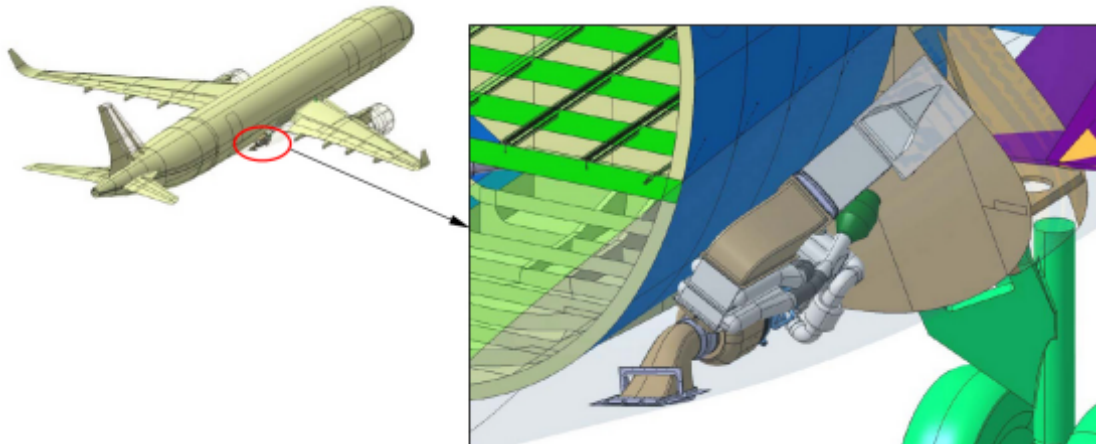


Figure 1.1

Air cooling and supply system on an aircraft body. Image courtesy of Airbus

### 1.1.1 Project ECOcents



Figure 1.2  
ECOcents Logo

This thesis contributes with its results to the government-funded project ECOcents. ECOcents stands for "Effizientes Cooling Center für Flugzeugsysteme" which translates into English as "Efficient Cooling Center for Aircraft Systems".

This project consists of two main research topics:

- Cooling center
- Cooling channel

*Cooling center* deals with the design of heat exchangers while *Cooling channel* deals with the inlet, outlet and channel design. Previous studies have been made on the design of the air inlet in connection to this project. The investigation carried out in this thesis is however the first detailed investigation of wind tunnel simulations in combination with air systems inlets using the RANS flow solver TAU developed by the German Aerospace Center (DLR).

## 1.2 Purpose

The purpose of this thesis is to investigate flow phenomenon on a NACA-type flush inlet. Main consideration will be done in view of inlet efficiency and aerodynamic drag.



Figure 1.3  
NACA type flush inlet. Figure from Reference [1]

A detailed study will be carried out on an inlet in combination with the Transonic Wind tunnel Göttingen (TWG) using Computational Fluid Dynamics. The study will analyse the effect of varying the ramp angle of the inlet. The initial ramp angle into the inlet is kept constant, and the angle for the second section of the inlet is varied. The feature of a varying ramp angle is something that already exist on commercial aircrafts manufactured by Airbus. The inlet throat area will change as a result of a change of the ramp angle.

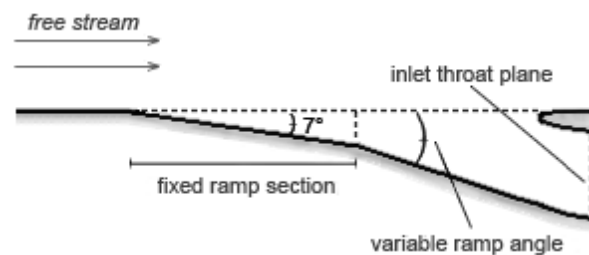


Figure 1.4  
Cross section of an inlet.

The variable ramp angle is adjusted to the system cooling needs and the ambient flight conditions. At high altitude a smaller angle is sufficient because of the very low temperature of air that enters the inlet. At lower altitudes where the temperature of the air is higher, the angle is increased to allow for a higher mass flow to secure sufficient cooling. It is important to note that in reality some additional consideration has to be taken for the change of density that follows from a change in altitude.

Four different cases will be investigated as a part of this thesis: 4, 7, 10 and 15 degrees. The ramp angle of 7 degrees will be investigated at three different Mach numbers:

- Mach 0.73
- Mach 0.8
- Mach 0.87

The same constant ramp angle of 7 degrees will be investigated for three different Reynolds numbers.

- Reynolds number:  $5 \cdot 10^6$
- Reynolds number:  $10 \cdot 10^6$
- Reynolds number:  $15 \cdot 10^6$

The three other angles will be investigated at a Reynolds number of  $10 \cdot 10^6$  and Mach 0.8. A comparison of the results obtained CFD results will be made with an empirical method analysis. Suggestions will be given for optimal arrangements of air inlets with regards to caused flow effects. The CFD investigation will be used to validate and support a wind tunnel campaign in TWG (DLR Göttingen) that is planned for October 2011.



### 1.3 Scope of work

- Study of literature relevant to the topic of the thesis. This includes presentations, books and technical reports on Computational Fluid Dynamics and Air Inlets.
- Familiarization with the tools necessary to achieve the objective (CATIA, CENTAUR, TAU, Tau.BL and Tecplot 360).
- Prepare the wind tunnel CAD geometry for the data export into the meshing software.
- Prepare a number of CAD models for the purpose of investigating different NACA air inlet ramp angles.
- Generate several computational grids.
- Setup of TAU boundary conditions and execute TAU calculations.
- Detailed analysis of the results.
- Give suggestions for optimal air inlet ramp angles.
- Make recommendations for future work.
- Write a thesis paper for the Degree of Bachelor of Science in Engineering.
- Hold a presentation in English on the results obtained for interested parties at Airbus site in Bremen, Germany.
- Hold a presentation in Swedish on the scope of this thesis and the results obtained at Mälardalen University in Västerås, Sweden.



## 2 Theory

### 2.1 Boundary Layer Theory

When studying air flow over a solid body it is appropriate to divide the analysis of the flow into two parts. Close to the surface of the solid body friction forces play an important part whereas further out into the free stream friction forces can be neglected. The idea is to treat the air flow close to a surface separately. This concept was first suggested in 1904 by a man named Ludwig Prandtl.

Due to the friction between the surface and the moving gas, the air flow closest to the surface will tend to adhere. This phenomenon is known as the no-slip condition. This is true for all fluids but for the purpose of this thesis we are mainly interested in the medium air. The velocity gradually increases further away from the surface and eventually reaches the free stream velocity, denoted as  $V_2$  in Figure 2.1.

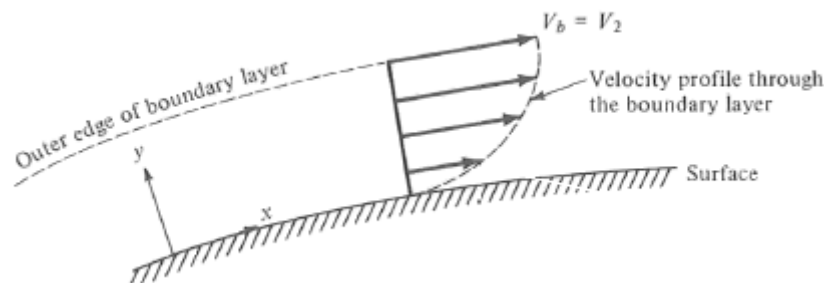


Figure 2.1

Velocity profile through a boundary layer. Figure from Reference [2]

The region in which this velocity gradient exist is called the boundary layer. The velocity reduction of the flow inside the boundary layer gives rise to shear friction  $\tau_w$  on the surface of the solid body. This shear friction is the source of a form of drag called skin friction drag.

The thickness of the boundary layer, denoted as  $\delta$ , is defined as the distance normal to the surface up to a point where the flow has reached 99% of the free stream velocity. Due to the effects of friction, the thickness of the boundary layer increases as the flow moves a distance over the surface and can attain a considerable thickness, e.g, at the end of a flat plate (Figure 2.2) or at the fuselage tail of an aircraft.

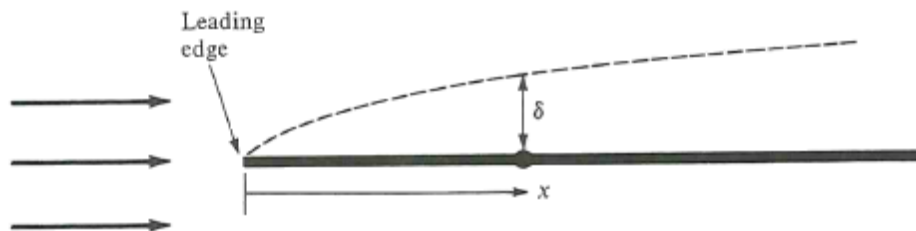


Figure 2.2

Boundary layer growth along a flat plate. Figure from Reference [2]

The boundary layer thickness is an important parameter to consider when placing an air inlet on a surface as this low-velocity, low energy boundary layer decreases the performance of the inlet.

## 2.2 Drag

Aerodynamic drag is the force acting parallel to the free stream on a body immersed in a moving fluid. All forces in aerodynamics have their origin in pressure distribution and shear stress distribution over the body surface. It is hence appropriate to divide the drag of a body into two categories, *pressure drag* and *skin friction drag*, depending on which one of these sources it has its physical origin. There are additional types of aerodynamic drag which play an important role at the overall aerodynamics of aircrafts: *interference drag*, *lift-induced drag* and *wave drag*. For aerodynamic design of air systems they might not be completely negligible but will not be regarded here in detail.

Shown in Figure 2.3 is an airfoil at an angle of attack  $\alpha$  to a free stream with velocity  $V_\infty$ . A lower pressure on the upper side of the airfoil than on the lower side will cause a resultant force  $R$  at the center of pressure.

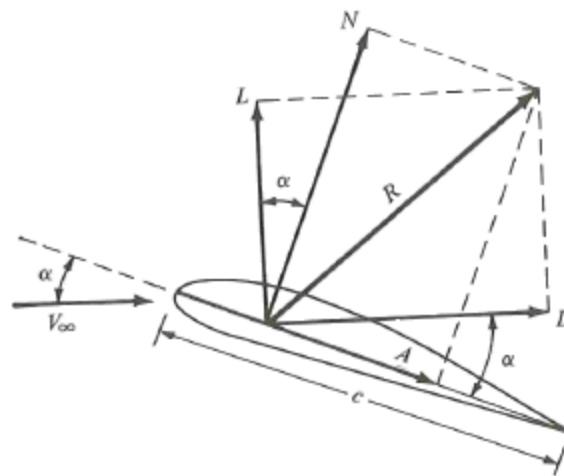


Figure 2.3  
Forces. Figure from Reference [3]

The component of the resultant force perpendicular to the free stream ( $L$ ) will be generating lift while the component parallel to the free stream ( $D$ ) will be acting as drag on the airfoil. In aeronautics the term  $C_D$  is often used which is given by the formula:

$$C_D = \frac{D}{q_0 S} \quad (1)$$

where  $D$  is the drag in Newton,  $q_0$  is the dynamic pressure in the free stream and  $S$  is an appropriate reference area. When speaking of drag inflicted by a separate component in relation to an airplane reference area it can be appropriate to talk about drag counts. One drag count is equal to  $1/10\,000 C_D$ .

### Pressure Drag

Pressure difference is a very potent force and the reason why an airplane can generate enough lift to fly. Pressure drag has its origin in a difference in pressure acting in the direction parallel to the onset flow.

An aerodynamic body such as a wing with a symmetrical airfoil placed in a free stream at an angle of attack of  $0^\circ$  will be subject to very little pressure drag. The predominant form of drag at

this angle of attack would be skin friction drag, but as  $\alpha$  is increased to a certain degree the flow will eventually separate at the trailing edge of the wing. The separation point will move further forward on the upper side of the wing with an increasing angle of attack. Flow separation alters the pressure distribution over the wing, lowering the pressure at the trailing edge and increasing the pressure at the leading edge resulting in a large increase in pressure drag.

### Skin Friction Drag

The skin friction drag is due to viscous effects on the surface of a body due to the presence of the boundary layer. The closer the flow gets to the surface, the more the motion of the flow is retarded by friction. An equal force in the opposite direction affects the surface of the solid body; this force is the skin friction drag. A larger surface area will give rise to a higher value of skin friction drag. A term used in the aircraft industry is *wetted area* which is the area in contact with the moving fluid and is often used as a reference area for skin friction drag.

## 2.3 Flight Mechanics

An aircraft which is flying at an altitude is subject to four forces: lift, weight, thrust and drag. To keep the same altitude over time the lift must be equal to the weight of the aircraft. For the aircraft to fly at constant speed, the thrust supplied by the engines must balance out the drag.

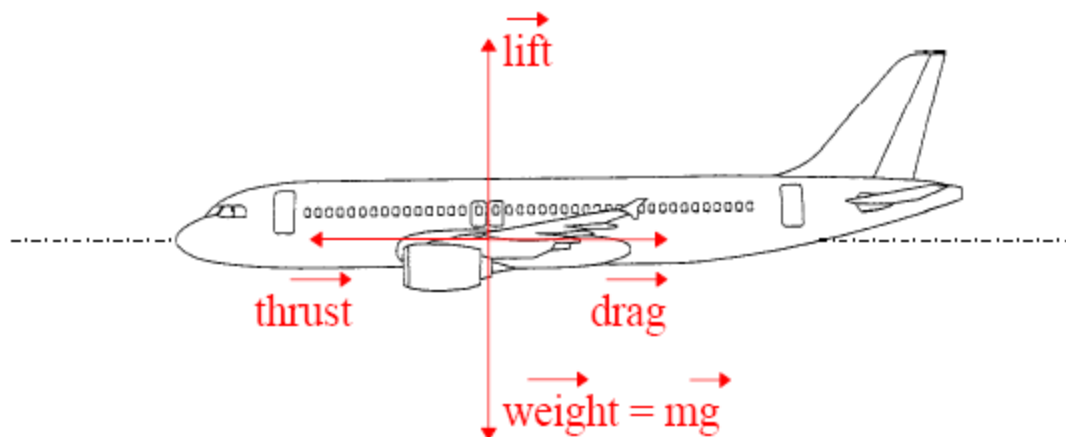


Figure 2.4

Balance of Forces for Steady Level Flight. Figure from Reference [4]

If the aircraft is subject to less aerodynamic drag, the thrust supplied by the engines can be reduced requiring less fuel. An airplane with a lowered fuel consumption can fly further with the same amount of fuel, alternatively carry more payload since the amount of fuel needed was decreased. The *Breguet range formulas* show this correlation:

*Breguet range formula - propeller driven airplane*

$$Range = \frac{\eta_p}{c} \frac{C_L}{C_D} \ln \frac{W_0}{W_1} \quad (2)$$

Where  $\eta_p$  is the propeller efficiency,  $c$  is the fuel consumption,  $C_L$  is the dimensionless lift coefficient,  $C_D$  is the dimensionless drag coefficient,  $W_0$  is the weight of an aircraft with full fuel tank and  $W_1$  is the weight of the aircraft with empty fuel tanks.

A lower value of the fuel consumption  $c$  will result in a longer range for the aircraft.

Breguet range formula - jet airplane

$$Range = 2\sqrt{\frac{2}{\rho_0 S} \frac{1}{c_t} \frac{C_L}{C_D}} (W_0 - W_1) \quad (3)$$

Where  $\rho_0$  is the density of the air in the free stream,  $S$  is the wing area and  $c_t$  is the thrust-specific fuel consumption.

A lower value of the thrust-specific fuel consumption  $c_t$  will also here result in a longer range for the aircraft.

## 2.4 Ram Pressure Efficiency

Ram pressure efficiency will be used throughout this thesis as an indicator to judge the effectiveness of an air inlet. The ram pressure efficiency is given by

$$\eta = \frac{P_{T1} - p_0}{P_{T0} - p_0} \quad (4)$$

where  $P_{T1}$  is the average total pressure at the inlet throat plane shown in Figure 2.5.  $p_0$  and  $P_{T0}$  is the static- and total pressure in the free stream condition of the flow, respectively.

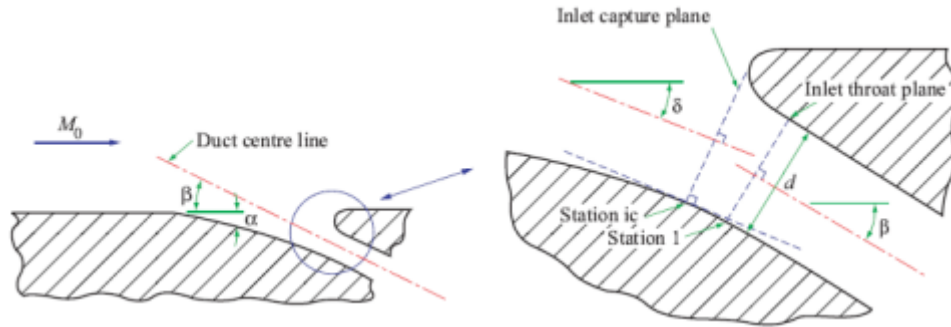


Figure 2.5  
Flush Inlet Denotations. Figure from Reference [5]

## 2.5 Ram Recovery Ratio

Ram recovery ratio is another way the efficiency of an inlet has been judged in previous reports. It is given by

$$\frac{P_{T1}}{P_{T0}} \quad (5)$$

where  $P_{T1}$  is the average total pressure at the inlet throat plane shown in Figure 2.5. and  $P_{T0}$  is the total pressure in the free stream condition of the flow.

## 2.6 Mass Flow Ratio

The inlet mass flow ratio is defined as the ratio of the mass flow through the inlet throat area  $A_1$  to the mass flow of the free stream external to the boundary layer through the same area  $A_1$  at a point sufficiently far upstream as to be unaffected by the presence of the inlet. The inlet mass flow ratio is given by

$$\frac{\dot{m}_1}{\dot{m}_0} = \frac{\rho_1 \cdot V_1 \cdot A_1}{\rho_0 \cdot V_0 \cdot A_1} = \frac{\rho_1 \cdot V_1}{\rho_0 \cdot V_0} \quad (6)$$

where  $\rho$  is the density,  $V$  is the flow velocity and  $A_1$  is the inlet throat area. Subscript 1 indicates values measured at the inlet throat plane (see Figure 1.4 and Figure 2.5) and subscript 0 denotes free stream values.

The value of the mass flow ratio is closely related to the drag of an inlet. The drag increases with increasing mass flow ratio [6].

## 2.7 Navier-Stokes Equations

The Navier-Stokes Equations are in modern aerodynamics the name of five equations which are solved simultaneously to attain information such as velocity, density and pressure at different points in a flow field. The only restriction of these equations (or rather, the momentum equations) is that they are valid for a Newtonian fluid only [7].

*The resistance arising from the want of lubricity in the parts of a fluid is, other things being equal, proportional to the velocity with which the parts of the fluid are separated from one another.*

**Isaac Newton, 1687**

**From Section IX of Book II of his Principia**

The above quote from Isaac Newton is how he defined this type of fluid. The "want of lubricity" should be interpreted, in modern terms, as shear stress. Almost all fluids adhere to this but there are exceptions such as blood flow. Presented below are the momentum, continuity and energy equations which together make up the Navier-Stokes Equations.

### Momentum equations

x-component:

$$\rho \frac{Du}{Dt} = -\frac{\partial p}{\partial x} + \frac{\partial \tau_{xx}}{\partial x} + \frac{\partial \tau_{yx}}{\partial y} + \frac{\partial \tau_{zx}}{\partial z} + \rho f_x \quad (7)$$

y-component:

$$\rho \frac{Dv}{Dt} = -\frac{\partial p}{\partial y} + \frac{\partial \tau_{xy}}{\partial x} + \frac{\partial \tau_{yy}}{\partial y} + \frac{\partial \tau_{zy}}{\partial z} + \rho f_y \quad (8)$$

z-component:

$$\rho \frac{Dw}{Dt} = -\frac{\partial p}{\partial z} + \frac{\partial \tau_{xz}}{\partial x} + \frac{\partial \tau_{yz}}{\partial y} + \frac{\partial \tau_{zz}}{\partial z} + \rho f_z \quad (9)$$

### Continuity equation

The equation of continuity as expressed below states that the rate of change of the mass of a fluid particle moving with the flow is zero.

$$\frac{D\rho}{Dt} + \rho \nabla \cdot V = 0 \quad (10)$$

Where  $\frac{D\rho}{Dt}$  is the time rate of change of density of the fluid element as it moves through space and  $\nabla \cdot V$  should be interpreted as the time rate of change of the volume of a moving fluid element per unit volume.

**Energy equation**

$$\begin{aligned} \rho \frac{D}{Dt} \left( e + \frac{V^2}{2} \right) = & p\dot{q} + \frac{\partial}{\partial x} \left( k \frac{\partial T}{\partial x} \right) + \frac{\partial}{\partial y} \left( k \frac{\partial T}{\partial y} \right) + \frac{\partial}{\partial z} \left( k \frac{\partial T}{\partial z} \right) - \frac{\partial(up)}{\partial x} - \frac{\partial(vp)}{\partial y} - \\ & - \frac{\partial(wp)}{\partial z} + \frac{\partial(u\tau_{xx})}{\partial x} + \frac{\partial(u\tau_{yx})}{\partial y} + \frac{\partial(u\tau_{zx})}{\partial z} + \frac{\partial(v\tau_{xy})}{\partial x} + \frac{\partial(v\tau_{yy})}{\partial y} + \frac{\partial(v\tau_{zy})}{\partial z} + \\ & + \frac{\partial(w\tau_{xz})}{\partial x} + \frac{\partial(w\tau_{yz})}{\partial y} + \frac{\partial(w\tau_{zz})}{\partial z} + \rho f \cdot V \end{aligned} \quad (11)$$

Where  $\rho$  is the local density,  $p$  is the local pressure,  $e$  is the internal energy due to random molecular motion and  $u$ ,  $v$ ,  $w$  are the velocities in the  $x$ ,  $y$ ,  $z$ -directions respectively. These equations were here presented in non-conservation form. For a detailed derivation of these equations and an explanation of the difference between conservation and non-conservation form the reader is referred to Reference [7].

When examining the Navier Stokes equations, one thing we can note is that we have five equations and six unknown flow field variables, namely:  $\rho$ ,  $p$ ,  $u$ ,  $v$ ,  $w$  and  $e$ . To solve a system which consists of multiple equations the number of equations should be equal to the number of variables. To resolve this we add a sixth equation to the system, the equation of state for a perfect gas

$$p = \rho \cdot R \cdot T \quad (12)$$

where  $R$  is the specific gas constant. This, however, gives us a seventh unknown variable, the temperature  $T$ . A thermodynamic relation between state variables is necessary to close the system. For a calorically perfect gas (constant specific heats) we can use the equation

$$e = c_v \cdot T \quad (13)$$

where  $c_v$  is the specific heat at a constant volume. This equation is sometimes referred to as the caloric equation of state.

**2.8 Reynolds-Averaged Navier-Stokes Equations**

The Navier-Stokes equations contain the physical relations needed to describe a turbulent flow for a Newtonian fluid. However, solving these equations for a turbulent flow would require an enormous amount of computational power and time. To manage this problem averaging concepts introduced by Osborn Reynolds in 1895 are used. Reynolds averaging can be expressed in a number of different forms. The three most commonly used forms [8] are:

**Time average**

$$F_T(\mathbf{x}) = \lim_{x \rightarrow \infty} \frac{1}{T} \int_t^{t+T} f(\mathbf{x}, t) dt \quad (14)$$

**The spatial average**

$$F_V(t) = \lim_{V \rightarrow \infty} \frac{1}{V} \int \int \int_V f(\mathbf{x}, t) dV \quad (15)$$

**Ensemble average**

$$F_E(\mathbf{x}, t) = \lim_{N \rightarrow \infty} \frac{1}{N} \sum_{n=1}^N f_n(\mathbf{x}, t) dV \quad (16)$$



The time average form is used to calculate the properties of stationary flows, that is, flows that do not vary with time. An example of a flow of this type is given in Reference [8] as flow inside a pipe driven by a constant-speed blower. This form is the most commonly used as most flows in engineering are of this nature. The spatial average can be used to describe turbulence which is on average uniform in all directions while the ensemble average is appropriate for flows that decay with time.

An unfortunate consequence of applying Reynolds-Averaging of the Navier-Stokes equations is the introduction of six new unknown variables known as the Reynolds-stress components. The new variables have to be found with the help of turbulence models. Different turbulence models have been introduced since the time of Reynolds solving approach.

The RANS solver TAU used in this thesis was established and is still being developed by the German Aerospace Center (DLR). The following turbulence one- and two equation eddy-viscosity models are implemented in TAU:

- One-equation eddy-viscosity models
  - SAO-model (Spalart-Allmaras, original version)
  - SAE-model (Spalart-Allmaras, Edwards modification)
  - SAM-model (Spalart-Allmaras, modified version)
  - SALSAM-model (Strain Adaptive Linear SA-model)
- Two-equation eddy-viscosity models
  - Wilcox  $k-\omega$  model
  - Menter Baseline model
  - Menter SST model
  - LEA  $k-\omega$  model
  - NLR TNT Model
  - Wilcox  $k-\omega$  model + SST
  - Menter 2layer  $k-\epsilon$  model

Additional models does exist for modeling the effects of turbulent flows in TAU. For a complete list and an in-depth explanation of the different turbulence models, the reader is referred to Reference [9] and Reference [10]. The turbulence model used for the CFD calculations in this thesis is the *Spalart-Allmaras, Edwards modification* model.

## 2.9 Spatial Discretisation

The spatial discretisation of the Navier-stokes equations, i.e., the numerical approximation of the viscous and convective fluxes as well as the source term, can be done by three main approaches: *the finite difference method*, *the finite element method* and *the finite volume method*. The RANS solver TAU used in this thesis is based on the finite volume method [11]. To apply any of these methods a computational grid is needed. Three types of grids are used in CFD: *structured grids*, *unstructured grids* and *hybrid grids*.

### 2.9.1 Computational Grids

#### Structured grids

Structured grids consist of quadrilateral elements in 2-dimensional grids and hexahedral elements in 3-dimensional grids. If we use a 2-dimensional grid as an example, an arbitrary point can be assigned a Cartesian coordinate  $(i, j)$ . A point to the right of this point would have the coordinates  $(i+1, j)$ , a point to the left  $(i-1, j)$  and similarly for the points above and below for the coordinate  $j$  as illustrated in Figure 2.6.

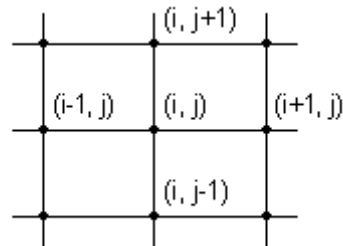


Figure 2.6  
Rectangular grid segment

The ease in which the grid can be expressed in Cartesian coordinates helps when the flow properties are calculated. The nearby points can quickly be identified and the flow parameters in these points help the convergence of the calculated flow parameters in the targeted point.

#### Unstructured grids

These types of grids are made up of triangular elements in 2-dimensional grids and tetrahedral elements, pyramids or prismatic elements in 3-dimensional grids. They can quickly be generated automatically to cover a large surface or volume with few input parameters but has the disadvantage of not being numbered in a manner similar to that of the structured mesh elements.

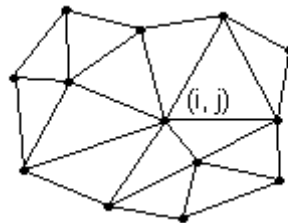


Figure 2.7  
Unstructured grid segment

This results in higher computational effort to find nearby grid points. Another disadvantage of unstructured grids is the uneven distribution of elements in physical interesting regions, e.g., the boundary layer. This disadvantage can be overcome by the use of a hybrid grid.

#### Hybrid grids

A hybrid grid is a combination of unstructured and structured grids into one single grid. It has advantages of both grid types. Structured elements are used in close proximity to surfaces and other physical interesting regions while unstructured elements are used to quickly fill the remainder of the calculation space.

### 2.9.2 Discretisation Methods

#### Finite Difference Method

This method is directly applied to the differential form of the governing Navier-Stokes equations. It employs a Taylor series expansion of the derivatives of the flow variables [9]. It has the advantage of simplicity but requires a structured grid to work with. The use of the finite difference method is very limited in modern aerodynamics.

#### Finite Element Method

The finite element method when applied to the Navier-Stokes equations starts with a subdivision of the physical space into triangular elements when working with a 2-dimensional grid, and into tetrahedral elements when working with 3-dimensions. The finite element method requires the governing equations to be expressed in integral form, and thus the equations have to be transformed from differential form. This method is advantageous for use around complex geometries because of its unstructured approach and the mentioned use of the integral form of the governing equations [9]. The finite element method is commonly used in structural analysis of materials.

#### Finite Volume Method

The finite volume method requires the physical space to be divided into a number of polyhedral control volumes in order to discretise the governing equations. The finite volume method requires also, as in the case with the finite element method, the integral form of the Navier-Stokes equations. The advantage of this method is that the discretisation is carried out directly in the physical space, requiring no transformation between the physical space and a calculation grid. The method can be applied to both structured and unstructured grids.

### 2.9.3 Central and Upwind Schemes

The methods discussed above require a numerical scheme to perform the spatial discretisation. While numerous different schemes exist, a brief explanation will only here be given for the *central scheme* and the *upwind scheme* as they are employed by the flow solver TAU [11].

#### Central Schemes

Belonging to this group are schemes based on central averaging or central difference formula. The values of the variables on either side of an element are averaged to evaluate the fluctuations in close proximity to the element. However, central schemes require an artificial dissipation to keep stable. A clear advantage is that in most cases a central scheme is more effective than the upwind scheme in view of CPU usage.

#### Upwind Schemes

Upwind schemes are able to capture discontinuities more accurately than central schemes and solve boundary layer parameters accurately with fewer calculation points. The downside of upwind schemes is that limiters have to be used to prevent oscillations of the solution variables close to strong discontinuities.

The central and upwind scheme can be combined when making a complete calculation of a flow field to obtain a converged and accurate solution. When using the flow solver TAU it has proven

advantageous to use upwind scheme for the first thousand or more calculations, and then switch to a central scheme for the remainder of the calculations.

## 2.10 Time Discretisation

For greater flexibility different approaches are used for spatial and time discretisation. Two different types of schemes are employed by TAU for time discretisation of the governing equations, namely *explicit*- and *implicit schemes* [10].

### Explicit Schemes

In the explicit approach to the governing equations there is only one unknown variable. Let this variable be denoted by  $A_i^n$  where  $i$  denote the node we are investigating, and  $n$  indicates the moment in time. Known values  $A_{i-1}^{n-1}$ ,  $A_i^{n-1}$  and  $A_{i+1}^{n-1}$  from the previous time-step are used to calculate the flow parameters in the new point. One equation and one unknown results in an easy definition and set-up of the problem. Very advantageous from a programming point of view but it does have its drawbacks. In some cases the time-step has to be very small to maintain stability of the solution which can result in long calculation times. The use of parallel processors has made these type schemes very interesting as each processor can work on a separate part of the grid with minimum intercommunication necessary [7].

### Implicit Schemes

Implicit schemes are much more complicated to solve than the explicit schemes. Instead of an equation with the unknown variable at one point  $A_i^n$  requiring information from points in the previous time-step, we have an equation with three unknowns, namely  $A_{i-1}^n$ ,  $A_i^n$  and  $A_{i+1}^n$ . The solution must be attained by solving an entire system of equations simultaneously. This approach has the advantage of allowing for greater time-steps than the explicit schemes resulting in less computational time. It should however be kept in mind that due to the system of equations being more complex, each time-step takes longer to calculate. As this method requires large amounts of information to be exchanged between nodes it is less suited for parallel processors [7].

### 3 Methodology

#### 3.1 Preliminary Studies

##### 3.1.1 Inlets

There are two basic types of inlets: *scoop inlets* protruding from a surface into the free stream and *flush inlets* submerged into a body.

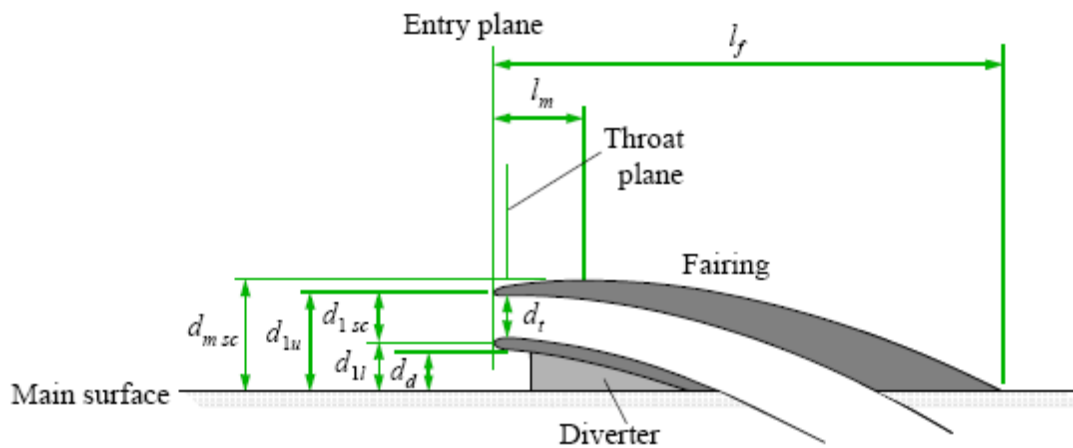


Figure 3.1  
Scoop inlet. Figure from Reference [6]

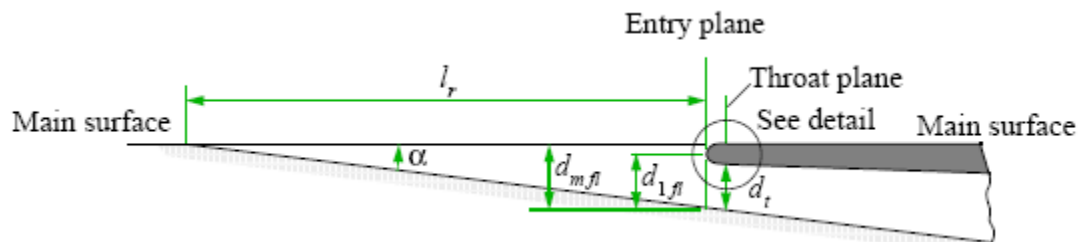


Figure 3.2  
Flush inlet. Figure from Reference [6]

Advantages and disadvantages exist with both design choices. While the scoop inlet has the advantage of avoiding the low energy boundary layer which reduces the efficiency of an air inlet, it has typically the disadvantage of a greater increase of aerodynamic drag compared to a submerged inlet.

The aircraft industry is very interested in solutions that reduce the aerodynamic drag, and in extent the fuel consumption of an airplane. The air inlet investigated in this report is of flush type.

##### 3.1.2 Flush Inlets

An air inlet should not, if optimal, increase the drag of the body into which it is placed or reduce the energy available in the air which enters the inlet. These criteria cannot be fully met by any

air inlet, but design parameters can be changed to come close to an optimum for a specific flight condition. For low drag it is advantageous to use a flushed inlet which is submerged into the surface of the body into which it is placed. The flush type is also advantageous to avoid foreign object damage on the inlet.

It is possible to divide flushed inlets into three basic categories depending on the geometry of the walls of the inlet: *parallel walls*, *convergent walls* and *divergent walls*.

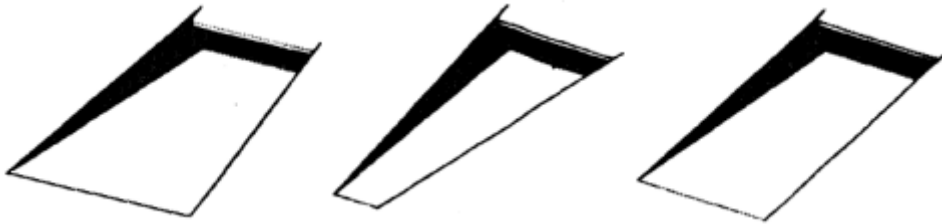


Figure 3.3

Flush inlets with convergent walls, divergent walls and parallel walls respectively.

Figures from Reference [12]

### Parallel Walls

Reference [6] makes a comparison between three different ramp planforms to assert the effect of the change in planform has on the performance of the inlet.

A curved-divergent submerged intake has a higher ram pressure efficiency for all mass flows in the interval  $0 < \frac{\dot{m}}{\dot{m}_0} \leq 1.0$ . While the peak of performance for a curved-divergent intake takes place at a mass flow ratio of around 0.4, the peak of performance for an inlet with parallel walls is at the much higher mass flow ratio of 0.7 and above. While this is the case, the report also shows that for a certain mass flow ratio, the overall drag caused by the different types of inlets is lower for the inlet with parallel walls.

The wetted area between the inlet *entry plane* and the inlet *throat plane* (denotations seen in Figure 3.2) for an inlet with parallel walls is a minimum for a width/depth ratio of 1. This means that the amount of low energy boundary layer air should also be at a minimum. It is discussed in Reference [5] that at high mass flow ratios, this parameter becomes more significant in determining the ram pressure efficiency of the inlet.

### Divergent Walls

The divergent walls of this type of inlet cause strong vortices to develop along the ramp edges as shown in Figure 3.4.

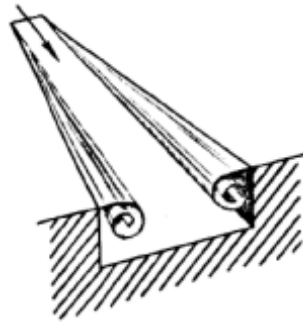


Figure 3.4

Vortices formed along the edges of a flush inlet with divergent walls. Figure from Reference [12]

This is because along the ramp the flow follows the divergent walls while the flow along the body into which it is submerged is parallel to the free stream. As a consequence there is a sudden change of the direction of the flow at the ramp edges giving rise to rotational flow [13]. The boundary layer is thinned out by these vortices in the inlet influencing region [6] and so the pressure loss due to the boundary layer is reduced, however, due to the vortices themselves there is a total pressure loss. The vortices created along the ramp edges additionally cause air flow of higher velocity further away from the surface to be caught and enter the duct, increasing the mass flow ratio. The overall beneficial effect of the vortices in terms of ram pressure efficiency is judged to be greater than the adverse effects.

Reference [14] observed that divergent walls divert much of the boundary layer around the intake. This effect additionally supports the increase of efficiency. The reason for this is discussed by the authors of the report as having two possible causes. The first is based on the ramp pressure distribution and the pressure just prior to the ramp cause the boundary layer to divert away from the inlet. This effect was analysed on pressure measurements that indicated velocity ratios below 1.0 in that local region. The second reason was analysed to be caused by the sharp edges of the ramp walls that prevent the boundary layer to flow over the edges into the inlet. This was deduced from an experiment where the edges were rounded, causing a great decrease of the beneficial effects of the diverging walls. The effect of the sharp edges of the ramp walls preventing the boundary layer to flow over the edges into the inlet will be investigated as a part of this thesis.

### Convergent Walls

This type of flushed inlet present a number of problems if used for air supply on an aircraft. Because of the convergence, the boundary-layer growth rate along the floor is increased reducing the efficiency of the inlet [12]. There is also the possibility of vortices developing along the ramp edges outside of the inlet.

#### 3.1.3 NACA Curved-Divergent Inlet

The initiative for the divergent curvature of the NACA curved-divergent inlet as shown in Figure 3.5 was first taken in 1945 by the National Advisory Committee for Aeronautics.

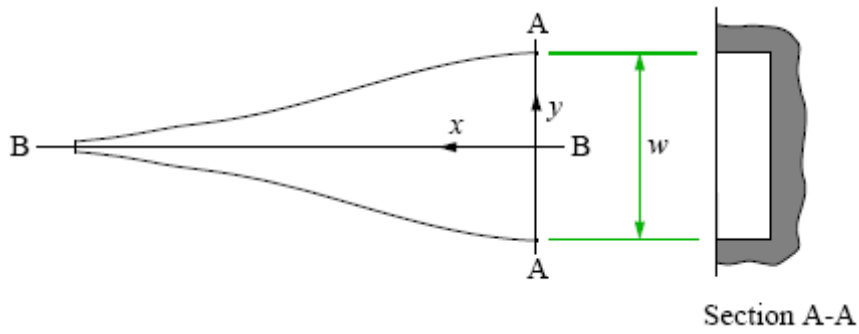


Figure 3.5  
NACA curved-divergent planform. Figure from Reference [6]

$x/l_r$	0.0	0.1	0.2	0.3	0.4	0.5	0.6	0.7	0.8	0.9	1.0
$2z/w$	0.996	0.916	0.996	0.766	0.614	0.466	0.388	0.312	0.236	0.158	0.085

Table 3.1  
Ramp coordinates for NACA curved-divergent planform. Table from Reference [6]

The first report investigating this type of inlet (Reference [15]) presented results of a number of wind tunnel tests in which the curvature (one of several parameters investigated) of the ramp walls was varied. The resulting design, today generally known as a NACA duct or NACA-type inlet, was that one that showed highest pressure recovery and for which further studies was recommended. The following reports during the 1940s and 1950s focused mainly on an experimental approach to determine how the different parameters such as boundary-layer thickness, ramp plan form, ramp angle, lip geometry and width/depth ratio affects the pressure recovery and drag of the inlet.

Vortices such as those described for the divergent ramp walls form by the presence of this inlet. These vortices affect the boundary layer on the ramp of the inlet and sweeps it towards the edges [16]. These vortices carries some of the boundary layer past the ends of the entry and out into the external flow [16].

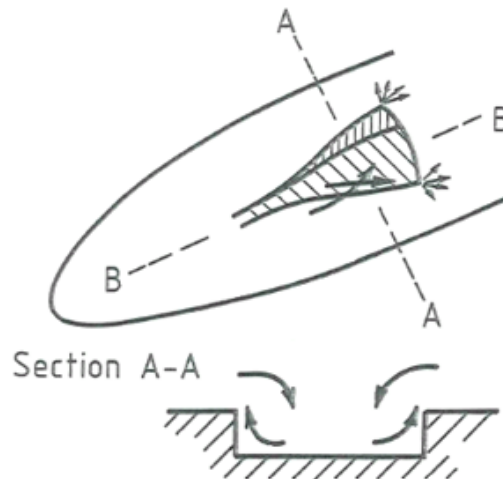


Figure 3.6  
NACA curved-divergent inlet. Figure from Reference [16]



### 3.1.4 Design Parameters

This section contains a discussion on how design parameters influence the properties of a NACA curved-divergent inlet according to previous studies. The NACA report used as reference in this section (Reference [14]) carried out a number of experiments to investigate design variables of a NACA inlet in a wind tunnel setup. The wind tunnel test arrangement of the submerged inlet in the NACA report can be seen in Figure 3.7.

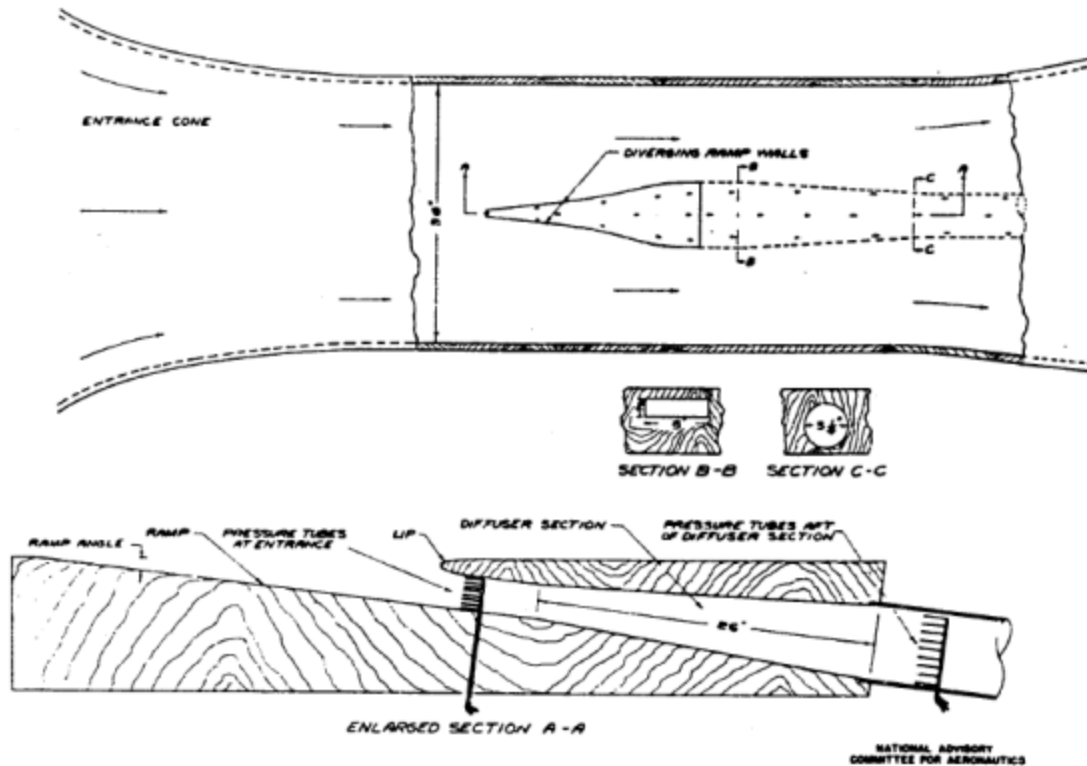


Figure 3.7

Arrangement of the submerged NACA inlet in Reference [14]. Figure from Reference [14]

The ESDU papers used as reference (Reference [5] and Reference [6]) are based on theoretical calculations along with test data from NACA experiments.

The parameters which can be subject to change and which determine the properties of a submerged inlet are:

- Ramp angle
- Width/Depth ratio
- Ramp plan form (Curved-divergent in the case of a NACA inlet)
- Ramp length
- Lip design
- Position of the inlet
- Boundary layer thickness (depending on position)
- Usage of deflectors

### Ramp Angle

Investigations in Reference [6] show that for ramp angles greater than 5 degrees, the ram pressure efficiency decreases with an increase of the ramp angle. Experiments carried out in Reference [14] established that the decrease in pressure recovery due to an increased ramp angle has a relation to the width/depth ratio, resulting in a greater reduction at higher width/depth ratios. It is further discussed in this report that the pressure loss as a result from an increase in ramp angle has a strong correlation to the resulting geometrical change of the ramp plan form. An increased ramp angle increases the angle between the diverging walls and in effect the tendency for flow separation. The obliquity between the free stream flow and the ramp walls is increased making it difficult for the free stream to follow the outer contour of the inlet and flows instead directly into the duct. This results in a reduction of the ram pressure efficiency as a larger proportion of the airflow entering the duct will consist of the low energy boundary layer.

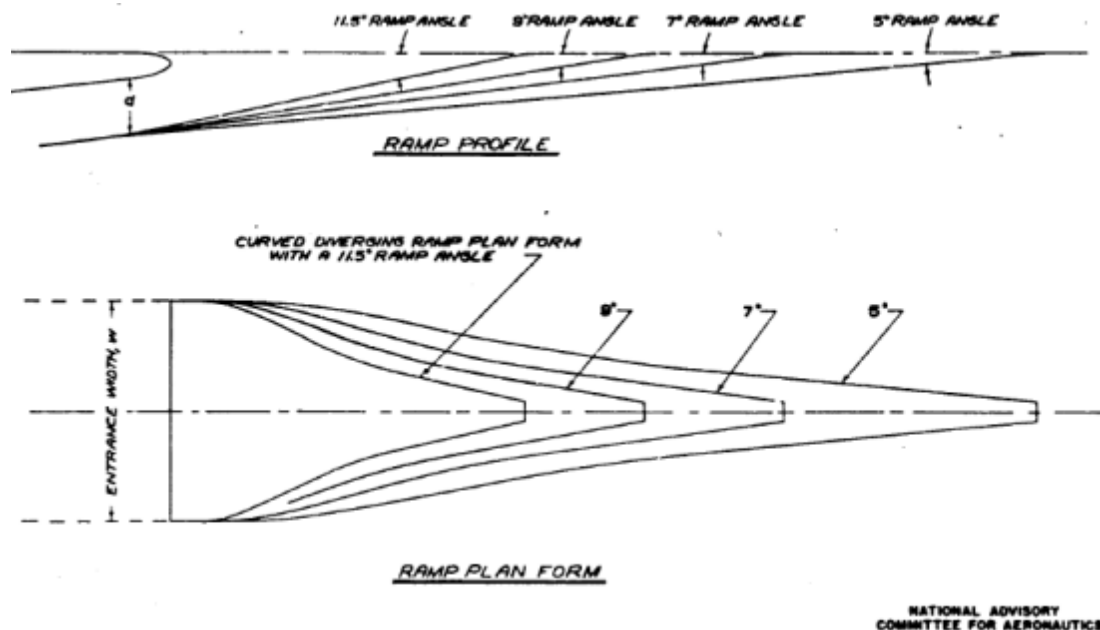


Figure 3.8

Resulting change of the ramp from a change of ramp angle. Figure from Reference [14]

Reference [6] suggests a width to depth ratio of around 4 and a ramp angle of 7 degrees for best pressure recovery.

### Width/Depth Ratio

Width to depth ratio is an important parameter as it will decide how many percent the boundary layer thickness will make up of the total height of the inlet. Experiments made in Reference [6] show that a width to depth ratio between 3.5 and 5.5 is desirable for a high pressure recovery with an optimum between 4 and 4.5. The width/depth ratio for the investigations within this thesis are between 2.3 and 5.4.

### Ramp Length

This parameters is directly related to the ramp angle and the width/depth ratio. It is in practical applications usually the parameter that place restrictions on the geometry of the inlet.

### Boundary Layer Thickness

The boundary layer thickness has been proven to play an important role for the ram pressure efficiency of an inlet. An increase in boundary layer thickness causes a decrease of the ram pressure efficiency [5]. This could be expected as the boundary layer contains flow at a lower velocity than that of the free stream. A general recommendation to avoid a thick boundary layer entering the inlet is to place the inlet closer to the leading edge of the surface into which it is submerged.

The boundary layer on the ramp walls of the air inlet has no initial thickness and grows over a very short distance before entering the inlet and has thus only a small impact on the ram pressure efficiency. The reduction of ram pressure efficiency due to the boundary layer from the walls of the inlet is only about 5-10 % of that due to the boundary layer on the ramp [12].

### Position of the Inlet

The main need for air supply on larger modern commercial aircrafts is usually supplied by ram air inlets on the belly fairing. The heat exchanger and related ducting are found inside the belly fairing, whwich is the fairing between aircraft wing and fuselage.

Recent investigations of different types of submerged inlets indicates that the efficiency of an inlet geometry depends greatly on the surface into which it is placed. For a NACA curved-divergent inlet it seems that the inlet is the most efficient on a surface that is parallel to the free stream. A submerged inlet with parallel walls seem to be more efficient at "ramps", e.g. regions such as the forward facing part of a belly fairing, as it is seen in Figure 3.9.

This choice of inlet type in a certain area depends greatly on how the area in which it is placed is affected by different flight phases and sidewinds. If it is greatly affected, an inlet with curved divergent walls is to be preferred.

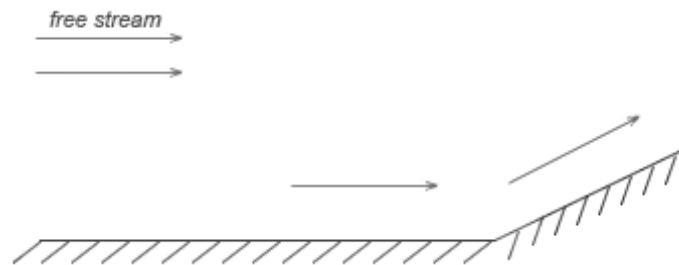


Figure 3.9

Surface parallel to the free stream and a ramp section.

A design option with a wider initial width of a divergent inlet can be made to compromise between these features.

### Deflectors

Deflectors are small ridges placed along the ramp walls on the surface into which the submerged inlet is placed.

The use of deflectors increase the ram pressure efficiency of the inlet but increase the drag. It is discussed in Reference [14] that the increase of ram pressure efficiency is because the flow along the surface outside of the inlet follows the contour of the inlet. Preventing flow of air over the edges of the ramp walls.

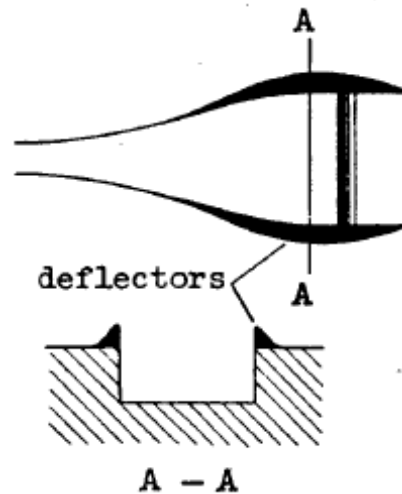


Figure 3.10  
Deflectors. Figure from Reference [12]

The use of deflectors, and how different parameters for these affects the ram pressure efficiency are not investigated as a part of this report.

### 3.1.5 Inlet Drag

It is possible to divide the drag of an inlet into two components: *momentum drag* and *spillage drag*.

#### Momentum Drag

The drag of a flush inlet is primarily due to momentum loss in the onset flow direction [5]. The difference is measured between a point upstream where the flow is unaffected by the presence of the inlet and the inlet throat plane (denotations seen in Figure 3.2). The geometry of the inlet and the proportion of the boundary layer thickness to the height of the inlet are the factors having the greatest effect on the value of the momentum drag.

#### Spillage Drag

Spillage drag has its origin in spillage of flow around the lip of the inlet. At the inlet lip there will be a stagnation line for the streamtube entering the duct and as the mass flow ratio decreases below 1, the stagnation line moves internally into the duct [5]. As a result the flow outside of the streamtube has to negotiate the lip. In general the flow outside of the streamtube will be affected by the lip and inlet geometry as a whole.

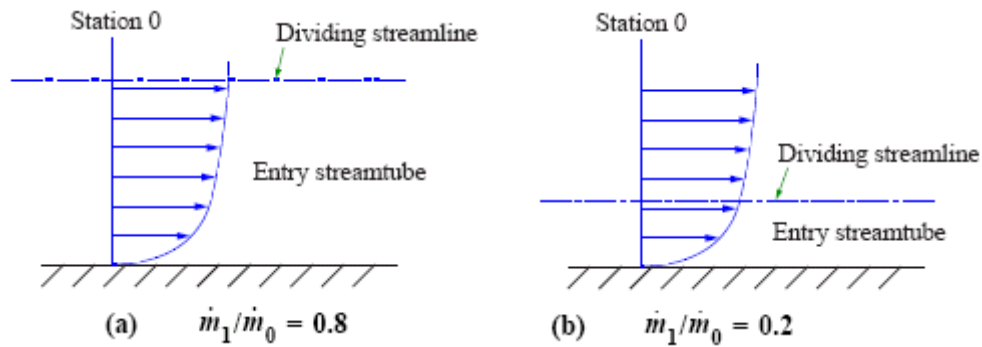


Figure 3.11

The effect of mass flow ratio on the entry streamtube. Figure from Reference [5]

It is recommended that a flush inlet has a round lip, because flow separation will occur aft of the lip should the lip be too sharp [5]. However, with a rounded lip the flow still has to negotiate an adverse pressure gradient and so the boundary layer thickens and increases drag as a result. Should the gradient be large enough, a separation of the flow will occur despite the use of the rounded lip [5].

### 3.1.6 Plenums

Two different types of plenums have previously been investigated within the ECOCENTS project. The plenum is the "bend" section shown in the images below. The two different designs are shown in Figure 3.9 and Figure 3.10. They are referred to as the *classic plenum* and the *base plenum*. The plenum investigated in this thesis is the *plenum base* as it was analysed in a previous CFD study to perform slightly better than the classic plenum.

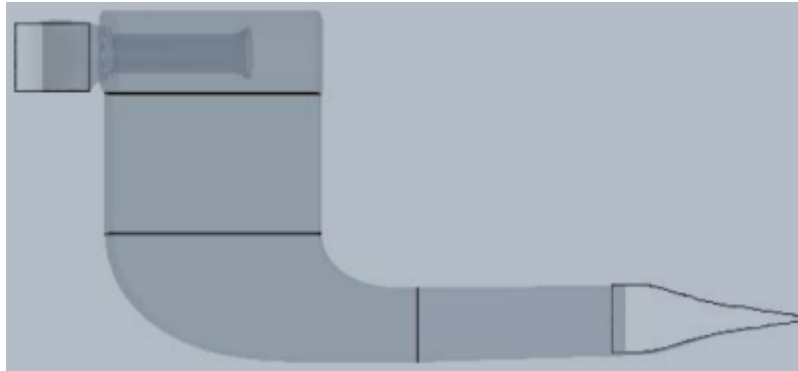


Figure 3.12  
Plenum classic. Figure from Reference [17]

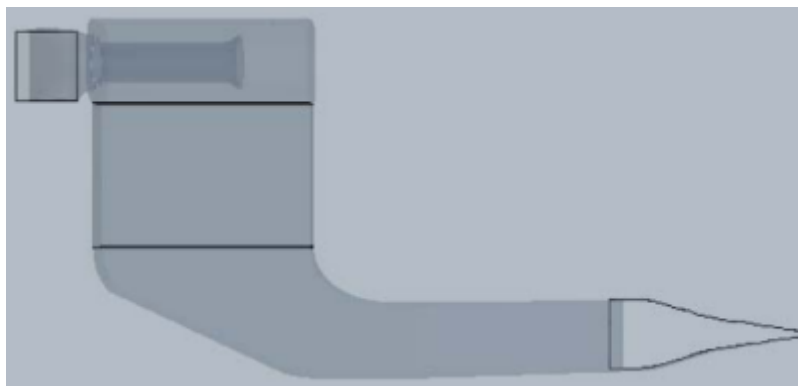


Figure 3.13  
Plenum base. Figure from Reference [17]

### 3.2 Geometry Preparation

The wind tunnel geometry as well as the NACA duct geometry was provided to the author of this thesis by Airbus. An approximately 5.8 meter extension of the wind tunnel was made to allow the flow to stabilize aft of the test section.

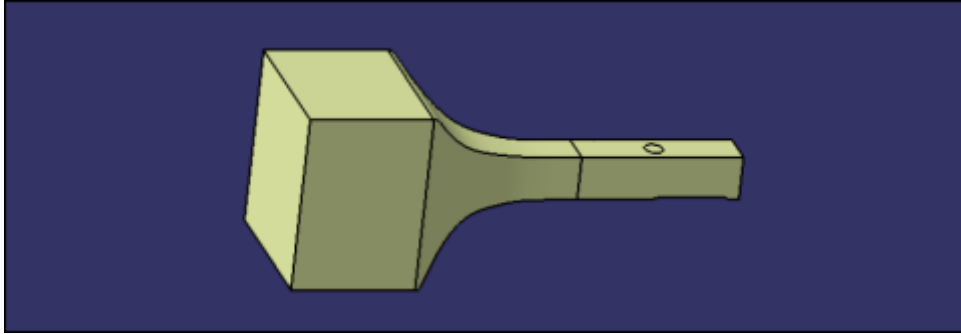


Figure 3.14  
Original wind tunnel geometry

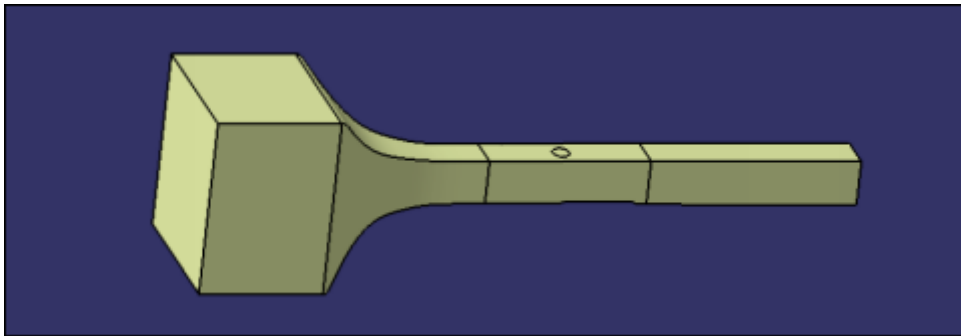


Figure 3.15  
The wind tunnel geometry with an extension aft of the test section

The first step of the geometry preparation process in CEN TAUR was to import the IGES file exported from CATIA. When importing an IGES file an automated query appears asking if a CAD diagnostic should be run. The CAD diagnostic identifies problematic panels and curves which need to be resolved to attain a valid geometry for mesh generation. An automated CAD cleaning tool can resolve some of these inconsistencies but manual labour is often necessary to resolve all issues. Figure A.2.11 and Figure A.2.12 in Appendix A2 shows a part of the wind tunnel geometry before and after automated and manual CAD cleaning. A curve with a number written in purple indicates that there is an issue with this curve that needs to be resolved.

The next step was to extend the wind tunnel test section. The extended test section part was made in CATIA and imported into CEN TAUR in the correct position as the IGES file contains information on the coordinates of the model.

A modular mesh approach was used to minimize the time required to generate the complete grid. Modular mesh generation means that when the correct settings for the grid outside of a modular box has been found, subsequent mesh generations can be limited to the contents of the modular box. This saves computational time at the mesh generation stage and reduces the difference of the final TAU results induced by the grid itself outside of the module. If we were to generate the entire grid anew after changing the geometry, grid nodes would be generated in slightly different positions and thus have a small effect on the result.

To define the boundary of the module in CENTAUR, two different approaches were available. The first was to apply the *Bounding Box* feature in CENTAUR and the second to create a new box in CATIA and import the geometry into CENTAUR. The second approach was chosen and the boundary of the module and the box itself as shown in CATIA can be seen in Figure 3.16 and Figure 3.17.

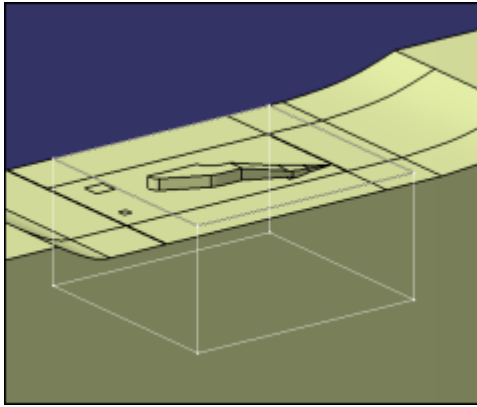


Figure 3.16

The boundary of the module

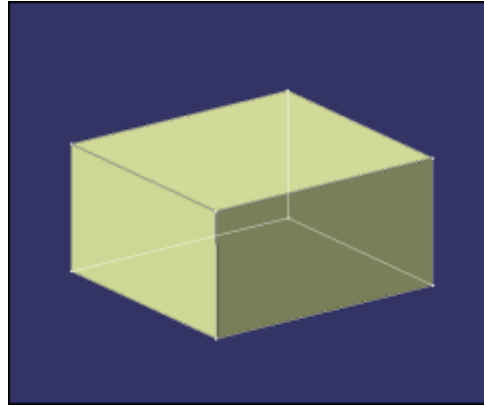


Figure 3.17

The module ready to be imported into CENTAUR

The ramp angle of the inlet was varied in CATIA by changing a parameter in the original geometry file. Models at four different ramp angles were generated:

- 4°
- 7°
- 10°
- 15°

The ramp angle of seven degrees is of main interest in this report. This is the angle recommended by previous studies. The angle which is subject to change is the variable ramp angle shown in Figure 1.3, presented again below. The effect on the inlet and the subsequent diffuser section by a change of this angle can be seen in Figure A.2.13 - A.2.16 in Appendix A2.

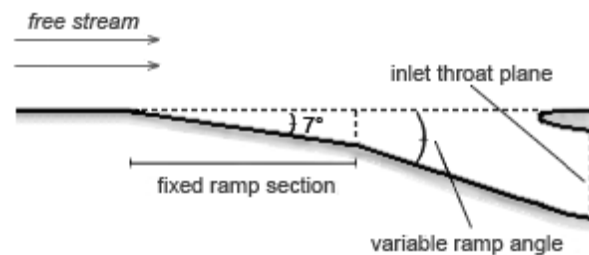


Figure 1.3

Cross section of an inlet.

A three dimensional view of the inlet system can be seen in Figure 3.18.



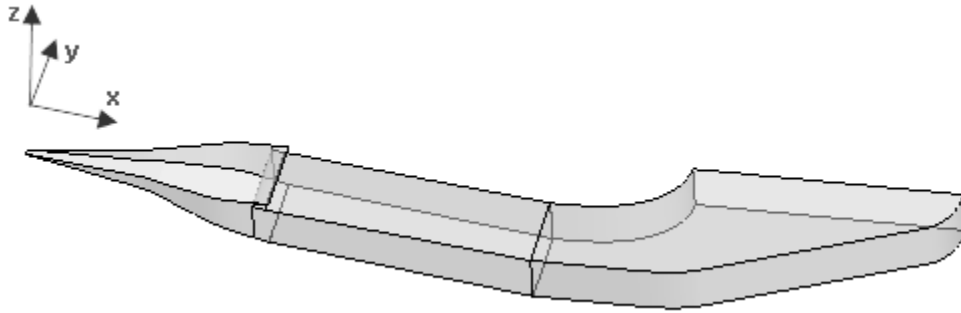


Figure 3.18  
The inlet system with coordinate axis

It was suggested by Reference [18] that an extension be made to the duct after the plenum section. The extension was recommended to be at least three times the length of the channel. This change was made directly in CEN TAUR by applying the *Bounding Box* feature. A boundary box consist of six panels and is defined by two sets of coordinates: minimum and maximum x,y and z-coordinates.

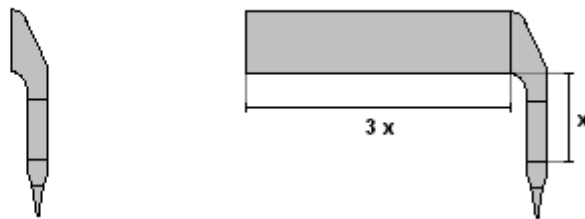


Figure 3.19  
Illustration of the extension made to the duct prior to the outlet

### 3.3 Mesh Generation

The prismatic elements are marched perpendicular from all surfaces with the surface elements as basis, the best approach is therefore to generate and refine the surface mesh before generating the mesh in its entirety. Areas which at once could be identified as requiring refinement were the interior of the inlet and the lip. Surface refinement in proximity to the inlet was also applied with geometrical sources. The lip of the inlet was refined according to the current best practice described in Reference [19] with the surface element size at the outer radius of a cylinder shaped source being 2 times the element size at the center.

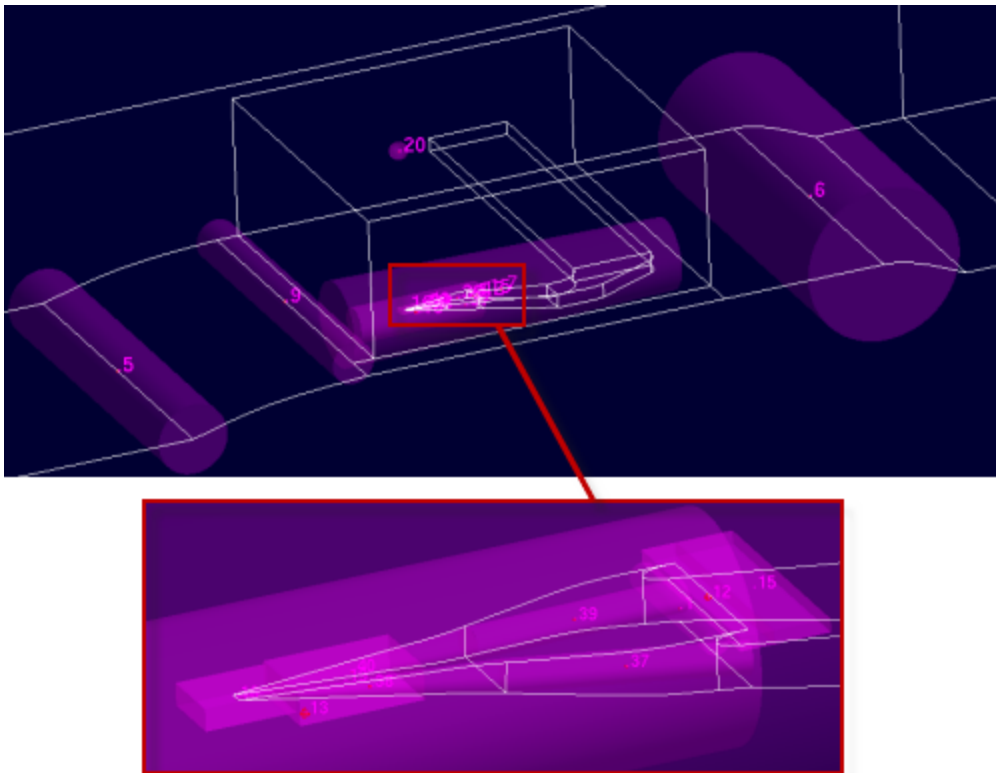


Figure 3.20  
Geometrical sources in the test section of the wind tunnel

With the settings of the surface mesh grid adjusted to appropriate values the first prismatic mesh could be generated. All meshes generated were done so by sending the job to a server which distributed the job to an available CPU. This made it possible to generate multiple meshes at the same time. This was vital as the effect on the mesh by changing a parameter in CENTAUR was sometimes hard to predict, making it necessary to try out multiple different settings.

The global prismatic settings of the wind tunnel were defined with the help of the python script *bl\_prism\_layer\_parameters\_v2.py* made at Airbus for the purpose of calculating prism layer parameters. The input and output from the use of this script can be found in Appendix A7.

Additional surface mesh improvements proved necessary to attain an acceptable prismatic mesh. The goal of the refinement of the prismatic mesh was to capture the boundary layer as much as possible with these structured elements. Achieving this assures a good resolution of the boundary layer and its properties [20]. The internal corners of the inlet were problematic areas as prismatic elements build from both side walls in the corner and cannot be connected together. Limited by the space the number of layers is reduced considerably. To avoid this to the greatest extent, CAD sources with reduced surface cell size were added defined by the lines in the corners of the inlet with a radius of influence.

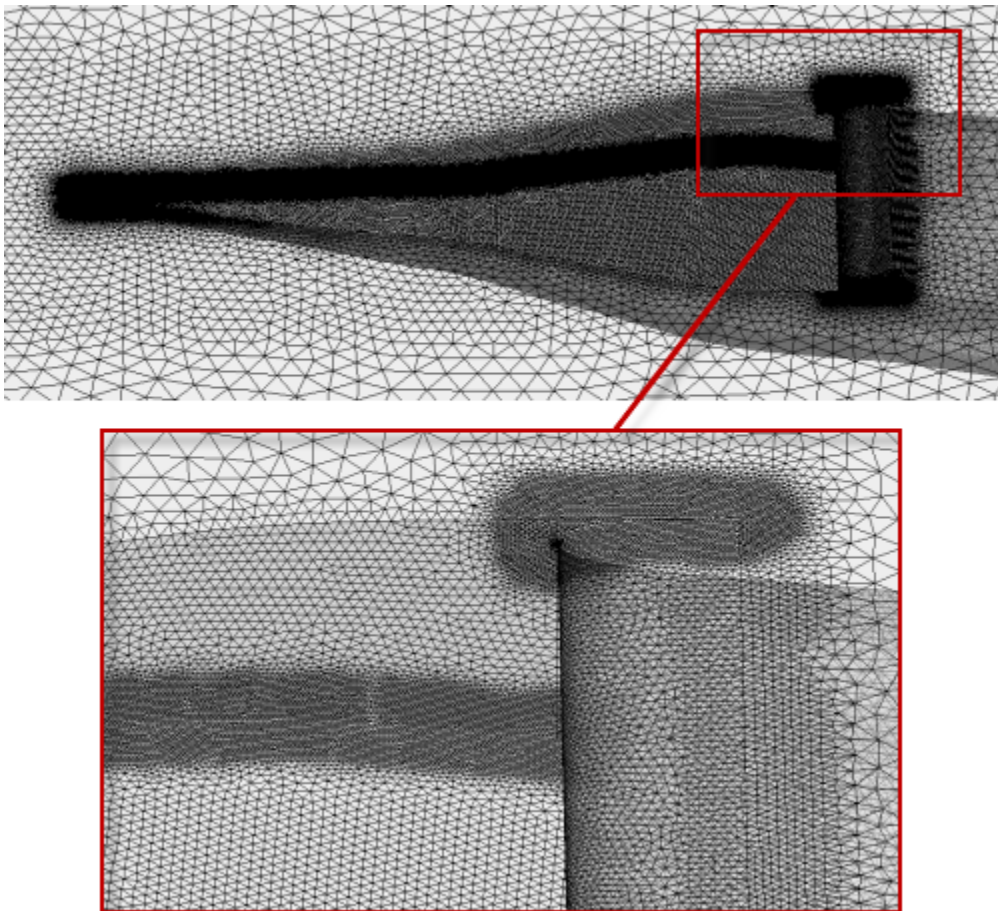


Figure 3.21  
Surface mesh at the inlet

Only one prismatic layer can grow back per element away from the corner. Reducing the cell size in this area will make the number of prismatic layers get pull-backed and grow up in a shorter distance. The result can be seen in the Figure 3.22 below and Figure A.2.17 in Appendix A2.

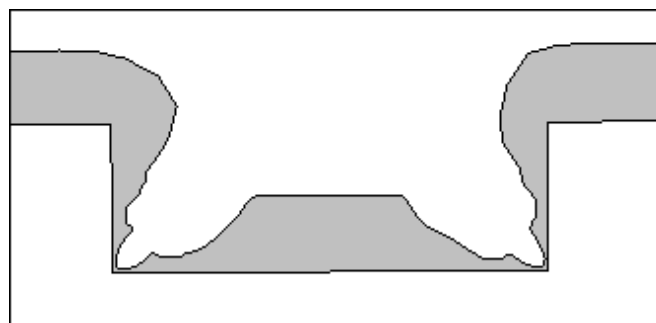


Figure 3.22  
The contour of the prismatic layers inside the inlet

The prismatic and tetrahedral mesh for two different positions in the inlet for the 7 degrees constant ramp angle can be seen in Figure 3.23 and Figure 3.24. Position of x-coordinates can be found in Figure A.2.4 in Appendix A2.

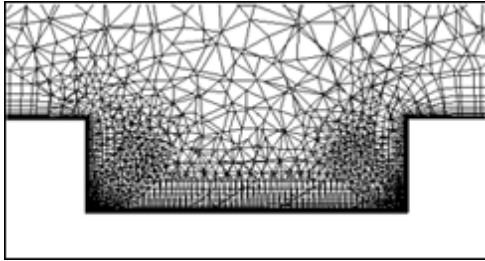


Figure 3.23  
The mesh at  $x = 135$

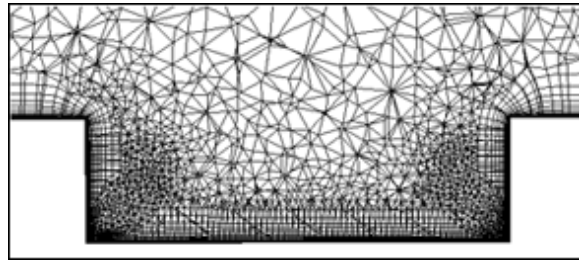


Figure 3.24  
The mesh at  $x = 180$

Another area of great difficulty was the transition from the wind tunnel floor into the initial ramp of the inlet. Due to the very small initial width of the inlet and the distance between the ramp walls, chopping occurs here as well. This problem was dealt with in a similar manner as that with the inner edges of the inlet: a source with very fine surface cell size. Further improvement was attained by using the modular meshing approach. When generating the module by itself a finer prismatic mesh was obtained compared to the mesh obtained when generating the complete tunnel including the contents of the module. In this way the number of layers at the transition into the duct increased from 14 to 21.

It was suggested by Reference [18] that the internal duct after the bend should have hexahedral surface elements and covered in most part by prismatic elements. This was implemented and achieved by increasing the number of prismatic layers to cover the desired volume. It was further suggested that the walls leading to the outlet should have their boundary condition set to inviscid wall. This suggestion was also embraced and implemented.

The modular mesh approach used in this thesis proved to save time when it was time to make changes to the geometry inside the modular box. Generating the whole wind tunnel geometry took approximately 8h while generating the contents of the module took approximately 2h. As a concluding remark it can be noted that the wind tunnel geometry and the contents inside the modular box was made up by approximately 30 000 000 elements by the end of the mesh generation process.

### 3.4 Numerical Computation

The air inlet configurations investigated in this thesis were done so in a wind tunnel set-up. The RANS solver TAU used in this thesis was originally established at DLR for external aeronautical flow simulations. Additional solver modules have been implemented to allow for specific simulation problems to be solved.

The wind tunnel set-up used in TAU for this thesis was previously investigated by the software developers in Reference [21], Reference [22] and also within a previous Airbus study (Reference [23]). The reports and presentations from DLR described two approaches within TAU to simulate wind tunnels:

- Wind Tunnel Boundary Condition [21]
- Engine Boundary Condition [21]

Both numerical approaches require similar inputs for the boundary conditions, only some of the physical variable names are different. The results of both approaches are expected to be equal.

One very promising approach required an extension prior to the original wind tunnel geometry as can be seen in the left part of figure 3.25

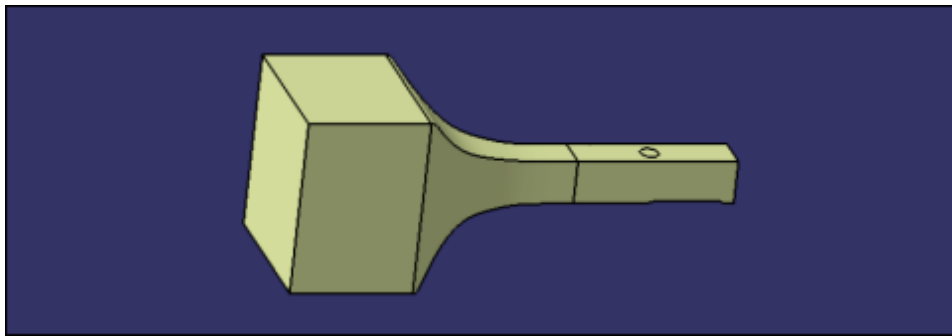


Figure 3.14  
Original wind tunnel geometry

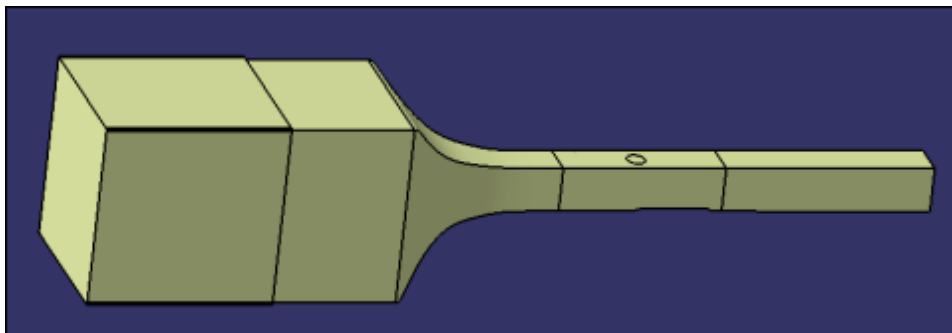


Figure 3.25  
The wind tunnel geometry with extensions

The reason for this wind tunnel inlet extension was to create a small gap surrounding the wind tunnel inlet lip to serve as an additional outlet as seen in Figure 3.26 and Figure 3.27. The dimensions used for this extension can be seen in detail within Appendix A2.

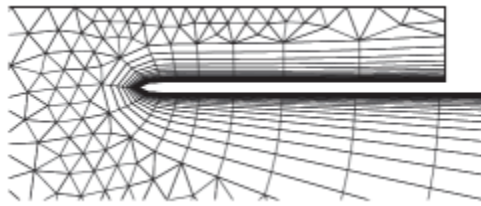


Figure 3.26  
Computational grid at the additional outlet  
Figure from Reference [21]

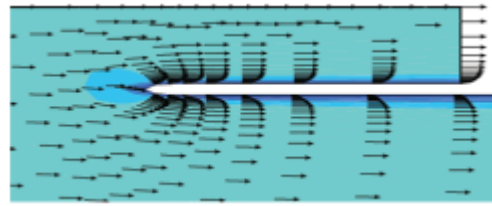


Figure 3.27  
Velocity profiles at the additional outlet  
Figure from Reference [21]

This set-up has the big advantage to define wind tunnel inlet condition for the RANS computations in a single point within the inlet plane, similarly as it would be measured in wind tunnel tests. The wind tunnel inlet extension was considered to be an inviscid wall, hence the mesh contained tetrahedras similarly to how it is seen in Figure 3.26.

Reference [21] describes that this additional outlet would act in conjugation with the simulation inlet plane such that the requested physical condition will be iteratively adjusted for the introduced reference point. Figure 3.28 Shows that adjustment approach.

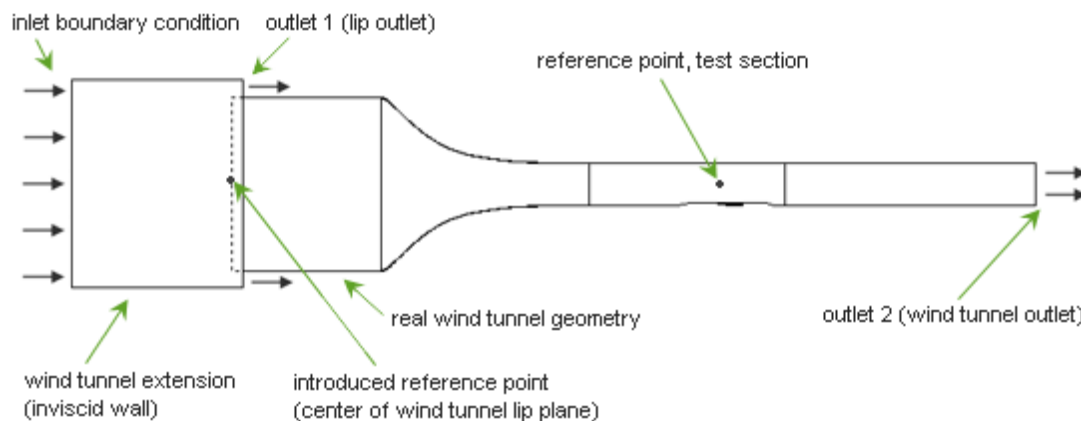


Figure 3.28  
Schematic set-up of the numerical wind tunnel simulation.  
Wind tunnel extension (inviscid wall) not to scale

This promising approach was pursued to great length, and with technical reports by DLR [21] it was believed that it would work for the geometrical set-up in this thesis. However, within the work of this thesis it was impossible to get the numerical computations to run stable over a certain iteration number. The reason for this unstable numerical behaviour is seen in the difficulty for the solver to get adjusted two reference points. This problem was impossible to solve by varying the intervall steps between iterations for when flow parameters were adjusted.

It turned out that in order to achieve the goal of this thesis a more basic approach had to be used. The additional geometry prior to the original wind tunnel inlet had to be removed and the boundary condition "wind tunnel inlet" was applied at the wind tunnel inlet plane.

The final numerical wind tunnel set-up that was used within this thesis is seen in Figure 3.15 below.

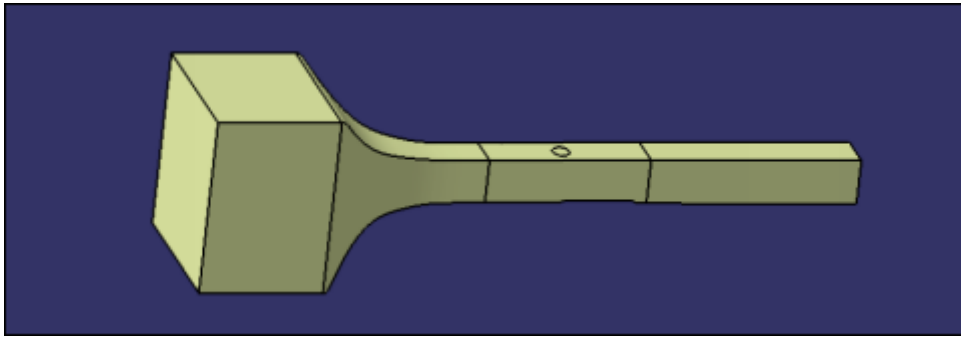


Figure 3.15

The wind tunnel geometry with an extension aft of the test section

Another problem that was observed within the work of this thesis was the definition of the wind tunnel reference condition: According to reports of DLR [21] the reference point for the wind tunnel condition can be defined at any point within the flow field in the test section. A recommendation of Reference [21] was followed making the mesh finer at that reference point and the surrounding region. This can be seen in Figure 3.29.

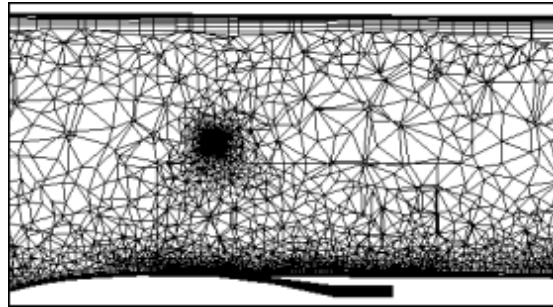


Figure 3.29

Close-up of the mesh at the wind tunnel test section

In Figure 3.29 the reference point for the test section condition is in the middle of the refined region of tetrahedral elements.

Even if all settings were done as Reference [21] recommended, it was observed that the TAU solver routine was not stable to get a solution. Similar observations were reported in Reference [23] where it was decided to use a TAU version from 2006 with special settings for wind tunnel simulations. At the time Reference [23] was published the TAU developer team was contacted to check the TAU solver in view of wind tunnel set-ups. It was promised that from TAU version 2009.2.0 it would work. Within this thesis, TAU versions 2008.1.0 and newer released versions (up to version 2010.2.0-p1) were tested, but no successful wind tunnel simulation could be reached. Therefore it was decided to define the wind tunnel outlet condition in such a way that the reference point in the middle of the tunnel in the test section reached the requested velocity.

Beside that the "reference velocity" setting for the wind tunnel outlet it had to be defined, the "Sutherland reference viscosity" in the \*.para file also had to be set. This value was changed in order to adjust the viscosity to fit a needed Reynolds number.

$$Re = \frac{\rho_0 \cdot V_0 \cdot l}{\mu_0} \quad (17)$$

Where  $Re$  is the Reynolds number,  $l$  is the Reynolds reference length,  $\rho_0$  is the density of the free stream,  $V_0$  is the free stream velocity and  $\mu$  is the viscosity of the free stream medium.

The value of  $l$  was chosen to be 1.0m, as for wind tunnel measurements the test section diameter or a relation of the square cross section area is used instead of any reference length of the tested model. TWG has a test section area of 1.0m x 1.0m, without consideration of the used ramp.



### 3.5 Post Processing

When the values of the variables defined in the \*.para file had been found, the different geometries could be submitted to a specified number of processors.

Shown below is the pressure distribution and Mach number in the tunnel for a configuration with Mach number 0.8 above the inlet in the test section.

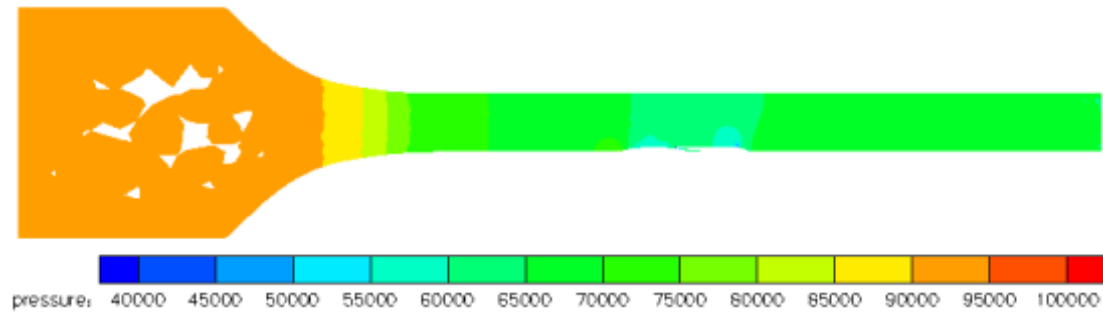


Figure 3.30

Side view of the wind tunnel showing the pressure distribution in Tecplot 360

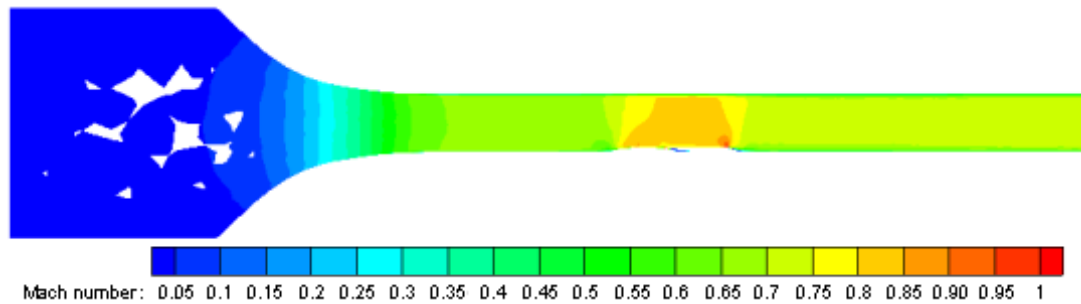


Figure 3.31

Side view of the wind tunnel showing the Mach number in Tecplot 360

The boundary layer thickness was investigated with usage of Tau.BL to verify that the prismatic layers cover the boundary layer. This investigation showed that the boundary layer was thicker than the prismatic layers at some points in the mesh, resulting in some additional adjustments. This can be seen when comparing the last and second last pictures in Figure A.3.11 in Appendix A3.

The residual of the calculations in TAU is a measure of the accuracy of the solution. The numerical residual represents the numerical rest terms after each iteration step. A smaller value indicates higher accuracy. The inlet presence has a great impact on the accuracy of the numerical solution. This influence is mainly due to two circumstances: first, the additional boundary condition "outlet" for the NACA inlet configuration makes it more difficult for the solver to get a converged solution. Additionally, the NACA inlet itself has an immense physical influence on the flow. Beside wakes outside and inside the NACA inlet, it is also difficult for the TAU solver to simulate the low flow velocities ( $\text{Mach} < 0.15$ ). In Figure 3.32 and 3.33 are seen residual plots for a clean wind tunnel setup and a wind tunnel setup with an inlet, respectively.

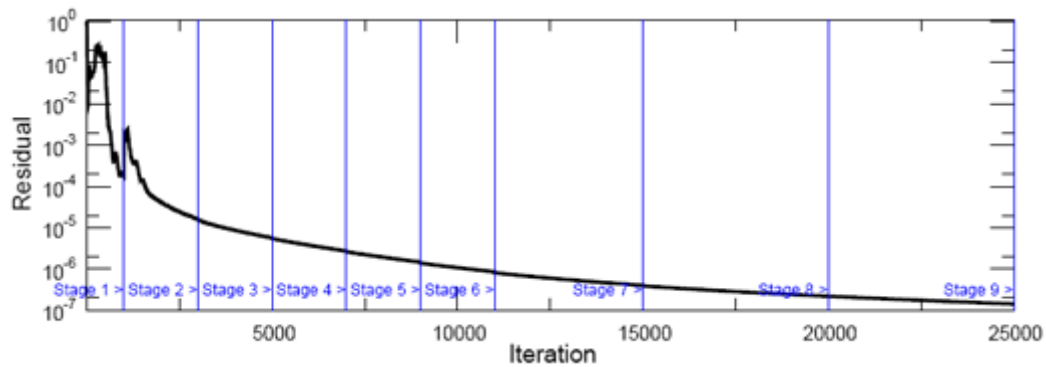


Figure 3.32

Residual plot for the clean wind tunnel setup. From 0 to 25 000 iterations.

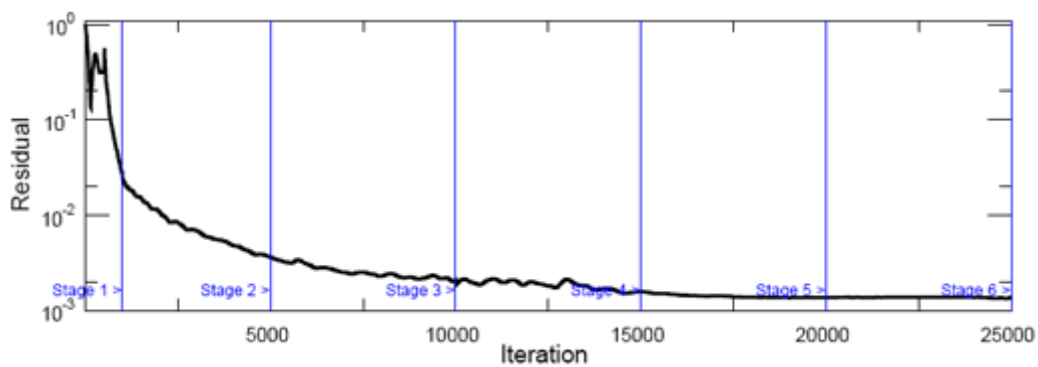


Figure 3.33

Residual plot for the wind tunnel with an inlet. From 0 to 25 000 iterations.

It should be remarked that the numerical calculations are driven much further in view of number of iterations than can be seen in Figure 3.33. The converged solution of an inlet configuration was obtained at approximately 200 000 iterations. The residual and physical values (e.g. drag) was observed during the computations in order to secure a converged solution and therefore valuable results.

The drag of the assembly parts that were defined in CENTAUR was stated in the end of the converged TAU solution. This aerodynamic drag is splitted within TAU into two parts: pressure drag and viscous drag.

### 3.6 Empirical Method Analysis

An empirical method analysis was carried out with calculation methods described in ESDU paper 86002 *Drag and pressure recovery characteristics of auxiliary air inlets at subsonic speeds* (Reference [6]). This paper is based on experimental results and allows for an estimation of inlet drag and ram pressure efficiency for different inlet configurations at subsonic speeds. Results obtained with this method serve as comparison values for the results obtained by means of Computational Fluid Dynamics. Unfortunately, the method found in Reference [6] is only valid to describe an inlet with a constant ramp angle. As seen in Figure A.2.13 - A.2.16 in Appendix A2, of the inlets investigated in this report only the inlet with a ramp angle of 7 degrees has a constant ramp angle. Values for this intake will be compared at Mach 0.8 which is the Mach number which has been of primary focus in this report.

The calculation of the inlet drag and ram pressure efficiency can be found in Appendix A4. To follow these calculations it is suggested to have Reference [6] available as the steps are not explained in detail. The air flow data used for these calculations were extracted from a CFD solution of the wind tunnel without the inlet at the inlet position. The results are presented below.

Mass Flow (kg/s)	Mass Flow Ratio	Drag (N)	Ram pressure efficiency
0.10	0.357	23.2	0.682
0.15	0.497	29.5	0.653
0.20	0.659	38.8	0.638
0.25	0.805	50.8	0.635

Table 3.2

Inlet drag and ram pressure efficiency estimated with the help of ESDU paper 86002 [6]

A software called RAMAIR available for calculating drag and ram pressure efficiency based on Reference [6]. However, it was decided not to use this software within this thesis. When RAMAIR computes the value of drag and efficiency for a specific mass flow, it adapts the geometry to the most efficient geometry. Thus values were given for geometries not investigated in this report.



## 4 Results and Discussion

### 4.1 Pressure and Mach number Analysis

In this section the physical flow features of the NACA inlet are analysed. For the most figures, the inlet with a 7 degrees ramp angle is used to illustrate the flow effects.

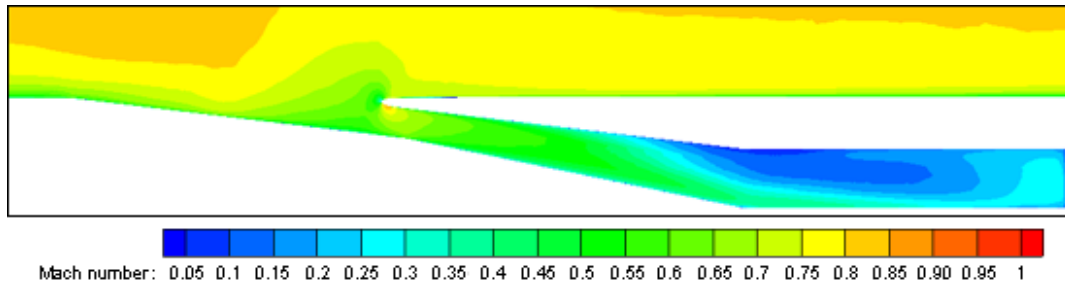


Figure 4.1

Side view in the symmetry plane of the inlet showing the Mach number  
Mach 0.8. 7 degrees ramp angle. Mass flow: 0.20 kg/s

It can be seen in Figure 4.1 that the Mach number is decreased in the area outside of the inlet. The region of low velocity flow closest to the wind tunnel surface is thinner aft of the inlet lip as most of the boundary layer has been sucked in by the inlet.

At the lip of the inlet a local region can be observed where the flow velocity is decelerated. Even if it is not clearly seen in Figure 4.1, there is also a stagnation point at the lip. Along the bottom side of the lip there is an acceleration of the flow and in a small area the velocity is above that of the free stream.

As the air flows further down into the diffuser the velocity of the flow becomes more uniform. As the air is lead through the inlet and down into the diffuser it will have a velocity component downwards. When the flow reaches the end of the diffuser and into the plenum, which is parallel to the wind tunnel floor, the flow will initially be located mostly in the lower region of the channel. This can be seen illustrated in Figure 4.6 and Figure 4.7 in the next section.

For the same configuration at a higher mass flow the air flow reaches sonic speed ( $Ma = 1.0$ ) at the beginning of the diffuser as can be seen in Figure 4.2. This reduces the total pressure of the flow and indicates that the throat of the inlet is now choking, which means that no additional air will pass the throat. At which mass flow this occurs depend greatly on the flow condition in the free stream and the pressure acting at the end of the inlet system.

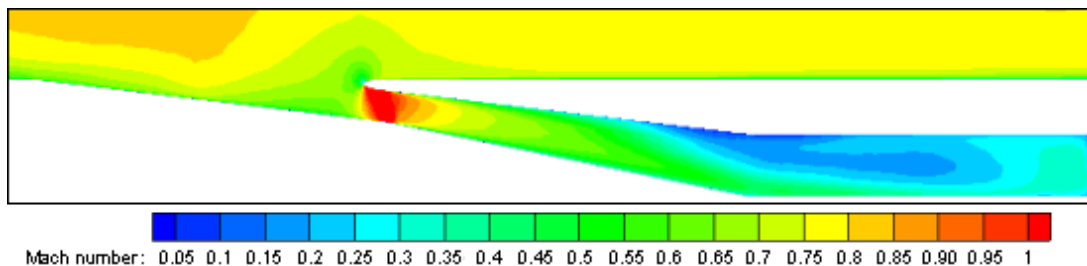


Figure 4.2

Side view in the symmetry plane of the inlet showing the Mach number  
Mach 0.8. 7 degrees ramp angle. Mass flow: 0.25 kg/s

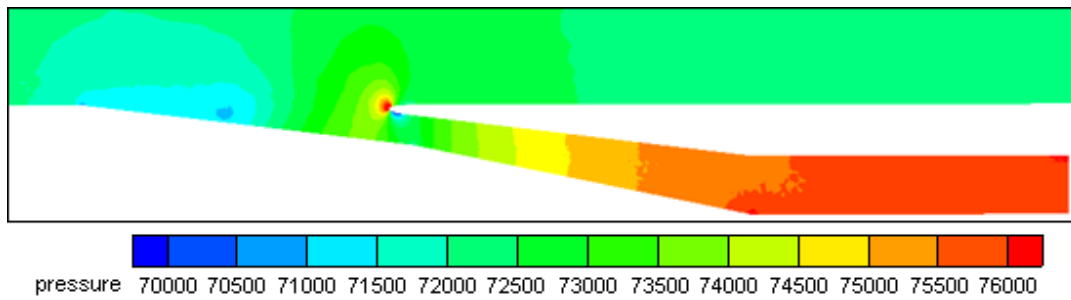


Figure 4.3

Side view in the symmetry plane of the inlet showing the static pressure  
Mach 0.8. 7 degrees ramp angle. Mass flow: 0.20 kg/s

Figure 4.3 illustrates a great increase of static pressure at the stagnation point of the inlet lip. This figure also shows that the static pressure rises along the flow direction within the diffuser. This effect is due to the reduction of the flow velocity within the diffuser while the total pressure is nearly constant, as it is seen in Figure 4.4.

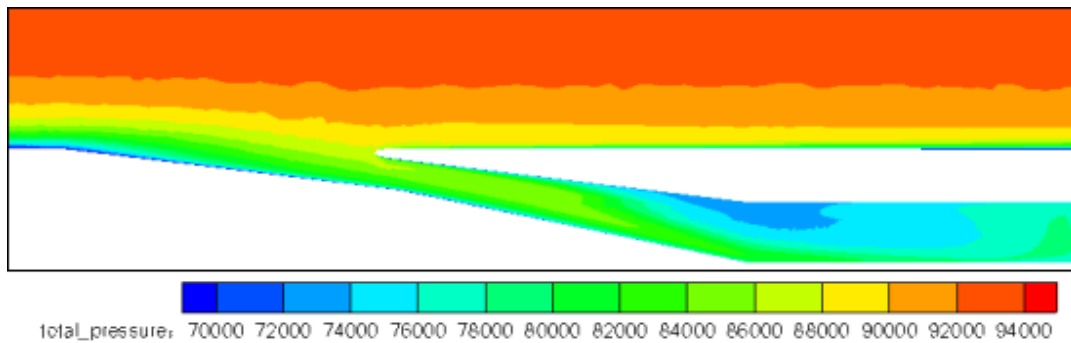


Figure 4.4

Side view in the symmetry plane of the inlet showing the total pressure  
Mach 0.8. 7 degrees ramp angle. Mass flow: 0.20 kg/s

Figure 4.4 shows an expected behaviour of the total pressure: In general, the total pressure is lower with approximation to any surface. This effect is mainly caused by the friction of the surface. In Figure 4.4 is also seen the influence of the NACA inlet on the total pressure. It should be remarked that the total pressure and static pressure in combination give an overall picture of the situation, since  $P_{tot} = P_{stat} + P_{dyn}$ .

When the total pressure within the inlet and channel is nearly constant while the static pressure is increasing, it means that the dynamic pressure is decreasing. This was also expected since the flow velocity is decreasing as the flow drives through the inlet and diffuser.

## 4.2 Boundary Layer Analysis

As a part of this thesis the boundary layer before, inside and aft of the inlet is analysed. The air flow into the inlet can be illustrated with the help of streamtraces placed in the free stream prior to the inlet. A streamtrace is the path of a massless particle placed in the free stream. These streamtraces show how the air closest to the wind tunnel surface flows into the inlet.

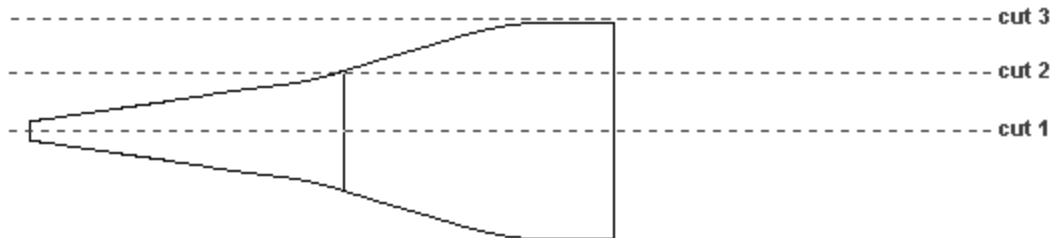


Figure 4.5

Top view of the inlet with the positions of the cuts shown in Figure 4.6 - 4.8.

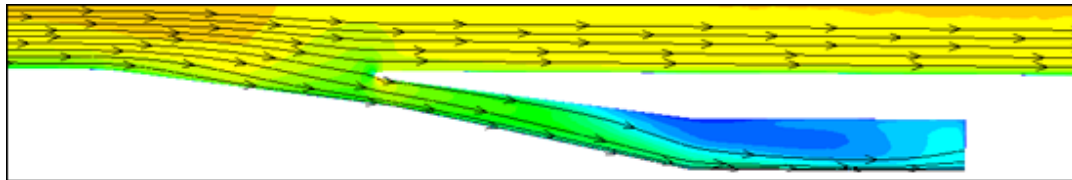


Figure 4.6

Side view in the symmetry plane of the inlet with streamlines. Cut 1

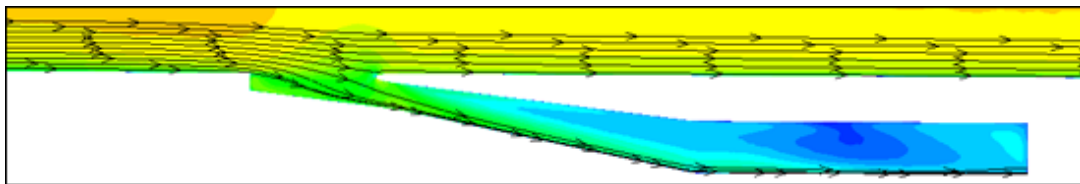


Figure 4.7

Side view of the inlet 19 mm to one side of the symmetry plane. Cut 2. Total width of inlet is 75 mm

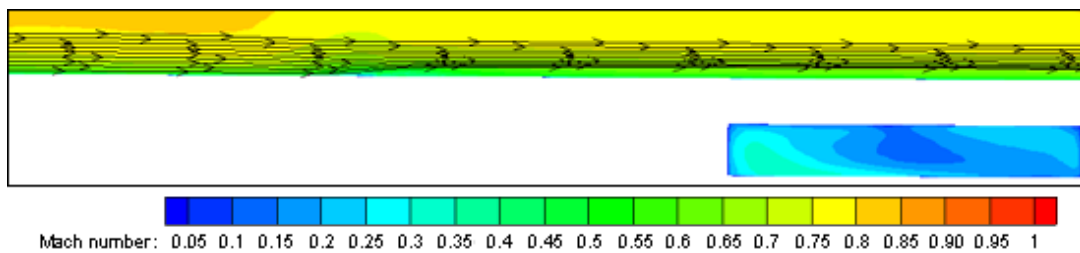


Figure 4.8

Side view 38 mm to one side of the inlet symmetry plane. Cut 3. Total width of inlet is 75 mm

In Figure 4.6 the air flow at the surface and a relatively large region away from the surface is sucked into the inlet. In the next figure, Figure 4.7, a smaller region of air enters the inlet compared to at the symmetry plane of the inlet shown in Figure 4.6. The influence region of the inlet is smaller compared to the symmetry plane (cut 1). In Figure 4.8 the flow is not seen to

enter the inlet, however, at the inlet lip the flow is diverted upwards. An explanation for this can be the presence of vortices in this area that are originated by both outer edges of the lip.

The velocity profile in the boundary layer was investigated with use of Tau.BL and Tecplot 360 to visualise the influence of the NACA inlet on the boundary layer. For this, the boundary layer velocity profile was compared between the clean wind tunnel set-up at Mach 0.8,  $Re 10 \cdot 10^6$  and a typical NACA inlet configuration (7 degrees ramp angle, mass flow = 0.20 kg/s) at the same condition. The boundary layer velocity profile was extracted at five positions:

- 260 mm prior to the inlet
- 50 mm prior to the inlet
- 15 mm aft of the lip of the inlet (at the inlet throat plane)
- Inside the inlet at the inlet throat plane
- 285 mm aft of the lip of the inlet

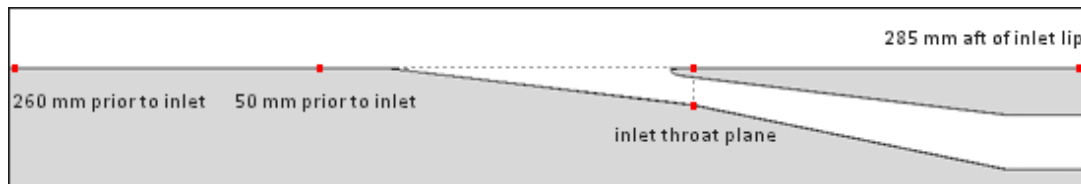


Figure 4.9

Side view of the inlet with points showing the positions investigated in Tau.BL and Tecplot 360

In Figure 4.6 one of the streamtraces placed is close to being the dividing streamline of the flow that enters the inlet. The height of the dividing streamline was estimated to be 20 mm at a distance of 50 mm prior to the inlet. In Figure 4.11 it can be seen that the boundary layer at this point is approximately 40 mm. It is worth to notice that the velocity profile extracted with Tau.BL only covers the height of the boundary layer, while the values extracted with Tecplot 360 in some cases show the velocity profile for a larger portion of the flow.



260 mm prior to the inlet the flow is still undisturbed by its presence as it is seen in Figure 4.10. The boundary layer profile for the clean wind tunnel and the wind tunnel with an inlet present coincide.

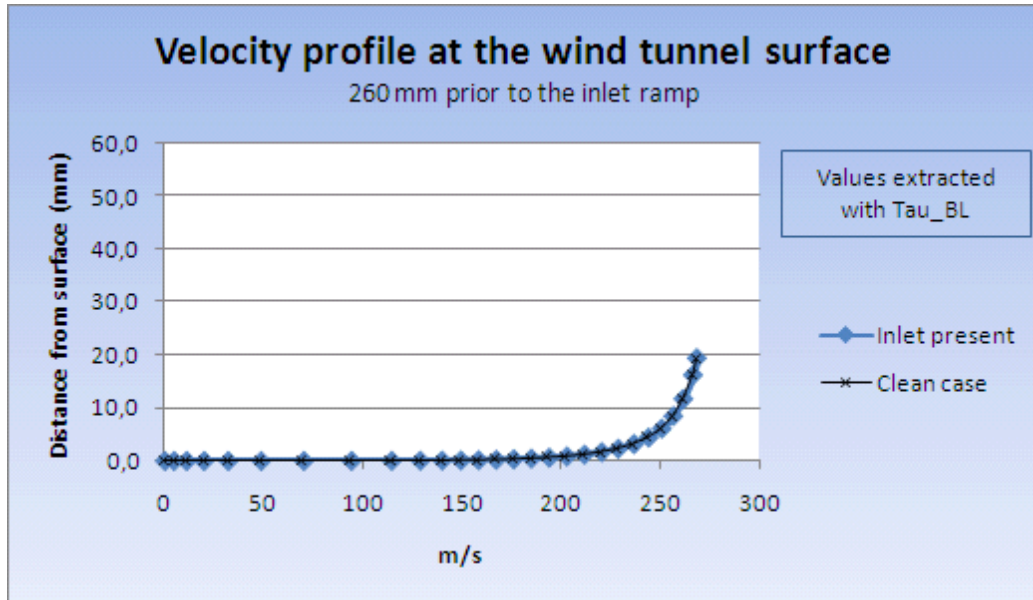


Figure 4.10  
Velocity profiles 260 mm prior to the inlet

An effect of the presence of the inlet can be seen in Figure 4.11. This boundary layer velocity profile shows the situation at a distance of 50 mm prior to the inlet. It can be seen that the boundary layer has a fuller velocity profile for the wind tunnel configuration with an inlet present. A fuller velocity profile means that the velocity value is higher than the compared clean case. As both these values were extracted with Tau<sub>BL</sub> they show the boundary layer height, which is defined to be the point where the velocity has reached 99% to that of the free stream.

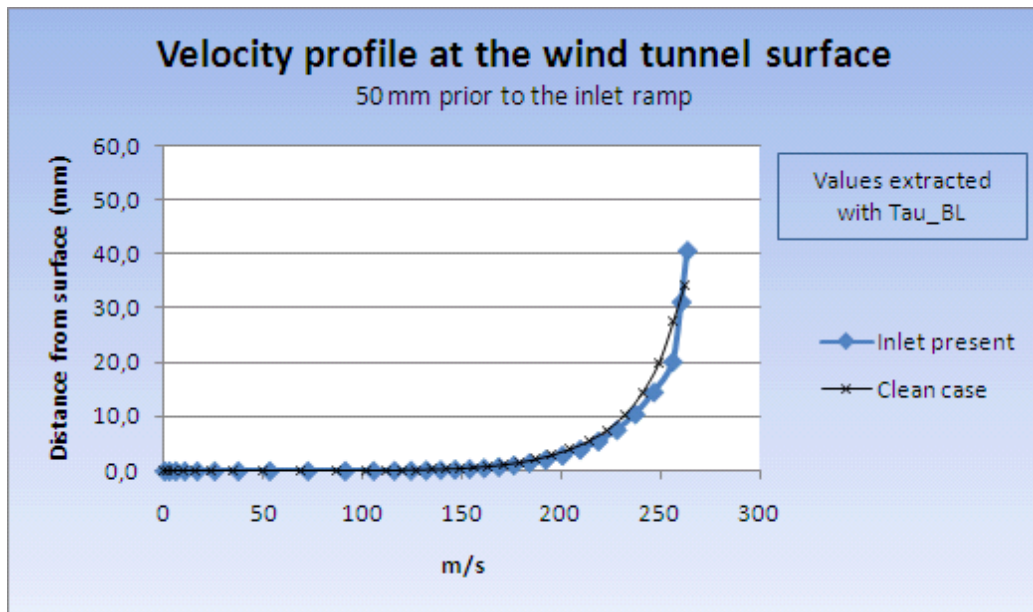


Figure 4.11  
Velocity profiles 50 mm prior to the inlet

15 mm aft of the inlet lip it can be seen that the boundary layer has grown for the clean case as to be expected. For the case with the inlet, a large portion of the low-velocity air flow has entered the inlet and a boundary layer is now growing up with a starting point at the inlet lip.

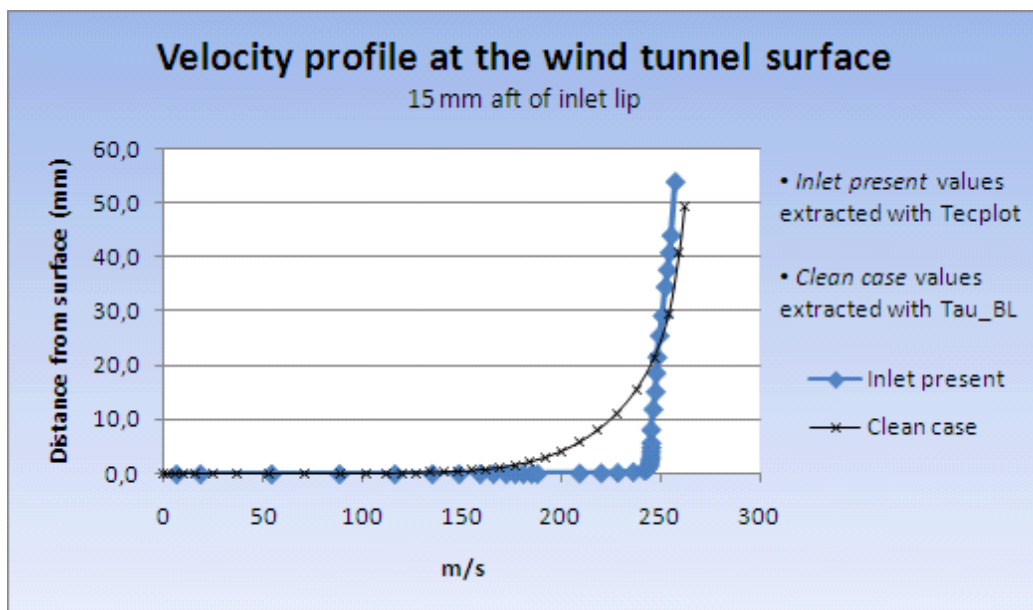


Figure 4.12  
Velocity profiles 15 mm aft of the inlet lip

In Figure 4.13 the velocity profile for the flow close to the wind tunnel surface can again be seen for the point 15 mm aft of the inlet. The distance to the surface (y-axis) is zoomed. Only the

curve representing the velocity profile with the inlet present is shown. In this figure it can be seen that the boundary layer is very thin at this point, approximately 1 mm.

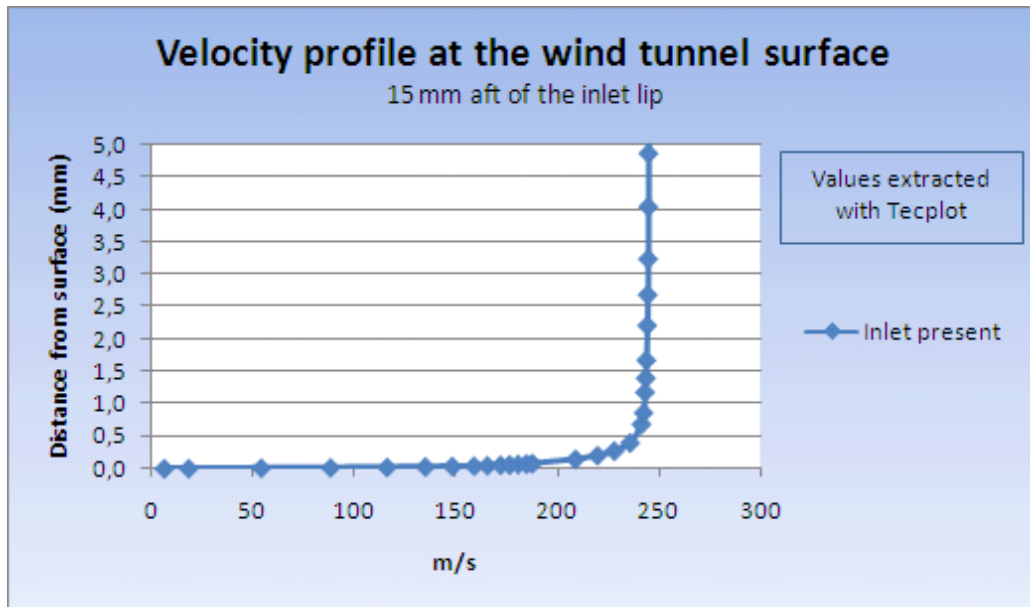


Figure 4.13  
Detailed velocity profile 15 mm aft of the inlet lip with the inlet present

A point 285 mm aft of the inlet was investigated to show that the shape and height of the boundary layer for the case with the inlet now is clearly seen in relation to the clean case. The boundary layer of the case with a NACA inlet has further developed, but a difference to the clean case is still visible. It should be remarked that the free stream velocity is slightly higher for the clean case. This is seen in the last shown point of each case (contrary to the point 50 mm prior to the inlet).

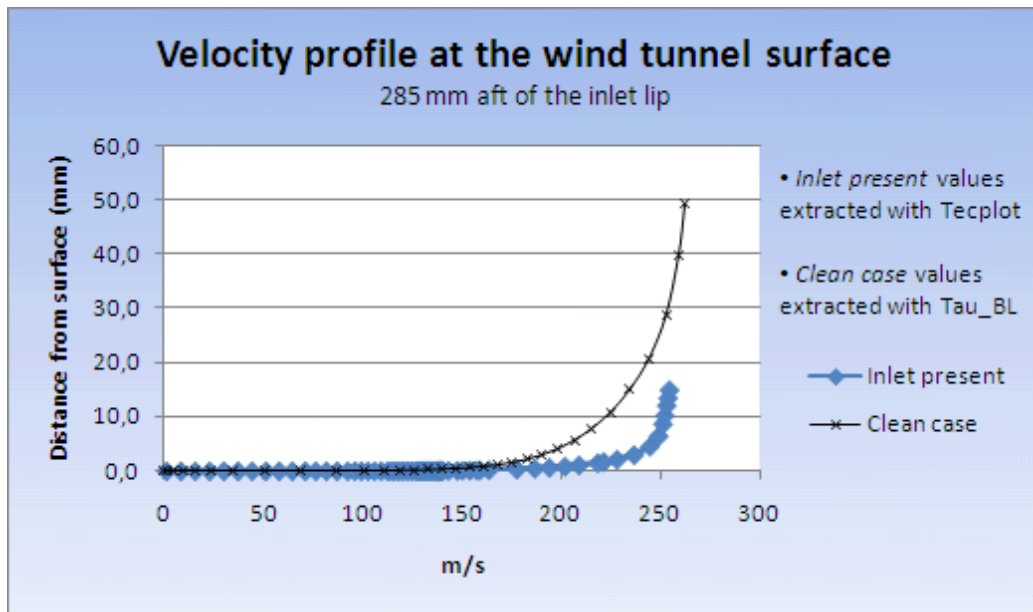


Figure 4.14  
Velocity profiles 285 mm aft of the inlet lip

The velocity profile in the inlet at the inlet throat plane can be seen in Figure 4.15. A higher velocity is seen to be in the top section of the channel. If compared to Figure 4.1 this makes sense as the velocity of the flow accelerates in this region inside the inlet just aft of the lip.

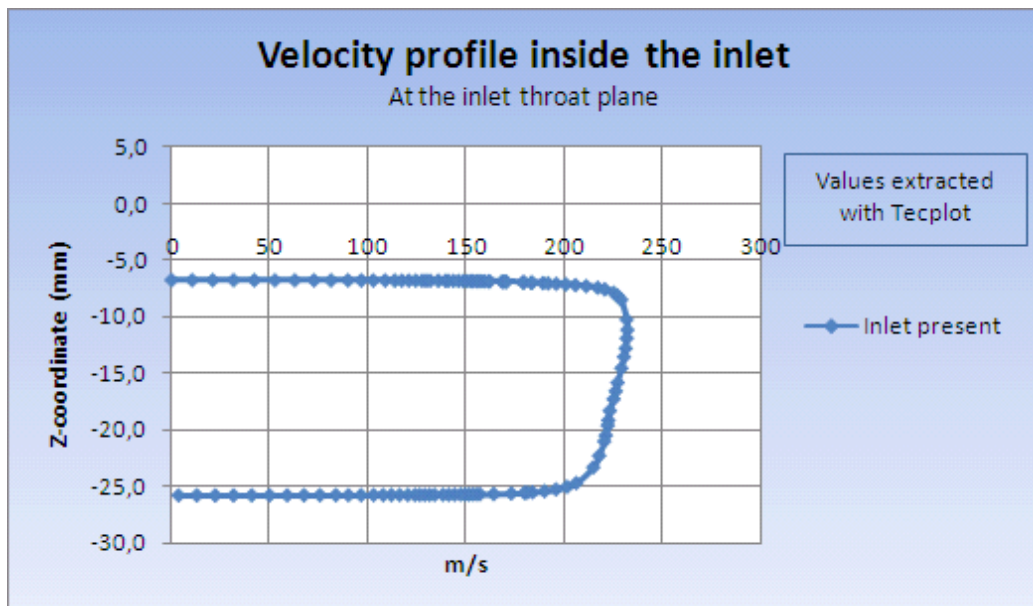


Figure 4.15  
Velocity profile inside the inlet at the inlet throat plane

### 4.2.1 Ramp wall edges

In order to investigate the effect of sharp ramp wall edges on the boundary layer air that flows over the edges into the inlet (described in section 3.1.2), streamtraces were placed on the surface prior to the inlet. This is shown in Figure 4.16 below. These streamtraces showed that with sharp edges, flow will still be going into the duct from the sides. This observation was expected, since we have a lower pressure inside the duct than outside, driving the flow.

In Figure 4.16 is also visible the influence of the wakes that enters the inlet. The placed streamlines are swirled and enter the intake section.

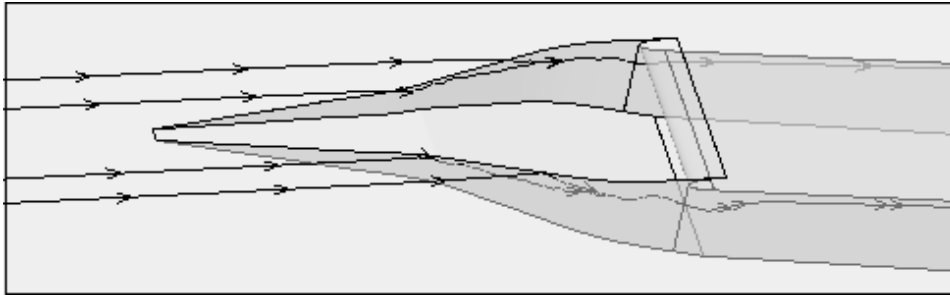


Figure 4.16

Streamtraces placed at the NACA submerged inlet from a Tau\_BL solution as seen in Tecplot 360

The loss of pressure described in Reference [15] was discussed with Reference [24] and the agreed interpretation was that the loss of pressure resulting from rounded edges was due to the vortices not forming along the rounded ramp edges.

### 4.3 Ram Pressure Efficiency

The ram pressure efficiency is used in this report to judge the effectiveness of the investigated air inlet. The values obtained for this parameter can be compared to earlier studies and additionally, this comparison is also a check of the reliability of the results.

The turbulence model used in this thesis was the SAE (Spalart-Allmaras with Edwards modification) model. The subject of this thesis was an investigation of the inlet efficiency, not a study of different turbulence models. A previous study, Reference [1], made a similar investigation of NACA inlets at low speed using the TAU RANS solver. Reference [1] investigated two different turbulence models and compared the results to NACA experimental results. The comparison can be seen in Figure 4.17.

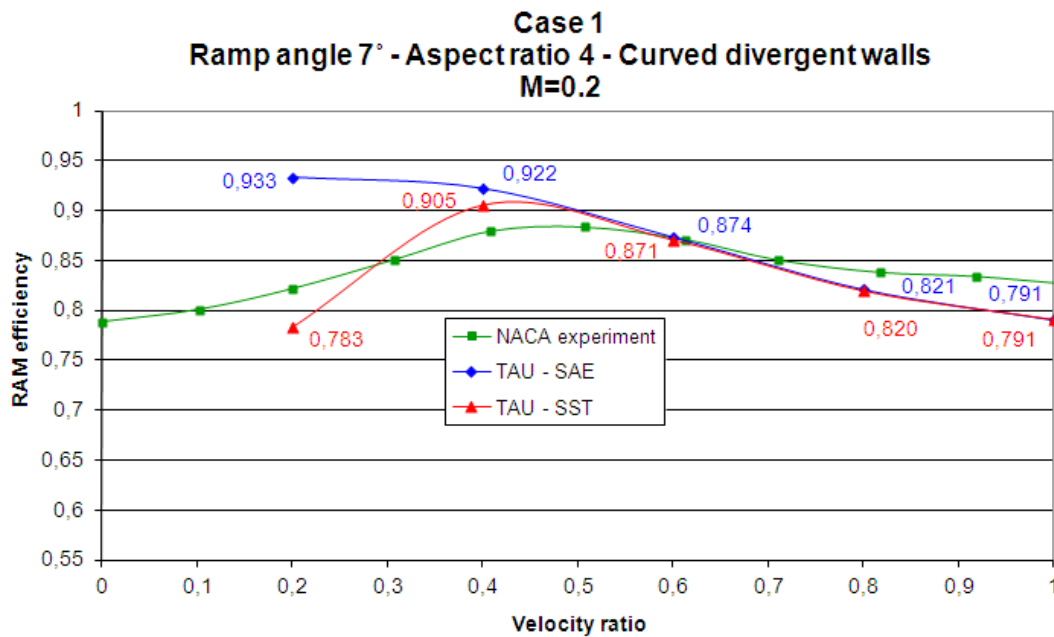


Figure 4.17

Ram pressure efficiency comparison at Mach 0.2 for different turbulence models  
NACA experimental results graph has been adjusted. Figure from Reference [1]

It can be seen that for velocity ratios greater than 0.4 there is very little difference in the results obtained with the applied turbulence models. For lower velocity ratios the SST turbulence model comes closer to experimental results. All results evaluated in this thesis, except for on one occasion (7 degrees ramp angle, 0.10 kg/s mass flow, Mach 0.8) have a velocity ratio greater than 0.4. Therefore the SAE turbulence model was chosen. Another reason for choosing the SAE model was because of the higher experience reliability with this model. It is also known to be robust and fast convergent.

The RANS solver results of this thesis were compared to own estimations, based on ESDU paper 86002 (Reference [6]). This method is based on NACA experimental results and takes among others, following parameters into account: the geometry of the inlet, the free stream velocity and the boundary layer thickness. Even though ESDU method is proven to predict the main flow physics, previous studies [25] have shown an off-set in results between ESDU and CFD obtained results. With this in mind it can be expected that the results in this thesis will differ in some degree to ESDU results.

An additional comparison is made to values obtained with a different flow solver (Star-CCM+ v.4.06) for the same NACA inlet geometry placed in the same wind tunnel (TWG) as investigated within this thesis.

The results have been compared for one geometry, the seven degrees constant ramp angle. The comparison has been limited to this geometry because the method described by ESDU is only valid for a constant ramp angle. That angle is the selection 7 degrees ramp case.

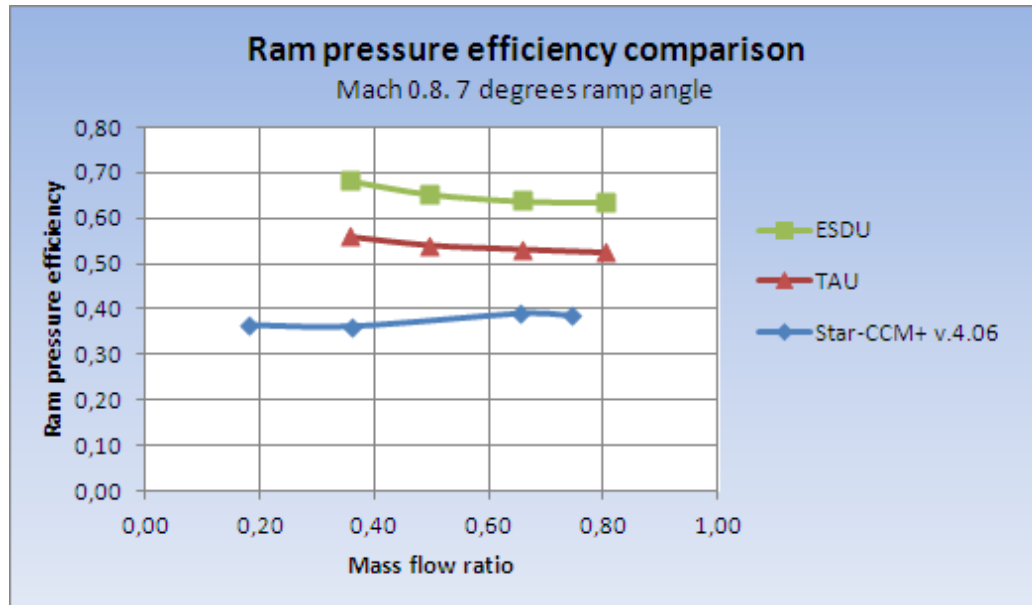


Figure 4.18

Ram pressure efficiency comparison for different estimation methods

It can be seen that ESDU predicts a higher ram pressure efficiency than TAU. The tendency of the curve does however seem to be very similar.

Star-CCM+ predicts an even lower efficiency for the same conditions. It is expected that this lower ram pressure efficiency in some extent can be explained by the presence of the (unheated) heat exchanger after the plenum. The heat exchanger represents for the internal flow another change of the flow direction and hence another reduction of the flow velocity. This effect is expected to influence the upstream flow and therefore also the Ram pressure efficiency. It is difficult to judge the influence of that heat exchanger. This influence will be cleared by a successive TAU CFD investigation that will contain heat exchanger and RAO (ram air outlet). Additionally, the TWG wind tunnel campaign in autumn 2011 will contribute to this subject.

Figure 4.19 shows a comparison for Star-CCM+ and TAU for all ramp angles investigated. It can be seen that compared to the results obtained with Star-CCM+ the results obtained with TAU does not show a great reduction of ram pressure efficiency for different mass flows. This could also be an influence of the heat exchanger and RAO, that might be more sensitive to very low internal flows.

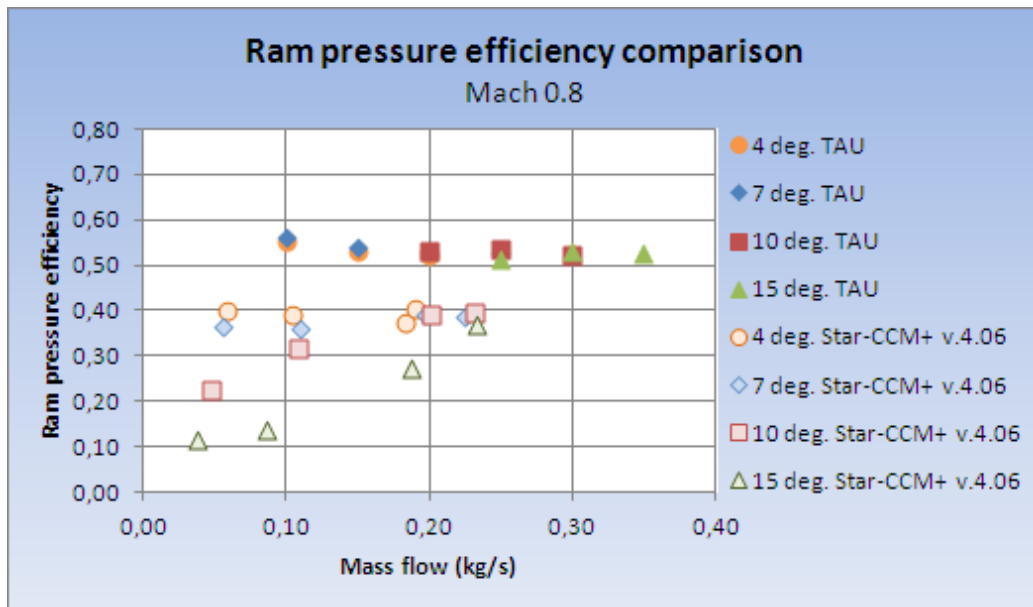


Figure 4.19  
Ram pressure efficiency comparison for different mass flows

Figure 4.20 shows a comparison of TAU results on RAM pressure efficiency between the four different ramp angles investigated in this report at Mach 0.8. In the graph a local maximum of the ram pressure efficiency can be seen for the 10 and 15 degrees ramp angle in the middle of the simulated mass flow values. Contrary, for inlet ramp angles 4 and 7 degrees the most efficient regions seem to be at lower mass flows.

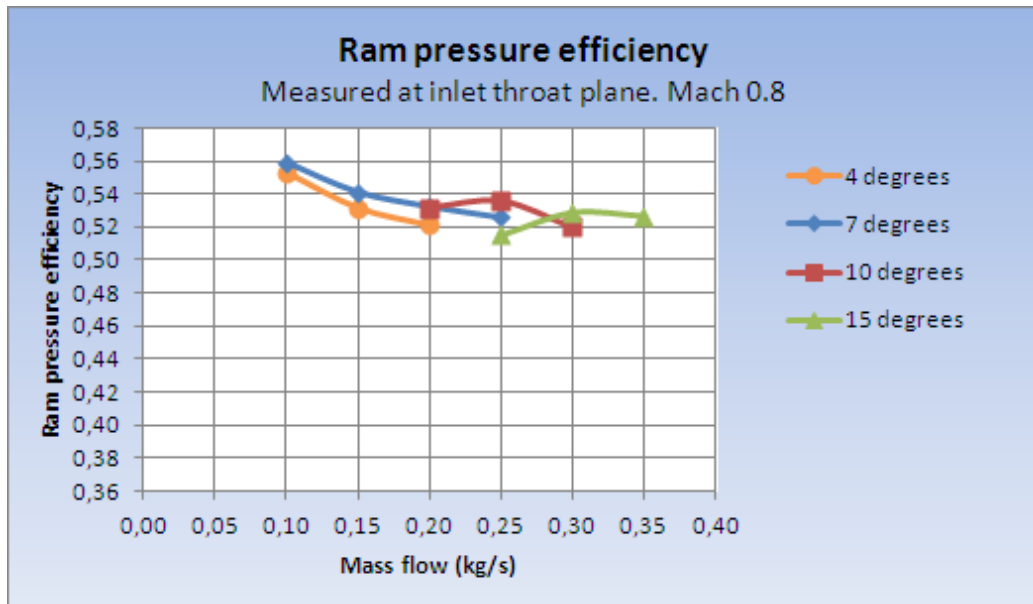


Figure 4.20  
Ram pressure efficiency for different inlet ramp angles in relation to the mass flow



#### 4.4 Ram Recovery Ratio

The investigation of pressure loss was extended up to the diffuser. This ratio is named ram recovery ratio. It can be seen in Figure 4.21 that the total pressure is decreased more over the diffuser with increasing mass flow and reduced ramp angle. The reduction of ramp angle is directly connected to the angle between the upper and lower diffuser walls. A small inlet ramp angle is followed by a larger diffuser angle than at higher inlet ramp angles. The lower ram recovery ratio after the diffuser for smaller ramp angles can be explained by the small inlet throat area followed by a large diffuser angle.

Table A.5.2 in Appendix A5 shows the diffuser angles for the different inlet ramp angles.

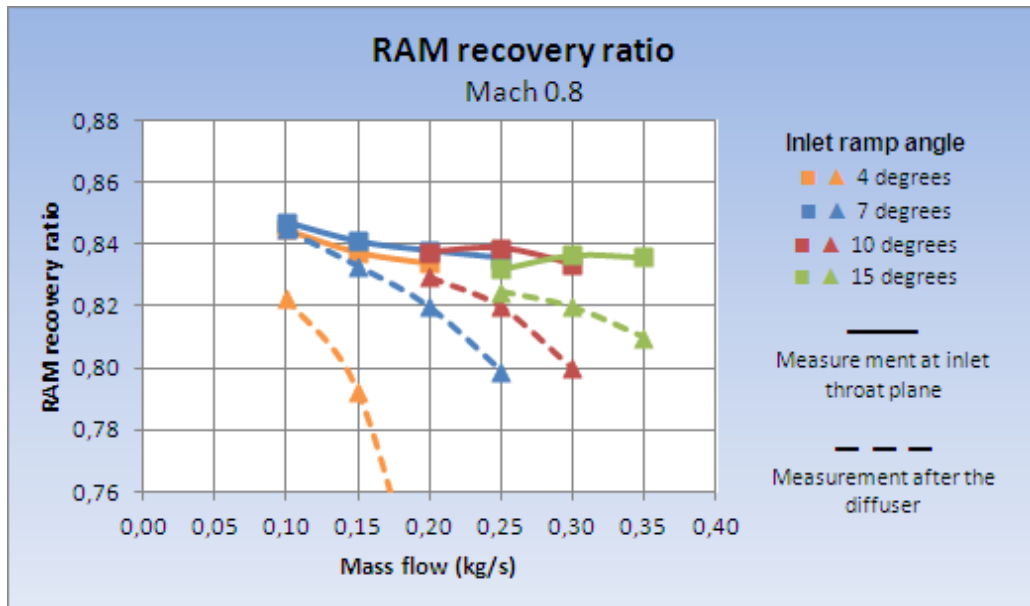


Figure 4.21

Ram recovery ratio for different inlet ramp angles in relation to the mass flow

## 4.5 Drag investigation

The drag output from the flow solver TAU is given separately as pressure drag and viscous drag for different assembly parts. The assembly parts were defined according to how they were grouped together in CENTAUR. The naming and definition of the different sections in this thesis can be seen in Figure 4.22 and Figure 4.23.

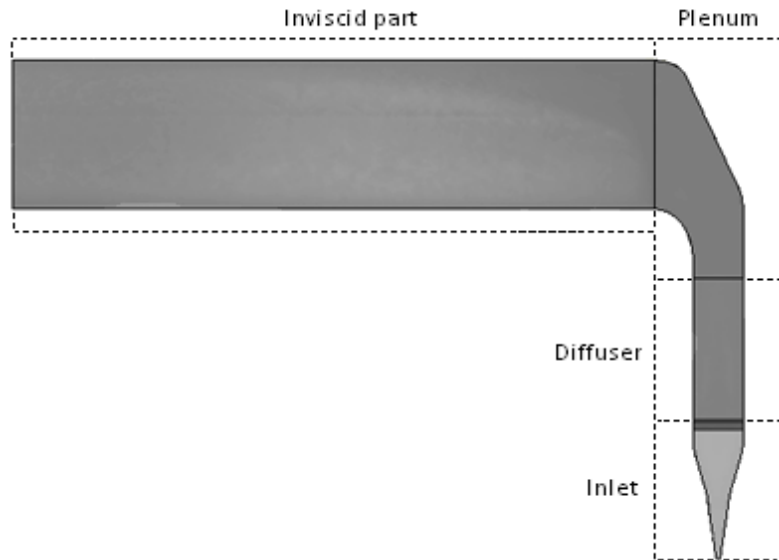


Figure 4.22  
Naming of the different inlet system assembly parts in this thesis

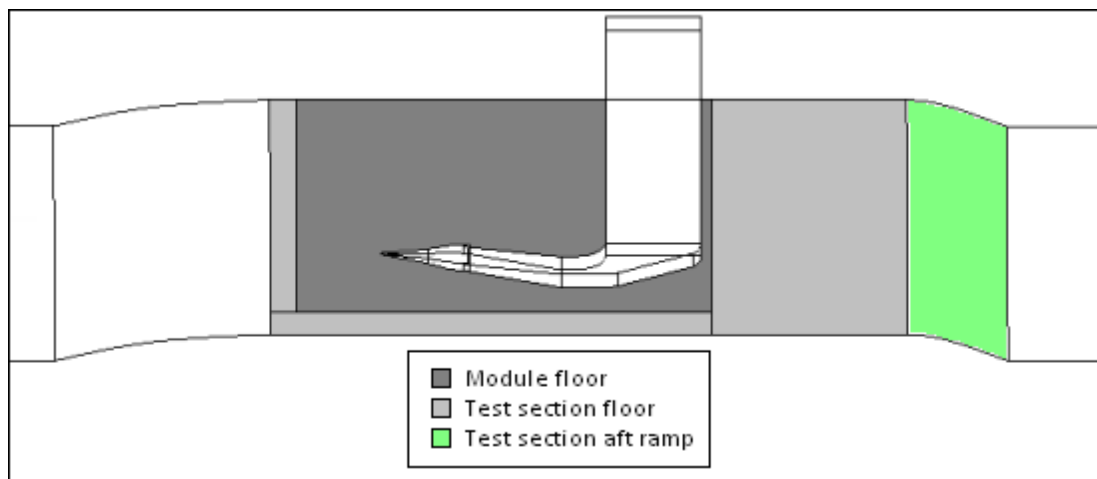


Figure 4.23  
Naming of the wind tunnel test section parts in this thesis

The drag output of from TAU is given as a drag coefficient  $C_D$ , based on the reference area in the TAU input file. This value can be reconverted into drag in Newton with the use of Equation (1) in this thesis. The values needed to use this equation are additionally the reference area, reference velocity and reference density that were defined in the TAU input.

When calculating the drag caused by only the inlet, the drag of the *inlet* assembly component was included as well as the resulting increase of drag on the *module floor* and *test section floor*.

When calculating the drag caused by the inlet system, the included parts are the *inlet*, *diffuser*, *plenum*, *inviscid part* and the resulting increase of drag on the *module floor* and *test section floor*.

When comparing values to ESDU it must be remembered that ESDU estimates the drag caused by the presence of the inlet only. None of the other inlet system parts and surrounding surfaces are considered within the ESDU method. Figure 4.24 shows the comparison of the investigated assembly parts for TAU vs. ESDU.

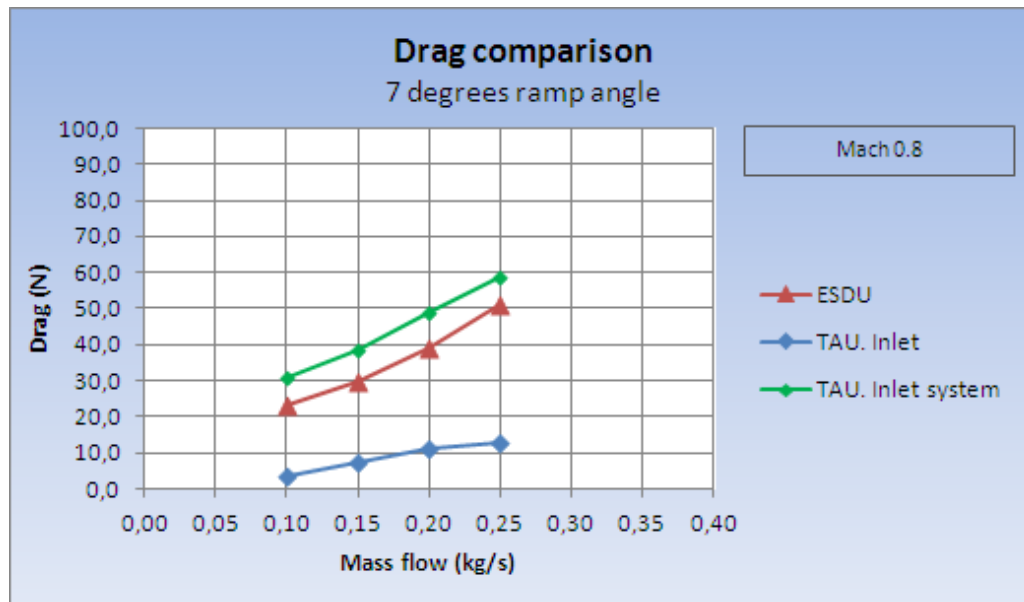


Figure 4.24

Drag comparison for the 7 degrees ramp angle configuration

It is seen a big difference in the results of both methods. The discrepancy between the TAU RANS solver and the ESDU method can be explained by that ESDU consider the inlet but also include drag terms that are derived by the inlet presence. The drag terms are ram drag, spillage drag and skin friction drag. Within ESDU any influence downstream of the inlet itself is not included. Therefore the bend of the plenum is ignored within ESDU.

In contrast to ESDU, with TAU it is impossible to split drag into drag components. Within TAU it is only possible to consider the drag contribution of assembly parts, as seen in Figure 4.22. These parts does contain all drag components but it is impossible to extract their contribution to the drag in detail. Therefore in Figure 4.24, the graph of ESDU should be compared with "TAU inlet system". It should be remarked that in the TAU results, the plenum bend is included. The difference between TAU and ESDU of around 9 Newton is seen to originate in some parts by the presence of the plenum bend. Moreover, similar underpredictions of ESDU were reported by Reference [24] and Reference [26] that were involved in the design process of several aircrafts and in different research projects. A similar underprediction of ESDU was observed recently in a different inlet design, where TAU RANS results coincide with a completely different RANS solver ELSA, using structured meshes.

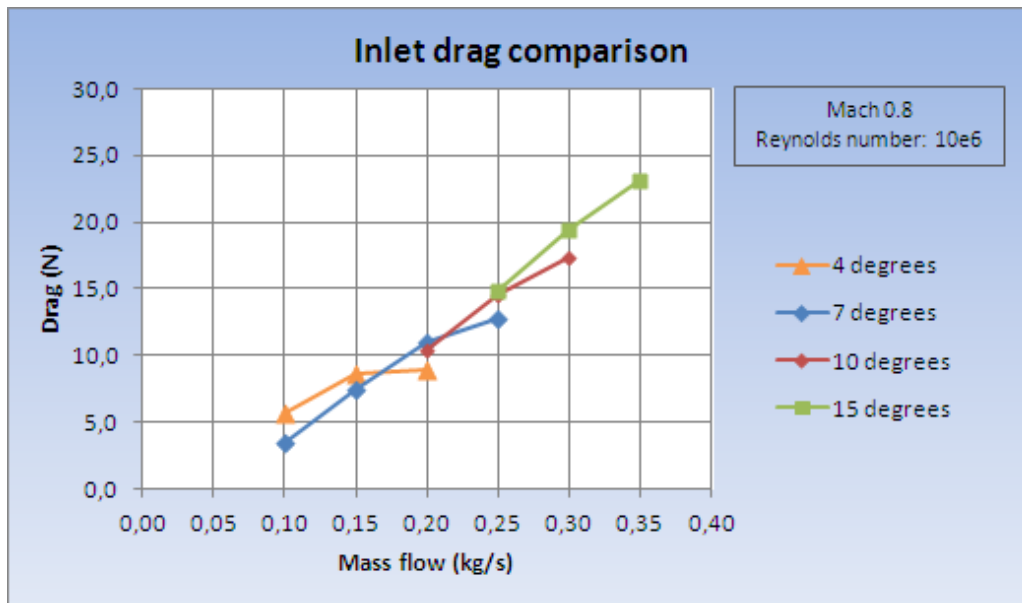


Figure 4.25  
Drag comparison for the different ramp angles at Mach 0.8

Figure 4.25 shows the drag comparison of the inlet assembly parts for different ramp angles. It can be seen in that figure that for the region of lower mass flows (0.10 - 0.15 kg/s) the 7 degrees ramp angle has the lowest drag. At 0.25 kg/s the 7 degrees ramp angle again seem to be the inlet which has the lowest value of drag, however, at this mass flow the flow inside the diffuser is  $Ma = 1.0$  as can be seen in Figure 4.26. It is interpreted from the graph in Figure 4.25 and the plot in Figure 4.26 that flow "choking" in the throat has just started at that mass flow value of 0.25 kg/s. A similar region of sonic flow is seen for the 4 degrees ramp angle at 0.20 kg/s.

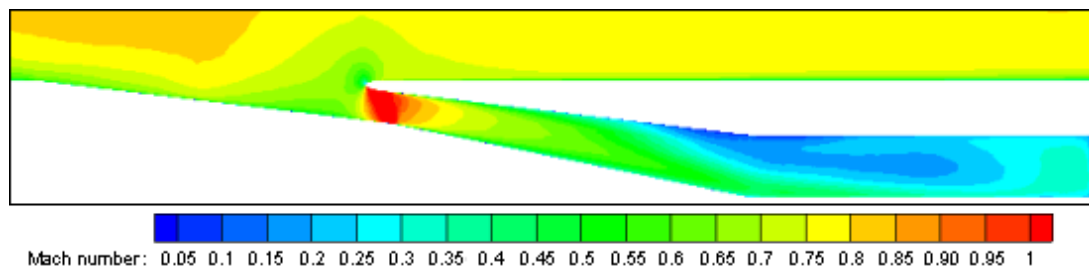


Figure 4.26  
Side view in the symmetry plane of the inlet showing the Mach number  
Mach 0.8. 7 degrees ramp angle. Mass flow: 0.25 kg/s

For an increase of the mass flow to the region of 0.20 - 0.30 kg/s the 10 degrees ramp angle has the lowest drag and therefore seems to be the best choice.

As it was discussed earlier, a more realistic consideration is seen in the drag analysis of the complete inlet system. Figure 4.27 shows this.

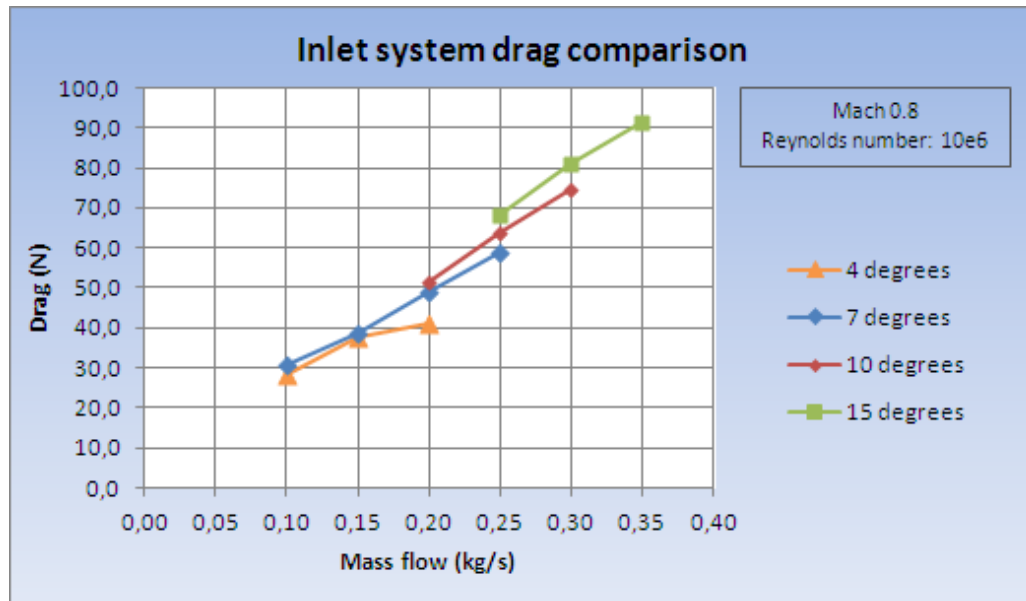


Figure 4.27

Drag comparison for the different angles for the complete inlet system at Mach 0.8

A difference that can be noted when comparing Figure 4.26 and Figure 4.27 is that the 7 degrees ramp angle seems more efficient at a mass flow of 0.20 kg/s when comparing the whole inlet system. This result is expected to be more realistic since the drag contributions of all the inlet system assembly parts are taking into account.

In Figure 4.28 is shown the comparison of the total drag for the complete inlet system for different Mach numbers. It is seen that drag increases with rising Mach numbers. This effect was also expected since the higher velocity contributes mainly additional pressure drag. The drag tendency has a linear behavior with increasing mass flow. This is valid for all investigated Mach numbers.

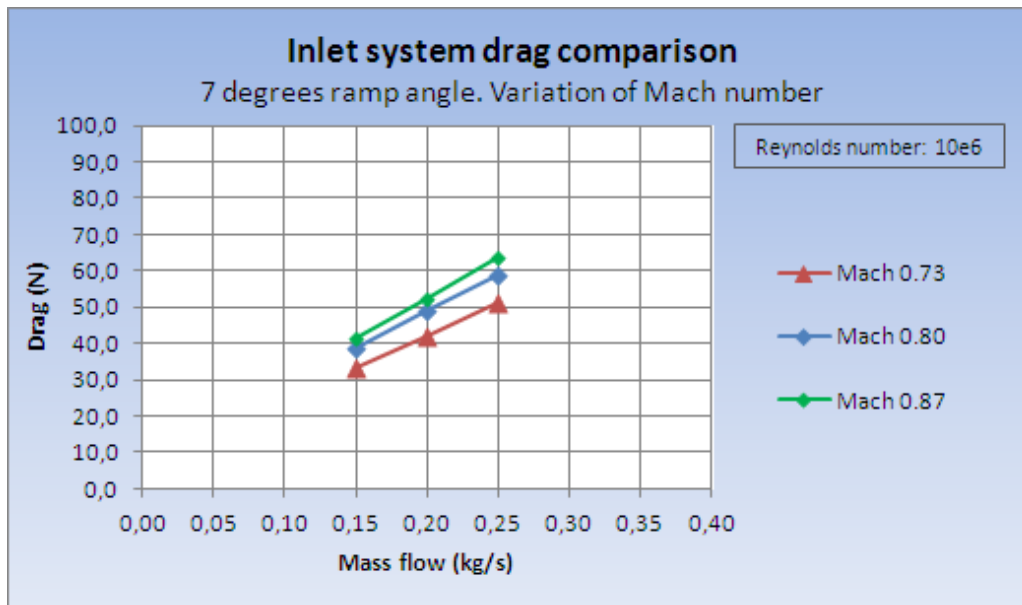


Figure 4.28

Drag comparison for 7 degrees ramp angle for the complete inlet system at different Mach numbers

Within this thesis additionally also a variation of the Reynolds number was investigated. The value of the Reynolds number used within this thesis was  $10 \cdot 10^6$ . Additionally  $5 \cdot 10^6$  and  $15 \cdot 10^6$  were investigated for a constant ramp angle of 7 degrees at Mach 0.8. The Reynolds number was varied by adjusting the viscosity of the flow medium.

In Figure 4.29 the effect of Reynolds number variation on the complete air inlet system is shown.

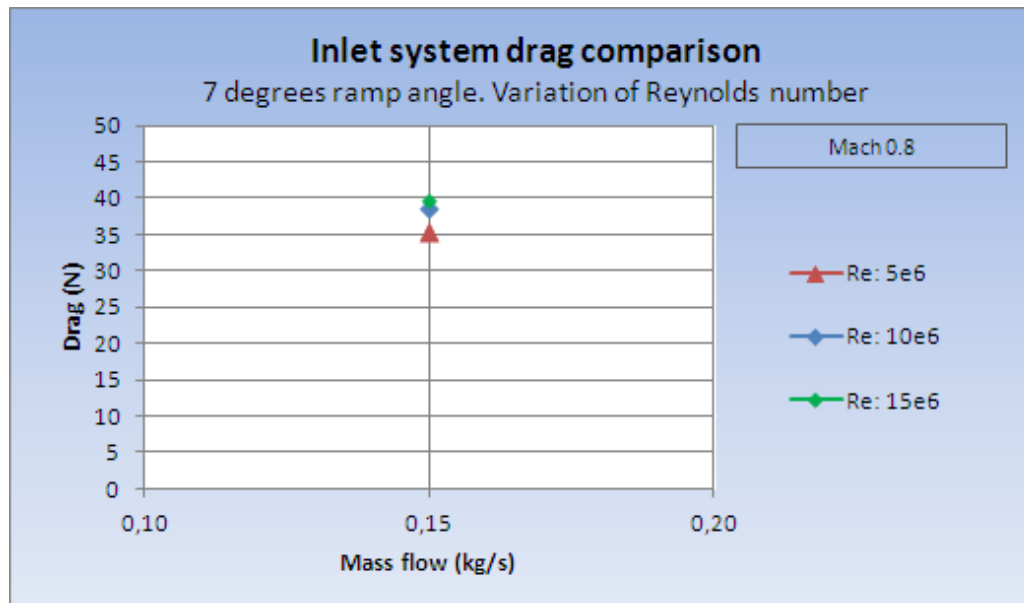


Figure 4.29

Drag comparison for 7 degrees ramp angle for complete inlet system at different Reynolds numbers

As expected, the Reynolds number influences the flow characteristics. With rising Reynolds number the dynamic viscosity decreases. At high Reynolds numbers the drag dependency on the velocity of the air is increased. When the Reynolds number is increased, the drag is increases even though the velocity of the medium is approximately the same. This increase of drag is not linear, a further increase of the Reynolds number above  $15 \cdot 10^6$  would only increase the total drag slightly.

For one case the contribution to the total amount of drag of the inlet system has been extracted for each inlet system assembly part. The case represented in Figure 4.30 is the 7 degrees ramp angle at Mach 0.8, Reynolds number  $10 \cdot 10^6$  and an inlet mass flow of 0.20 kg/s. This figure shows how the assembly parts contribute to the overall system drag. As expected, the main influence on the total drag is the pressure drag. The greatest contribution comes from the *plenum*, *inlet* and *inviscid section*, while the diffuser delivers a "negative" pressure drag for that considered ramp angle. The skin friction contributes a small component to the overall system drag.

It should be remarked that the drag contribution of the *module tunnel floor* and the *test section floor* should be seen separately within this figure. These two contributions represent the drag increase of the wind tunnel floor by the presence of the inlet.

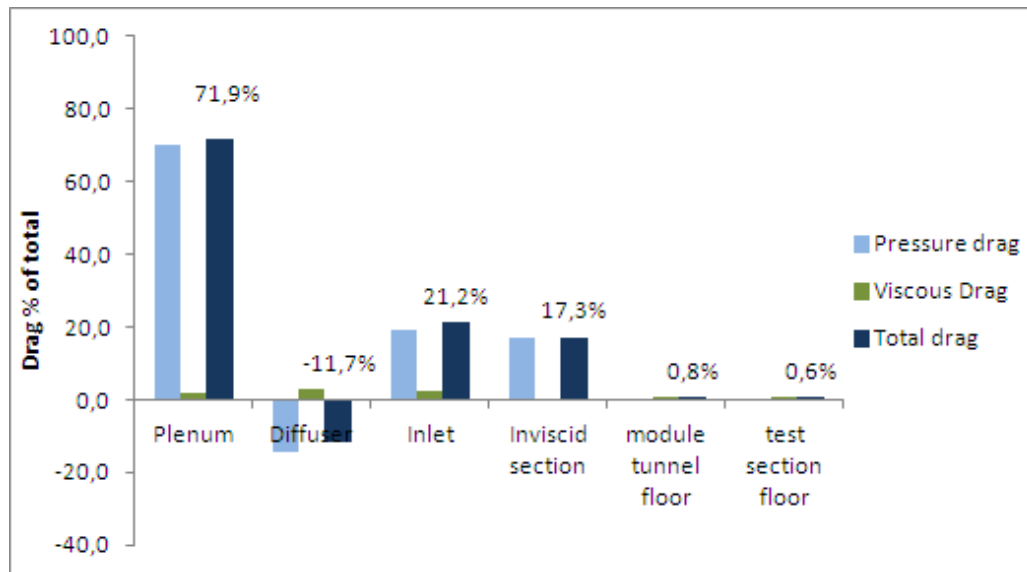


Figure 4.30

Drag contribution of different components of the inlet system and increase of drag on surrounding floor panels. Percentage of total drag.



### 4.6 Internal Air Duct After the Plenum

After the bend of the plenum the mass flow is unevenly distributed in the channel. This was expected and is due to the inertia of the flow medium as the flow is directed through the plenum bend by 90 degrees. The inertia is the resistance of an object with mass to a change of its velocity amount and/or velocity direction. The "object" is in our case any flow particle, i.e. molecules within the air. The uneven pressure distribution explains why the *inviscid part* of the inlet system (see Figure 4.22) has a pressure drag component.

The pressure distribution in the channel after the plenum can be seen in Figure 4.31 - 4.39. These figures show the results for Mach 0.8, a ramp angle of 7 degrees and an inlet mass flow of 0.20 kg/s.

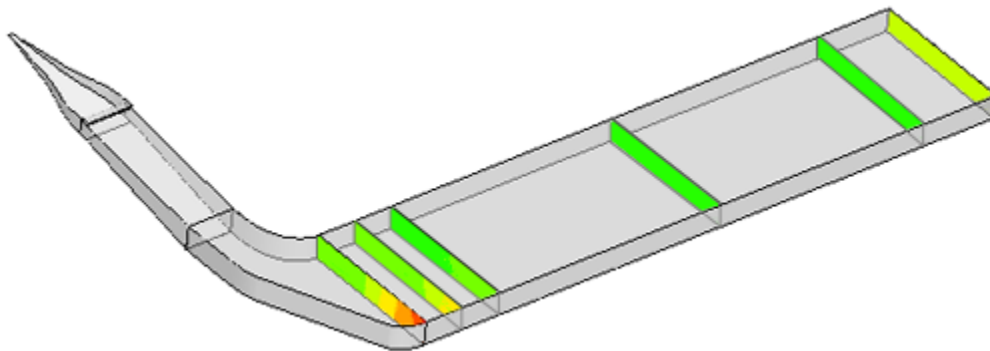


Figure 4.31  
The inlet system with pressure plots.



Figure 4.32  
Static pressure after the plenum



Figure 4.33  
Static pressure 60 mm after the plenum



Figure 4.34  
Static pressure 120 mm after the plenum



Figure 4.35  
Static pressure 480 mm after the plenum



Figure 4.36  
Static pressure 120 mm upstream  
of the inviscid "channel" exit.



Figure 4.37  
Static pressure at the inviscid "channel" exit.

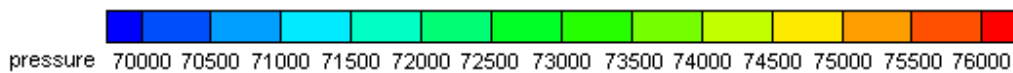


Figure 4.38  
Static pressure related to Figures 4.31 - 4.37 and Figure 4.39.

Figure 4.31 - 4.37 show how the flow within the inviscid part is harmonized. The reason for this artificially introduced inviscid "channel" for the numerical computations was to harmonize the flow up to the applied boundary condition "outlet" at the exit. This intention worked very well with the used lengths of the inviscid "channel".

It should be remarked that the slightly higher static pressure value at the channel exit (Figure 4.37) is due to the numerical set-up. The region that is influenced by the boundary condition that is applied at the channel exit, shown in Figure 4.39.

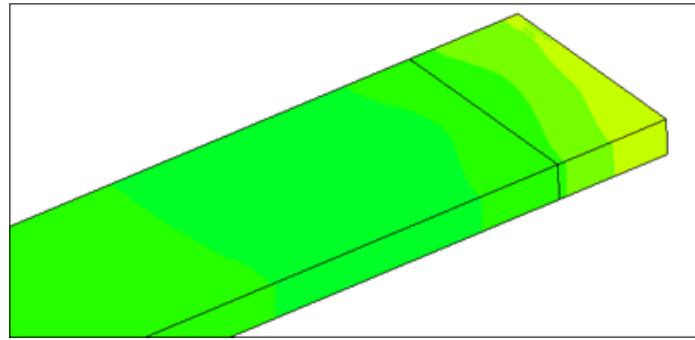


Figure 4.39

ISO view of the static pressure at the exit of the inviscid "channel".  
The location of the cut 120 mm upstream of the inviscid "channel" exit can be seen as a black line.

### 4.7 Analysis of the Vortices Formed by the NACA Inlet

In the *Preliminary Studies* section of this thesis it was mentioned that the vortices forming in the inlet increase the efficiency of the inlet. This is because these vortices reduce the thickness of the boundary layer in the inlet region and allow for high energy flow (flow outside of the boundary layer) to enter the duct. The latter can be seen illustrated in Figure 4.40.

It should be remarked that this plot represents a constant y-z plane only. This cut plane derived out of the 3-dimensional RANS solution. The visualized streamtraces within this plot will in reality flow not only top to bottom, but also streaming further in x-direction. However, this plot gives a good impression of the flow physics and also shows the internal vortices as those regions with high vorticity. A figure showing the x-coordinates in the inlet can be seen in Figure 4.47.

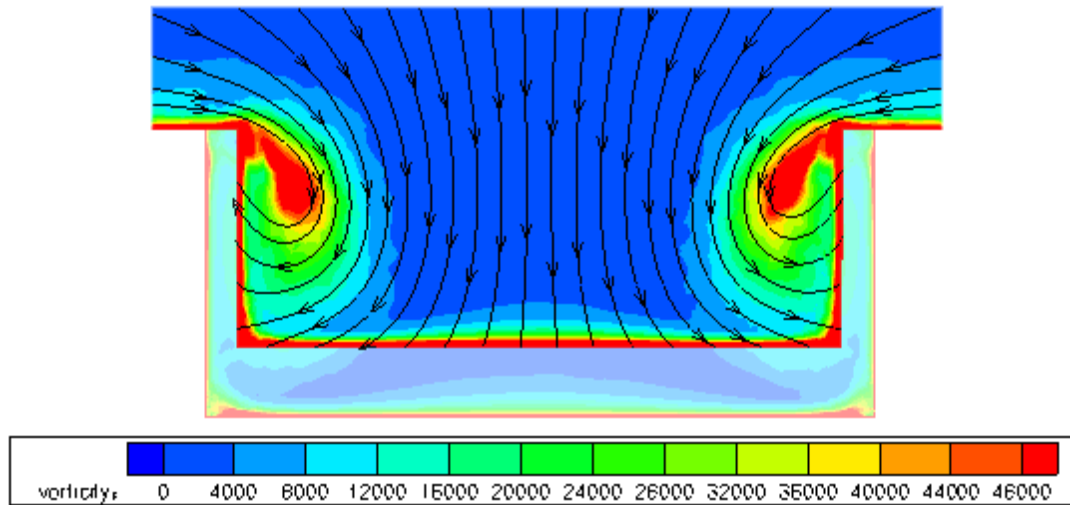


Figure 4.40

Plot of the vorticity at x-position 135 for an inlet with 15 degrees ramp angle.  
Streamtraces showing surrounding flow entering the inlet.

It was discussed in the section 3.1.3 on curved-divergent NACA inlets that the vortices formed carry a part of the boundary layer out back into the stream external to the inlet. The vortices and how a part of these vortices continue aft on the inlet on the exterior surface can be seen in illustrated Figure 4.41. This figure shows a constant pressure surface. The pressure is lowered by the vortices, and thus a surface showing the boundary of a certain pressure serves to illustrate the boundaries of the vortices. The inlet shown is the inlet with a 7 degrees ramp angle and a mass flow of 0.15 kg/s.

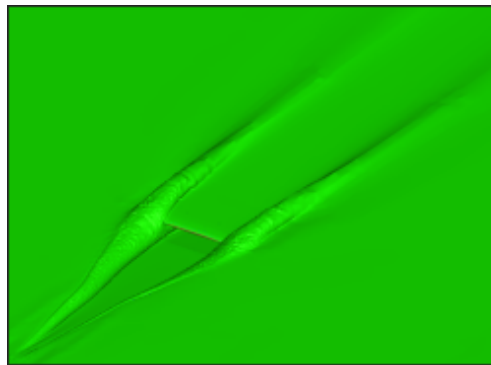


Figure 4.41  
ISO Pressure-surface 73250 Pa. Mach 0.8. Reynolds number: 10e6

Vorticity plots for 7 degrees ramp angle at Mach 0.8 and a mass flow of 0.20 kg/s.

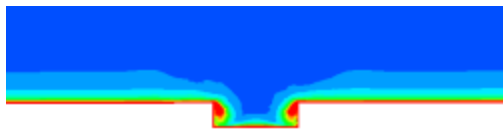


Figure 4.42  
X-position: 45

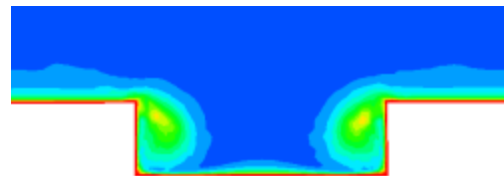


Figure 4.43  
X-position: 135

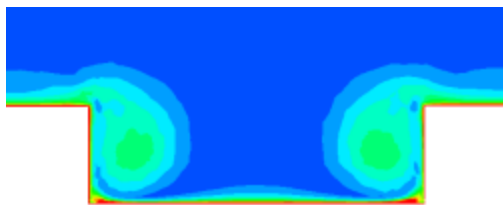


Figure 4.44  
X-position: 180

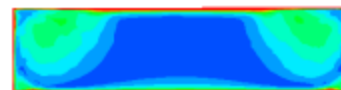


Figure 4.45  
X-position: 225

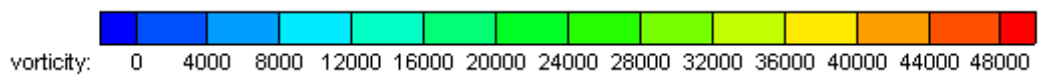


Figure 4.46  
Inlet vorticity gradient

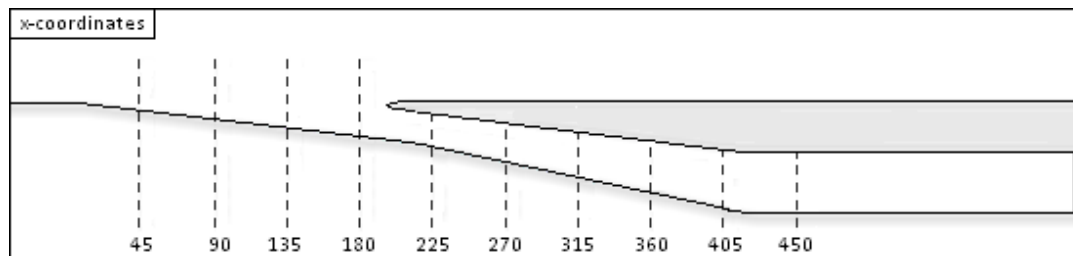


Figure 4.47  
Sideview of the inlet system with x-positions

Figure 4.42 to 4.45 show the start and development of the two wakes at the inlet ramp walls. In conjugation with the streamlines in Figure 4.40, the vortices are seen to be very important to force air flow into the inlet. Figure 4.45 is from x-station 225, where only the inlet diffuser is shown. It should be remarked that the two wakes are still present at that x-station within the diffuser, even if the strength of the vortices is reduced.

Reference [18] remarked that a symmetry of the solution is one of the indications of a good accuracy. This is of course only valid for a computational set-up without symmetry plane.

The results obtained within this investigation showed for all cases a very good symmetry. This is at least one indicator that the flow phenomena are captured by mesh cell size and RANS solver set-up.



## 4.8 Conclusions and Recommendations of Future Work

The objective of this thesis was to investigate the ram pressure efficiency and the drag caused by a NACA inlet with different ramp angles inside a wind tunnel set-up. The model investigated is a smaller version of the inlet used on some of Airbus airliners today. The results obtained within this thesis are therefore of interest to evaluate the performance of these inlets.

It was a difficult task to get the numerical calculations of the wind tunnel boundary condition in combination with the inlet flow settings to work. This numerical set-up consumed a lot of time. Additionally a very high number of RANS solver iterations was needed to get a converged solution for the numerical simulation including the inlet. Nevertheless, the meshing procedure was also a longer than anticipated task. This was mainly due to the difficulty of predicting the outcome of adjusting the parameter settings for surface, prism and tetrahedra mesh contents. Despite the mentioned difficulties, the numerical computations were successfully finalized in the end and the NACA inlet flow phenomena were assessed as originally planned within the scope of this thesis.

The analysis showed that the drag increases with increasing mass flow, and varied depending on the ramp angle used. The differences in ram pressure efficiency for a change of ramp angle or mass flow are, based on the results obtained with in this thesis, seen to be small.

Additionally to the ram pressure efficiency investigation, a detailed analysis of the boundary layer velocity profile was performed at different x-stations on the wind tunnel floor and inside the inlet. The results obtained of the ram pressure efficiency were compared to an estimation method based on experimental data (ESDU) and a previous CFD analysis.

The investigated ramp angle variations showed that the 7 degrees case and its corresponding width/depth ratio of 3.9 seems to be the optimum in view of ram pressure efficiency at the given conditions. In view of drag of the complete inlet system, including the influence on the surrounding surfaces, it was shown to be beneficial to have as low ramp angle as possible for a given mass flow. This recommendation is based on the inlet investigation only. The real situation on an aircraft is expected to be more complex. In an aircraft the heat exchanger and the RAO (Ram Air Outlet) are additionally driving the flow. Both, the heat exchanger pressure loss and the opening angle of the RAO will highly influence the air systems characteristics.

Future work is seen in the complete simulation of a system with an air inlet, heat exchanger and outlet. These simulations can be compared and validated with the outcomes of the wind tunnel test campaign at TWG planned for October 2011.

With these numerical computations of the complete air system, additional valuable results will contribute to the prediction of Star-CCM+ compared to TAU RANS.

Additional effort should be invested into the numerical wind tunnel simulation. It was found out that recently available TAU RANS solver versions did not simulate wind tunnel set-ups as they are described in the solver manual. This part is seen to be repaired and maintained by the TAU developer team.





## References

- [1] Aurelien Rigollet. *CFD computations for RAM air inlets*. Master's thesis, Ecole Nationale Supérieure de Mécanique et d'Aérotechnique, 2009.
- [2] John D. Anderson. *Introduction to Flight*. McGraw-Hill Higher Education, 6th edition, 2008.
- [3] John D. Anderson. *Fundamentals of Aerodynamics*. McGraw-Hill Higher Education, 4th edition, 2006.
- [4] *Getting to grips with aircraft performance*, January 2002. Airbus.
- [5] ESDU. *03006. Subsonic drag and pressure recovery of rectangular planform flush auxiliary inlets with ducts at angles up to 90 degrees*, 2003.
- [6] ESDU. *86002. Drag and pressure recovery characteristics of auxiliary air inlets at subsonic speeds*, 2006.
- [7] John D. Anderson. *Computational Fluid Dynamics*. McGraw-Hill Higher Education, international edition, 1995.
- [8] David C. Wilcox. *Turbulence Modeling for CFD*. DCW Industries, 3rd edition, 2010.
- [9] Jiri Blazek. *Computational Fluid Dynamics: Principles and Applications*. Elsevier, 2006.
- [10] Institute of Aerodynamics and Flow Technology, Braunschweig. *Technical Documentation of the DLR TAU-Code*, 2010. Release 2010.2.0.
- [11] Thomas Gerhold. *TAU Training Document - TAU Overview*, 2007.
- [12] Alvin H. Sacks and John R. Spreiter. *Theoretical investigation of submerged inlets at low speed*. Technical report, National Advisory Committee for Aeronautics, 1951.
- [13] Luis Fernando Figueira da Silva Antonio Batista de Jesus Cesar Celis Perez, Sandro Barros Ferreira and Guilherme Lara Oliveira. *Computational Study of Submerged Air Inlet Performance Improvement Using Vortex Generators*. *Journal of Aircraft*, 44(5), 2007.
- [14] Emmet A. Mossman and Lauros M. Randall. *An experimental investigation of the design variables of NACA submerged duct entrances*. Technical report, National Advisory Committee for Aeronautics, 1948.
- [15] Lauros M. Randall Charles W. Frick, Wallace F. Davis and Emmet A. Mossman. *An experimental investigation of NACA submerged duct entrances*. Technical report, National Advisory Committee for Aeronautics, 1945.
- [16] John Seddon and E.L. Goldsmith. *Intake Aerodynamics*. Blackwell Publishing Limited, 1985.
- [17] Dr. Martin Schmid. *ECOcents Cooling Channel: CFD Analysis TWG environment*. Airbus, 2010. Powerpoint presentation.
- [18] Dr. Christian Bartels. Senior Expert in Aircraft System Aerodynamics at Airbus. Verbal communications.

- 
- [19] A. Grimminger. *Current Practice for Meshing of High Lift Configurations with Centaur*. Technical report, Airbus, 2009.
- [20] John Dietrich. *TAU Code Validation According to the Boundary Layer Flowfield*. Technical report, Airbus, 2007.
- [21] Markus Widhalm. *Windtunnel Boundary Conditions*. German Aerospace Center, 2011. Powerpoint presentation.
- [22] R. P. Dwight. *Engine Inflow Boundary Conditions for Specification of Mass-Flow*. Technical report, DLR, 2005.
- [23] Anica Bäre. *CFD Investigation on the Influence of Wind Tunnel Enclosure and Model Mounting on the Characteristics of the Tails of a Transport Aircraft Configuration*. Technical report, Airbus, 2010.
- [24] Dr. Bruno Stefes. Skill Group Leader of the Fuselage Air Systems Group at Airbus. Verbal communications.
- [25] Thomas Stevens. *CFD results comparison of System operating point at Cruise conditions*. Airbus, 2011. Powerpoint presentation.
- [26] Udo Krause. Research Engineer in Aircraft Aerodynamic Design at Airbus. Verbal communications.
- [27] *TAU-Code User Guide*, 2010. Release 2010.2.0-p1.
- [28] Holger Dettmar. *Hybrid-CFD Training, CAD and Mesh generation*. Airbus, 2009. Powerpoint presentation.
- [29] Dietrich John. *A Program to Evaluate the Boundary Layer Flow Field from Navier-Stokes Results in Unstructured Grids*. Airbus, 2004.
- [30] DNW german-dutch wind tunnels: TWG. <http://www.dnw.aero/windtunnels.aspx?id=304&menuid=34&subid=304>, May 2011.

## A APPENDIX

### A.1 Computational Models and Tools

#### Grid Generation

The purpose of grid generation is to attain a structured and/or unstructured grid which defines the geometry of a two or three-dimensional model and the surrounding flow field. The generated grid is referred to as a mesh and defines the calculation points used by a flow solver. A higher number of elements are required in regions where the flow is expected to undergo dramatic changes in terms of e.g., temperature, pressure and velocity.

##### A.1.1 CENTAUR

CENTAUR is the program which has been used to generate the calculation grid in this thesis. This mesh generation program can produce a hybrid mesh composed of prismatic, hexahedral, pyramidal and/or tetrahedral elements.

When the user has made a CAD model and wishes to proceed and generate a computational grid, the first thing to be done is to export this model in a format which CENTAUR can read. When this file has been read into CENTAUR the model needs to be cleaned.

What does clean mean in this context? When the IGES file supported by CENTAUR has been exported from the CAD program, the quality of the model often need to be improved in some regions. The original CAD geometry is not water-tight. This has to be prepared within the CAD process.

CENTAUR has a diagnostic procedure which detects problematic panels and lines. Problematic lines are typically lines with high curvature which have been split into smaller lines that lie on top of each other. These lines have to be merged or deleted to obtain a valid geometry. Some of these issues are taken care of automatically by CENTAUR while others can be fixed manually by applying available tools.

When the geometry has been defined correctly, the next step is to configure the general settings employed by CENTAUR during the mesh generation process. Settings defining the properties of the surface elements, prismatic elements and tetrahedral elements are governed by parameters found in separate files adherent to each project. The values of some of these parameters can be approximated with the help of several Airbus-internal softwares. Others have to be found by an iterative process where the results of different configurations are analysed.

#### Mesh Generation

The meshing strategy which is employed by CENTAUR allows the user to define what type of mesh to be generated: a hybrid mesh or a complete unstructured mesh for e.g., Euler equation computations (inviscid flow). The hybrid mesh is appropriate to use if the computational grid generated will be processed by a RANS solver such as the RANS routine within TAU. A hybrid mesh consist of both structured and unstructured elements. Structured elements are generated in physical interesting regions, e.g., the boundary layer while unstructured elements are used to quickly and with minimum effort fill the rest of the computational space.

The panels which make up the model in CENTAUR must be assigned to groups which in turn have to be assigned a boundary condition later used by the flow solver. The boundary conditions used in this thesis are *viscid wall*, *inviscid wall*, *inlet*, *outlet* and *interface*. The approach of using a complete unstructured mesh and solve this with Euler equations would require all surfaces to be set to *inviscid wall* and the element type for all these surfaces set to *tetrahedra*.

The following steps are performed to create a mesh which can be successfully used for calculations:

- CAD Preparation
- Generation of a surface mesh
- Generation of a prismatic mesh
- Generation of a complete mesh, including tetrahedral mesh elements
- Analysis of generated mesh.
- Iterative process: Change appropriate parameters and generate a new mesh until satisfied with the result.

### Input/Output Files

The mesh generator uses the following input files:

- project.sin for global parameters controlling the surface mesh generation process
- project.pin for global parameters controlling the prism generation process
- project.tin for global parameters controlling the tetrahedral generation process
- project.lin for source settings to locally specify any or all of the above parameters in a selected geometric area or field volume

The output files are:

- project.fvs containing the surface mesh
- project.fvp containing the surface mesh and the prismatic cells
- project.hyb containing the complete mesh.

The complete mesh consists of the surface mesh, the prismatic mesh and the tetrahedral elements. This file can be used for inspection, while a \*.grid file containing all information about the computational mesh is used for actual calculations by a flow solver.

### Surface Mesh Generation

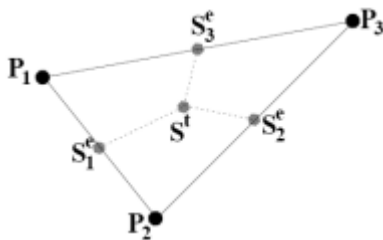


Figure A.1.1

Control volume borders on a triangle  
Figure from Reference [10]

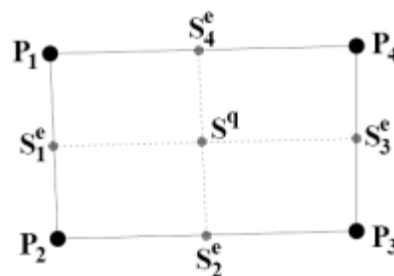


Figure A.1.2

Control volume borders on a quadrilateral  
Figure from Reference [10]

The surface mesh consists of triangles and quadrilateral elements which allow for the very high flexibility needed for a good representation of complex geometries. Elements with small angles or with great skewness should be avoided in order to ensure a valid grid and faster convergence of the solution in the flow solver [27]. *Stretching ratio* and *scaling parameter* are two examples of settings available in the surface generation input file for the mesh generation process and these often need to be adapted for a specific case, determining the rate of change of element size from one element to its neighbours and the average size of the grid elements respectively.

### Prismatic Mesh Generation

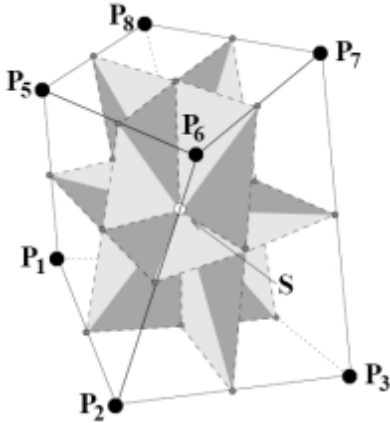


Figure A.1.3

Control volume borders in a hexahedron

Figure from Reference [10]

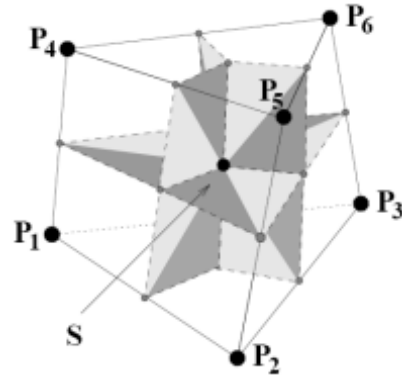


Figure A.1.4

Control volume borders in a prism

Figure from Reference [10]

A prismatic mesh can be generated when the surface mesh generation has been successful. The prismatic mesh consist of hexahedral and prismatic elements created perpendicular to the surface. They extend a set number of layers specified by the user in the separate input file and gradually increase in size further away from the surface. The first prismatic layer should lie within the viscous sublayer of the boundary layer [28]. The viscous sublayer which exist in turbulent flow is a region very close to the surface where the flow is laminar. This region is typically around 1% of the total boundary layer thickness. A calculation point should be within this region to ensure sufficient resolution of the boundary layer characteristics such as the velocity profile and momentum thickness. To ensure sufficient resolution of the turbulent boundary layer, a non-dimensional distance from a surface  $y^+$  is defined as

$$y^+ = \frac{y \sqrt{\frac{\tau_w}{\rho}}}{\nu} \quad (18)$$

where  $\tau_w$  is the shear stress at the wall,  $\rho$  the density of the air,  $y$  the distance from the wall, and  $\nu$  the kinematic viscosity.

The value of the first off-wall node  $y^+(1)$  in the prismatic grid should be within the limits of  $0 \leq y^+(1) \leq y_{max}^+$  where  $y_{max}^+$  depends on the Reynolds number and should be at most the thickness of the boundary layer multiplied by 0.05. However, a good estimated target  $y^+(1)$  for a Low-Reynolds boundary condition is 1 [27]. The value of  $y^+(1)$  determines how accurately the grid captures the viscous effects of the flow.

### Tetrahedral Mesh Generation

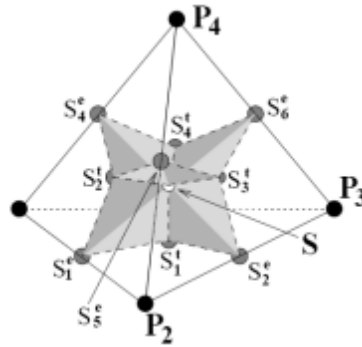


Figure A.1.5

Control volume borders in a tetrahedron. Figure from Reference [10]

When the surface- and prismatic mesh has been generated the remaining domain is filled with tetrahedral elements. This is because of how quickly and easily these elements can fill a large volume. Similarly to how the prismatic mesh elements gradually increase in size further from the surface, so does the tetrahedral elements further away from the prismatic layers.

### Pyramids

A sixth type of geometric figure which is generated in CENTAUR is a pyramid. These elements are useful to bridge between the different element types such as from prisms to tetrahedrals.

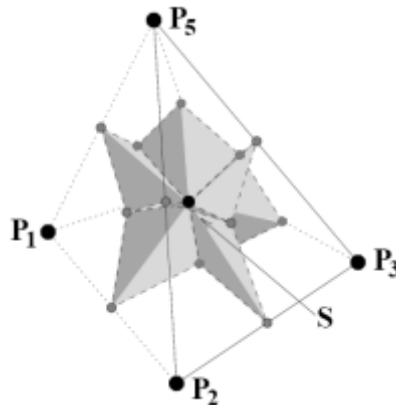


Figure A.1.6

Control volume borders in a pyramid. Figure from Reference [10]

### Sources

An important feature which is employed in CENTAUR and which is a fundamental tool to attain good accuracy are *sources*. Implementing a source allows for the user to directly specify the distance between calculation points, the number of prismatic layers and the stretching ratio in a specified area or volume. The surface- and prismatic mesh often needs to be refined where the geometry undergoes sudden changes such as high curvature areas or transitions from one panel to another.

There are two types of sources, *Geometrical Sources* and *CAD Sources*. Geometrical sources are defined as a 3-dimensional object (e.g., a sphere, cylinder or rectangular box) inside which local settings are defined while CAD sources are linked to a panel or line in the existing geometry.

### A.1.2 TAU

The TAU code is a Reynolds-Averaged Navier Stokes (RANS) solver developed by the German Aerospace Center (DLR). TAU can solve the complete system of RANS-equations or just the Euler equations depending on settings. The TAU code has been used in the aerospace branch for the past 25 years and has been validated by various DLR and Airbus funded projects. One such investigation of the accuracy of the TAU code was carried out in Reference [20]. It involved two wind tunnel test campaigns for low and high Reynolds numbers and one flight test campaign at different Reynolds number and different Mach numbers. Comparison of the data gathered to TAU calculations showed an overall good consistency and the code was judged to be reliable.

The software consists of a number of modules which are parallelized and can be distributed over several processors to work on the same grid partitions. The TAU Training Document (Reference [11]) states that in order to achieve high efficiency when using multiple processors, the number of grid points which makes up the mesh we want to investigate divided by the number of processors should be greater than or equal to 100 000. Additional processors will only reduce the calculation time slightly.

When working with CFD this will also depend on the computational environment at, for example, the work place. Sometimes it might be more efficient to reduce the number of CPUs to a number lower than the optimum. This will depend how long the waiting time is for a set number of CPUs. A job might finish faster if it starts right away with 64 processors than if it has to wait to start with 254 processors.

The main modules of TAU are

- Grid Partitioning and Re-partitioning
- Pre-processing
- Flow Solver
- Grid Adaption
- Grid Deformation

### A.1.3 Tau.BL

The program Tau.BL [29] was developed to extract the Navier-Stokes results calculated by TAU in the boundary layer. The results extracted are used to calculate boundary layer parameters such as the boundary layer thickness and the momentum thickness. The program uses the data available in TAU, thus reducing errors occurring on account of the user by requiring fewer inputs. Tau.BL has been validated at several Airbus projects.

Tau.BL results can be exported and viewed in a CFD visualization program such as Tecplot 360. Another possibility is to input specific coordinates and obtain information on the boundary layer at only these points, requiring less computational time.

While the program has difficulties asserting the boundary layer profile at stagnation points, conjunction areas and the trailing edge of wings, it is still a very reliable, fast and accurate program for the rest of a configuration [29].

#### A.1.4 CATIA

CATIA stands for Computer Aided Three-dimensional Interactive Application and is a Computational Aided Design (CAD) software. CATIA is a powerful tool for designing three-dimensional objects with very high accuracy. The first version of CATIA was released in 1981 and is today one of the most commonly used CAD softwares. It is used by a wide range of industries; the aerospace, automobile and shipbuilding industry among others.

CATIA offers a number of different design modes which have been tailored for a specific purpose, e.g., *Part Design*, *Composite Design*, *Weld Design*, *Sheet Metal Design* and *Assembly Design*. When carrying out this thesis project, mainly the *Generative Shape Design* mode was used in which it is possible to modify and create surfaces.

#### A.1.5 Tecplot 360

Tecplot 360 is a numerical simulation and CFD visualisation program. What this means is that the program can visualise the solution obtained by a flow solver of the flow field variables on a 2D or 3D representation of the model. Information on any of the calculated flow variables can be attained at any location where a calculation point was generated in the mesh. An example of how tecplot 360 can visualise the calculated flow field variables is shown in Figure A.1.7 below.

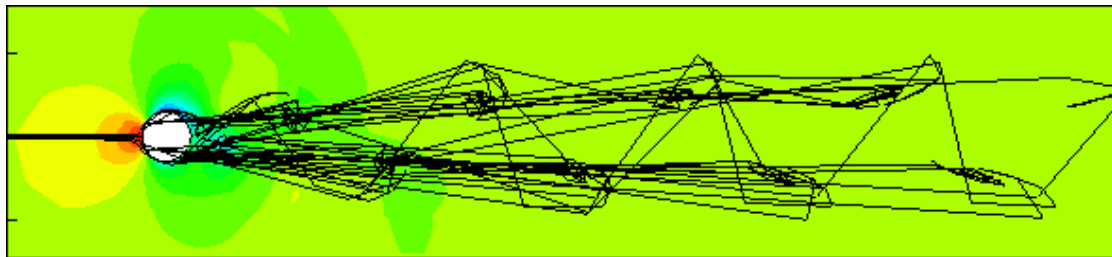


Figure A.1.7

Streamlines and the pressure distribution is visualised on a 2D view of a cylinder

#### A.1.6 RAMAIR

This program was developed at Airbus Bremen in 2007 for air inlet properties estimation and is based on ESDU paper 86002 (Reference [6]). It is possible to specify either a target mass flow to find out the appropriate inlet area at a set width/depth ratio, or to specify the inlet area to find out the mass flow. It is also possible to investigate different types of inlets: the NACA curved-diverged inlet, a flushed rectangular inlet and a scoop inlet with different inlet geometries (circular, semi-circular and rectangular).

One of the most relevant outputs of RAMAIR is the aerodynamic drag caused by the inlet. The aerodynamic drag should be as low as possible while the needed air mass flow is assured.

The output values obtained from the use of RAMAIR depend on more than just the geometrical shape of the inlet. Examples of other input settings greatly affecting the calculated values are the boundary layer thickness, the Mach number and ambient conditions such as density and temperature at a selected altitude.



## A.2 Figures

### A.2.1 Introduction

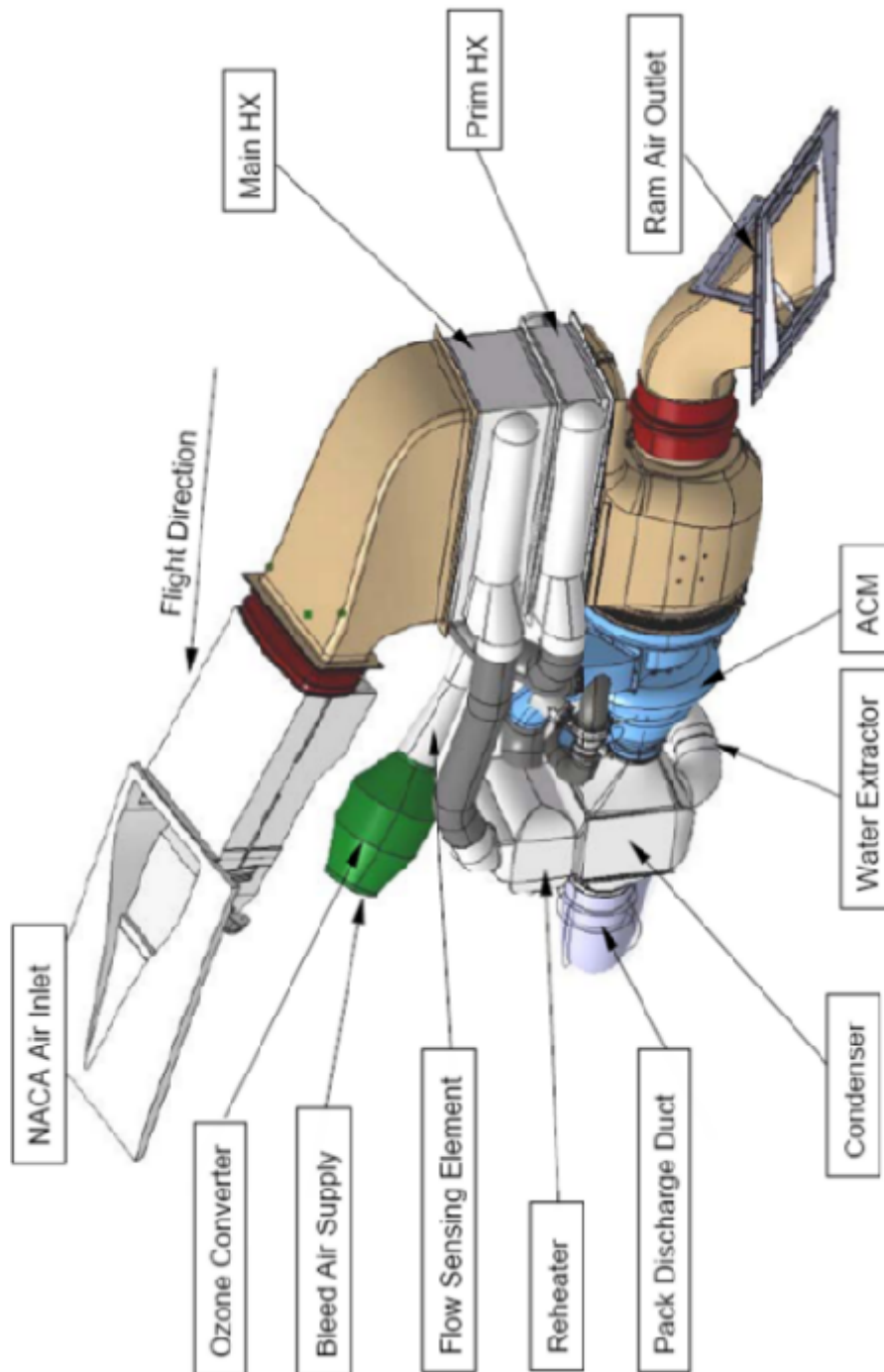


Figure A.2.1

Example of an air cooling and supply system. Image courtesy of Airbus

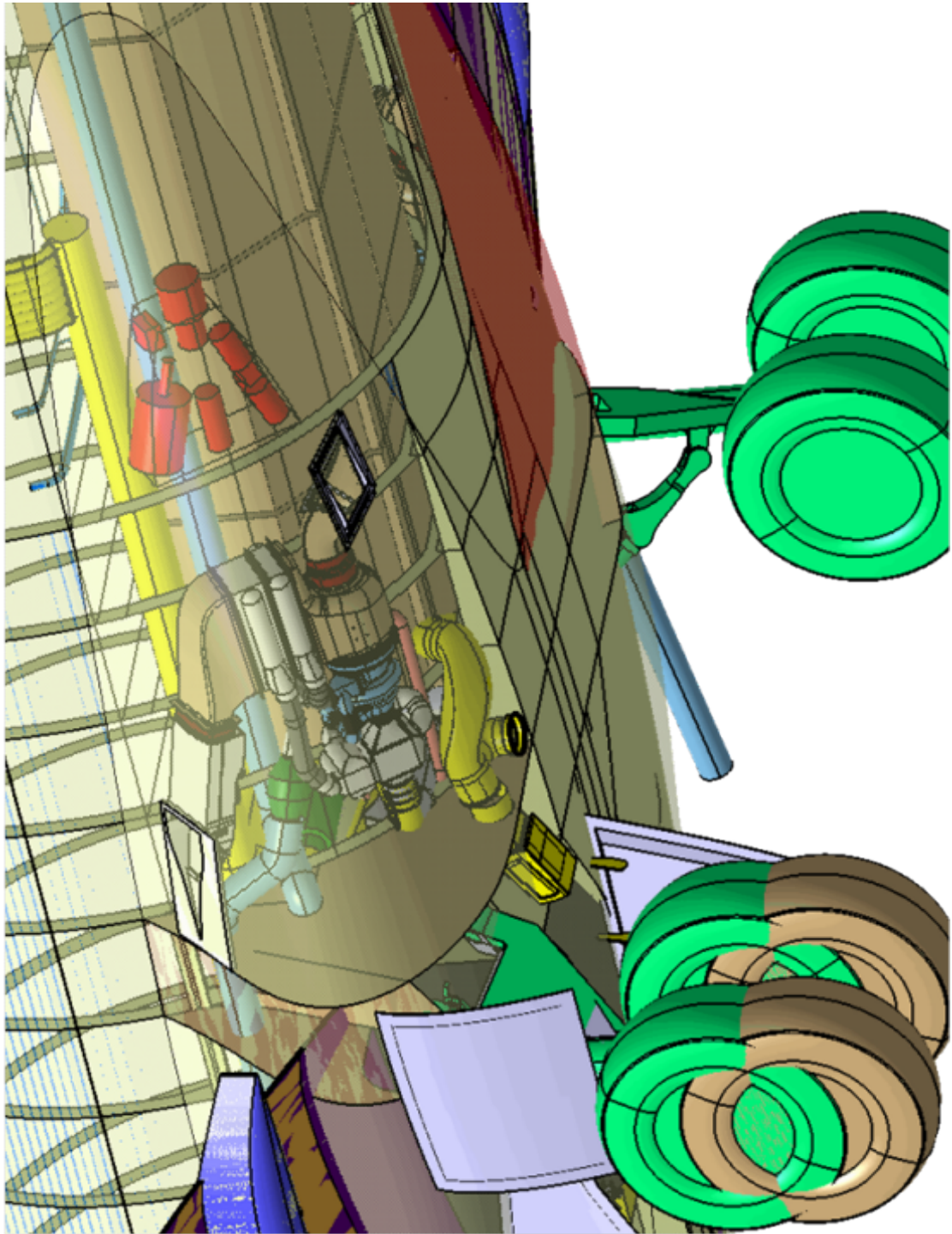


Figure A.2.2

Air cooling and supply system inside the belly fairing of an airplane. Image courtesy of Airbus

A.2.2 Measurements

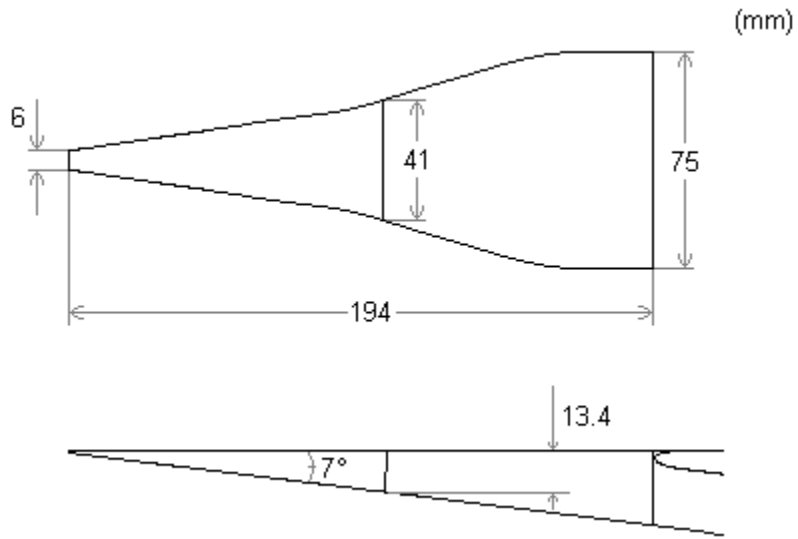


Figure A.2.3  
Measurements of the NACA submerged inlet investigated in this report

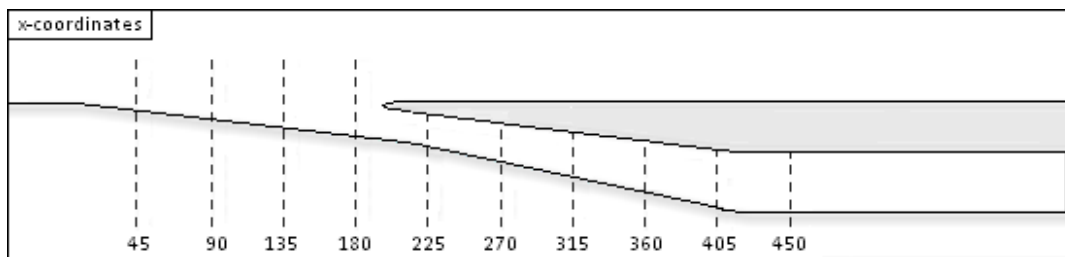


Figure A.2.4  
X-coordinates at different locations of the inlet

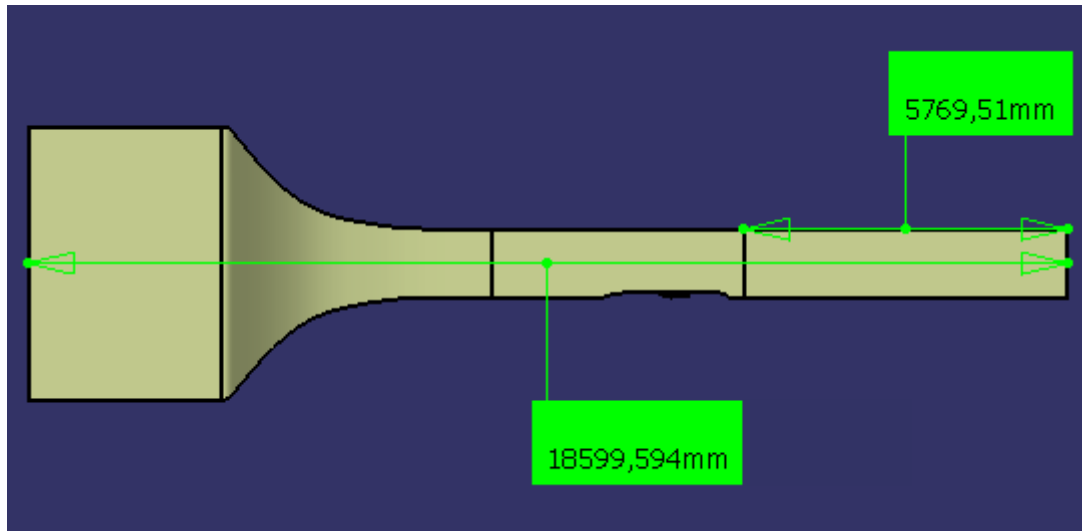


Figure A.2.5  
Side view of the wind tunnel geometry with measurements in millimeters

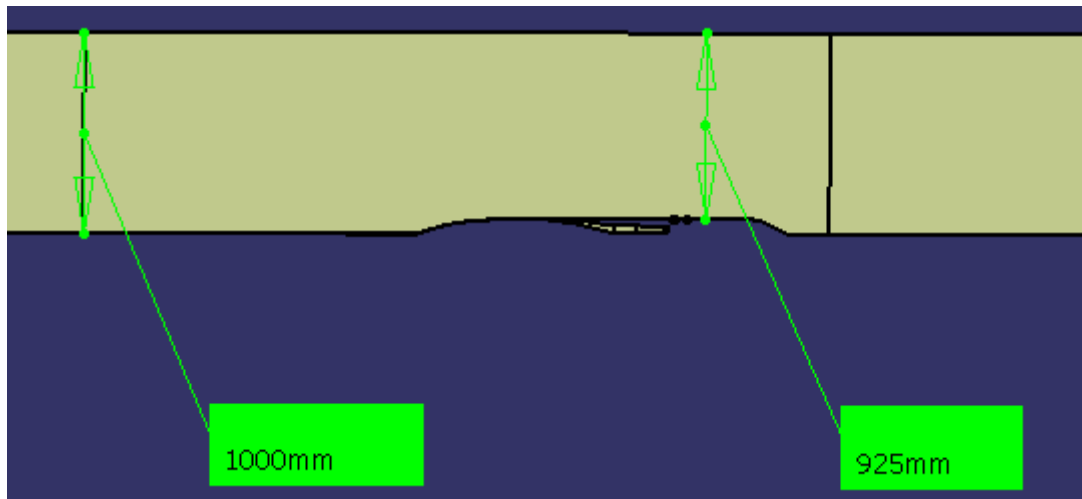


Figure A.2.6  
Side view of the wind tunnel test section with measurements in millimeters

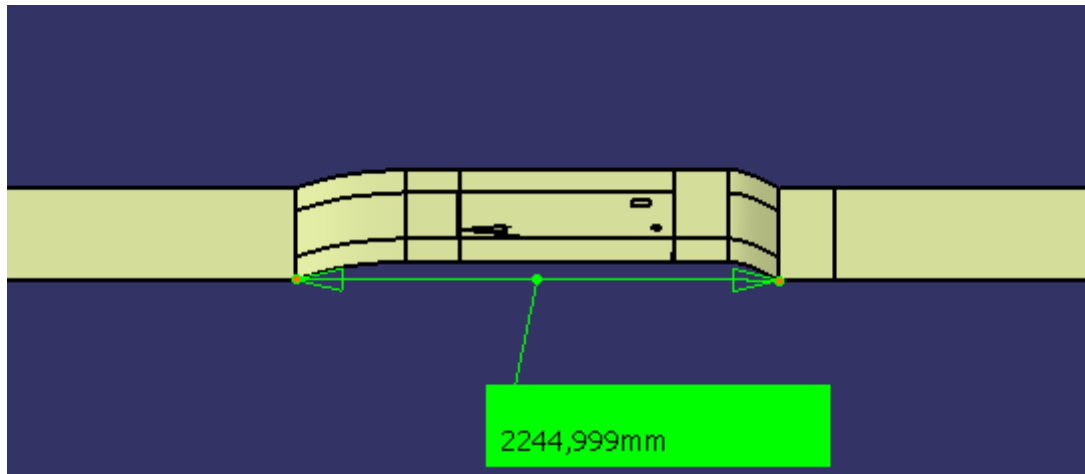


Figure A.2.7  
Side view of the wind tunnel test section with measurements in millimeters

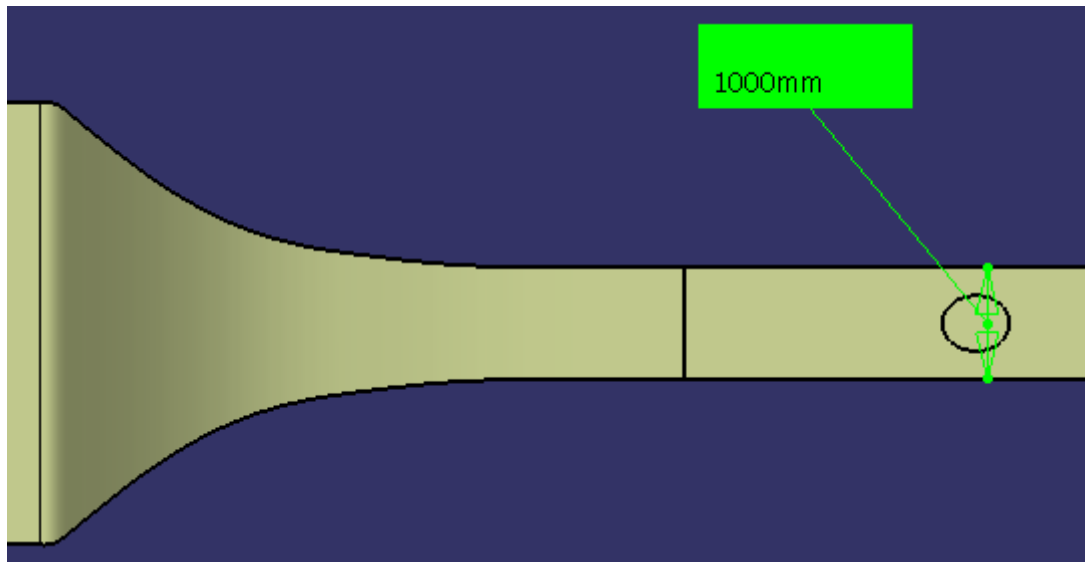


Figure A.2.8  
Top view of the wind tunnel test section with measurements in millimeters

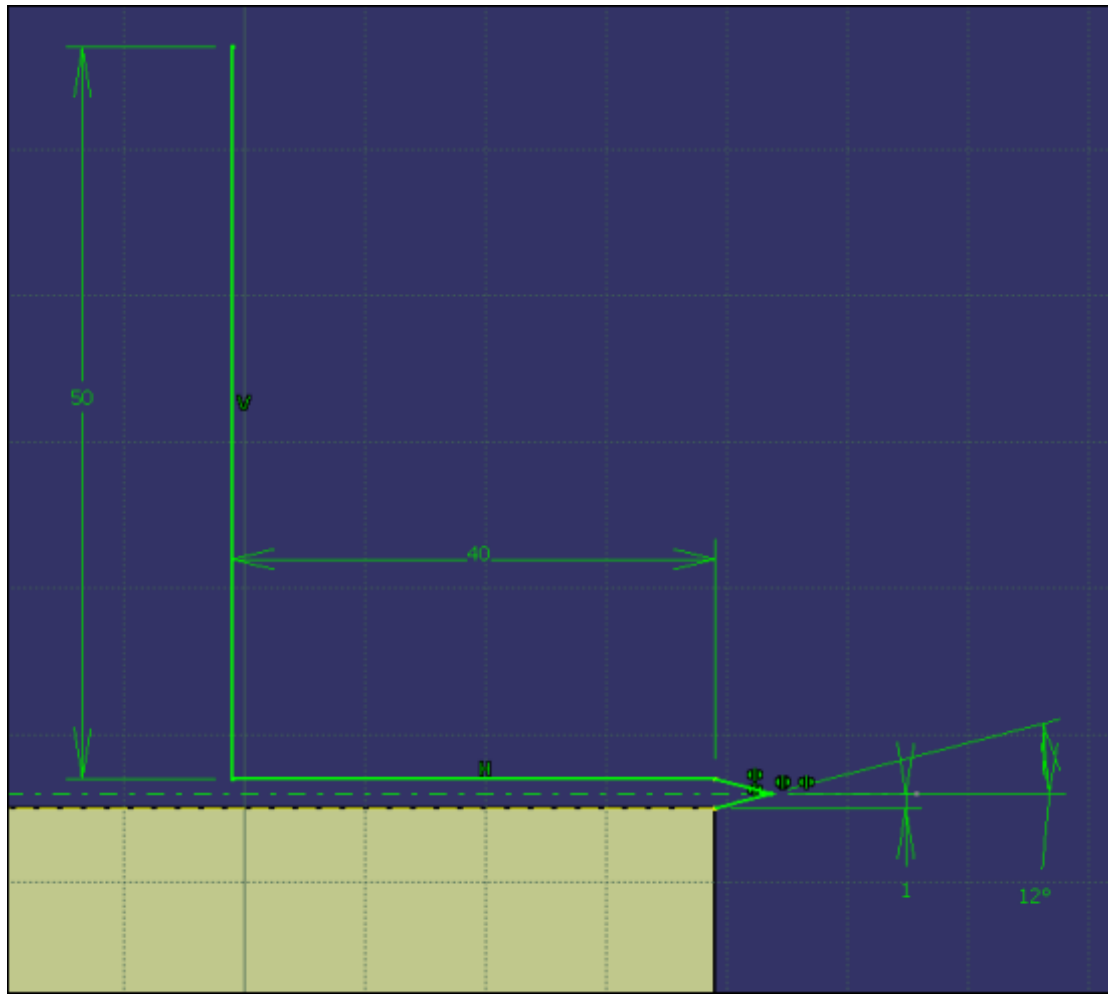


Figure A.2.9  
Measurements in millimeters of the additional inlet geometry which was later removed

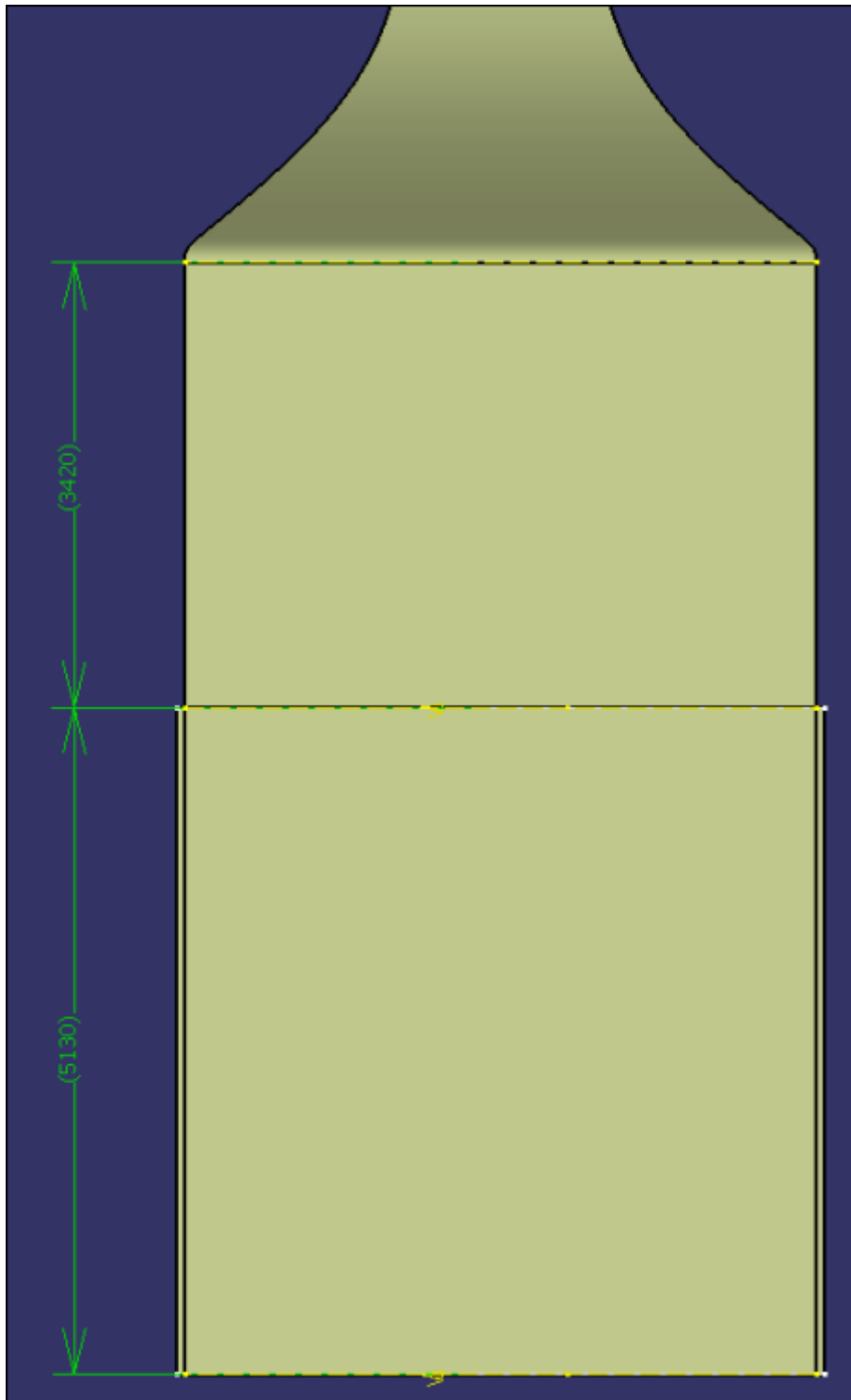


Figure A.2.10

Measurements in millimeters of the original and additional inlet geometry which was later removed

A.2.3 Geometry Preparation

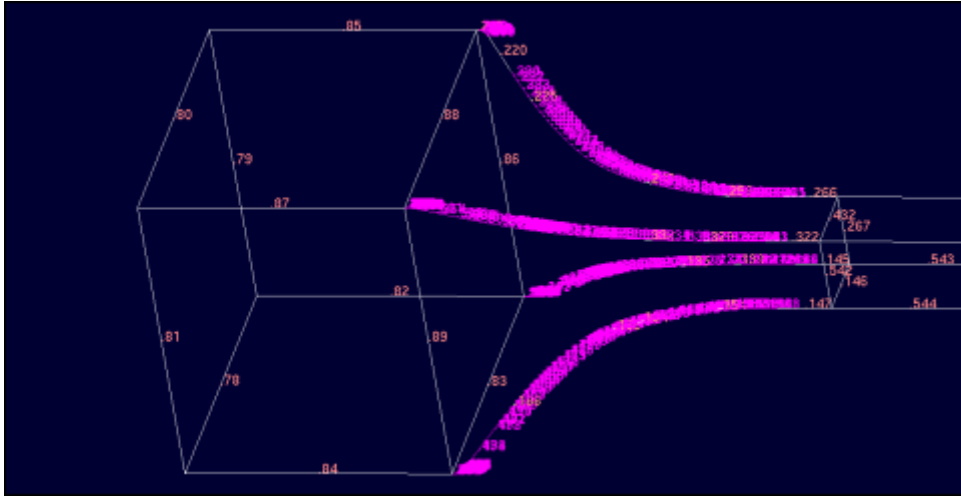


Figure A.2.11  
Part of the wind tunnel geometry prior to CAD Cleaning

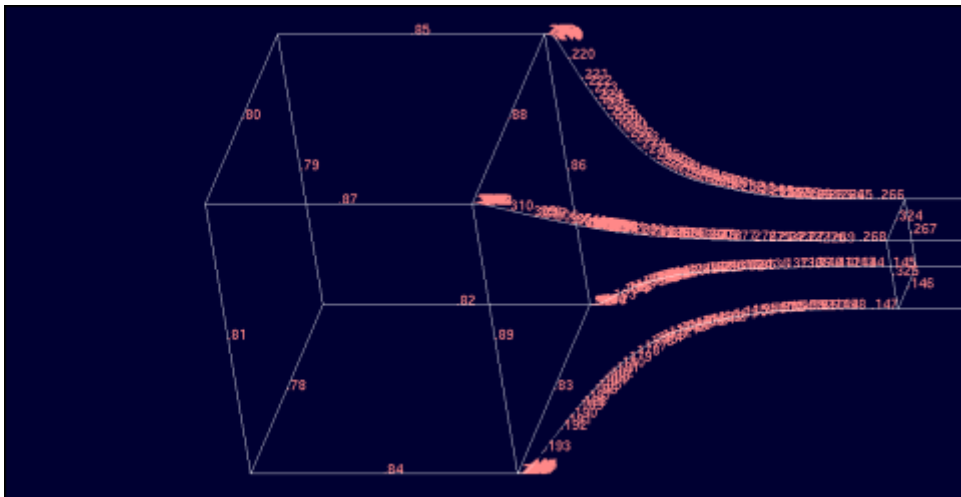


Figure A.2.12  
Part of the wind tunnel geometry after CAD Cleaning had been performed



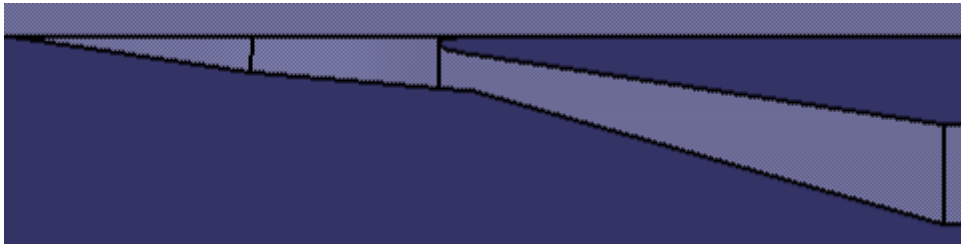


Figure A.2.13  
The air inlet with a ramp angle of 4 degrees as seen in CATIA

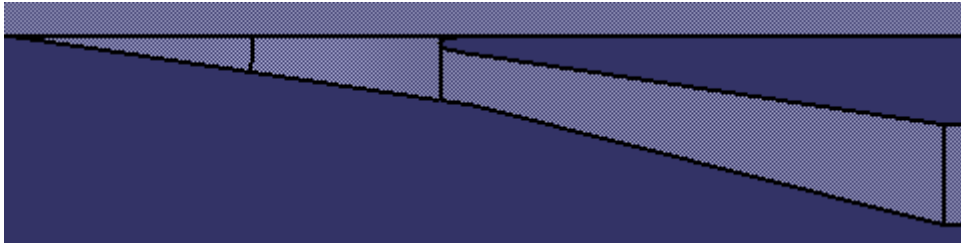


Figure A.2.14  
The air inlet with a ramp angle of 7 degrees as seen in CATIA

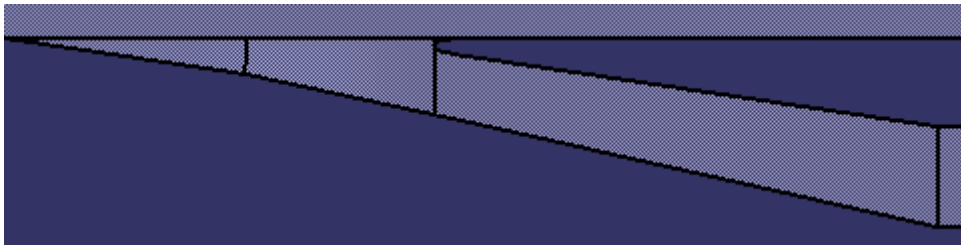


Figure A.2.15  
The air inlet with a ramp angle of 10 degrees as seen in CATIA

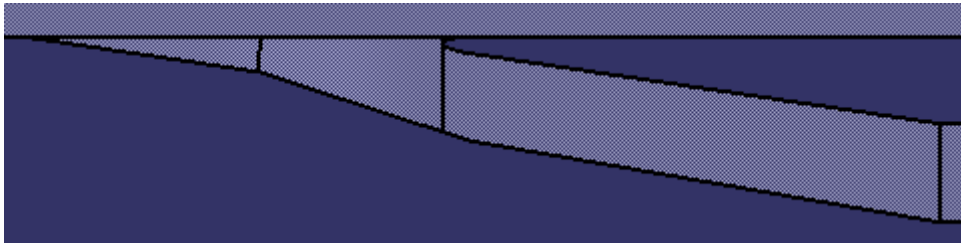


Figure A.2.16  
The air inlet with a ramp angle of 15 degrees as seen in CATIA

## A.2.4 Mesh Generation

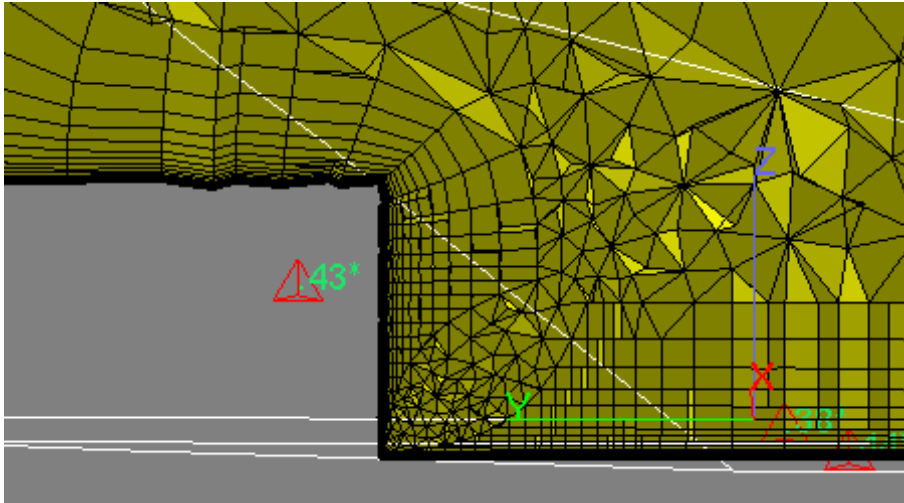


Figure A.2.17

The prismatic layers getting chopped down in the vicinity of the corners of the duct at x-position 45. 7 degrees ramp angle.

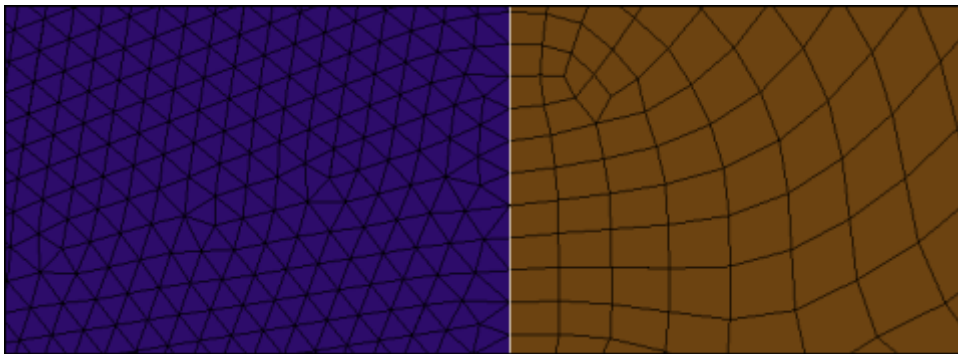


Figure A.2.18

Transition from triangular to hexahedral elements after the bend of the duct

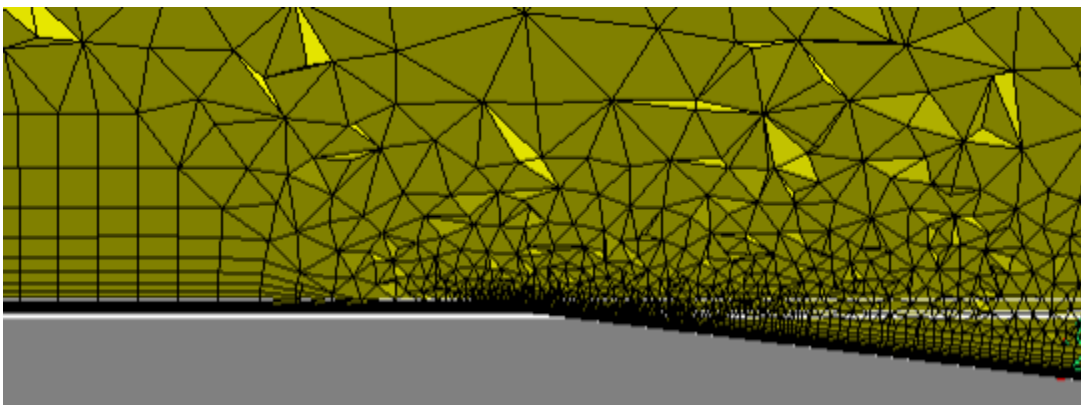


Figure A.2.19

The Prismatic layers prior to the inlet. 7 degrees ramp angle.

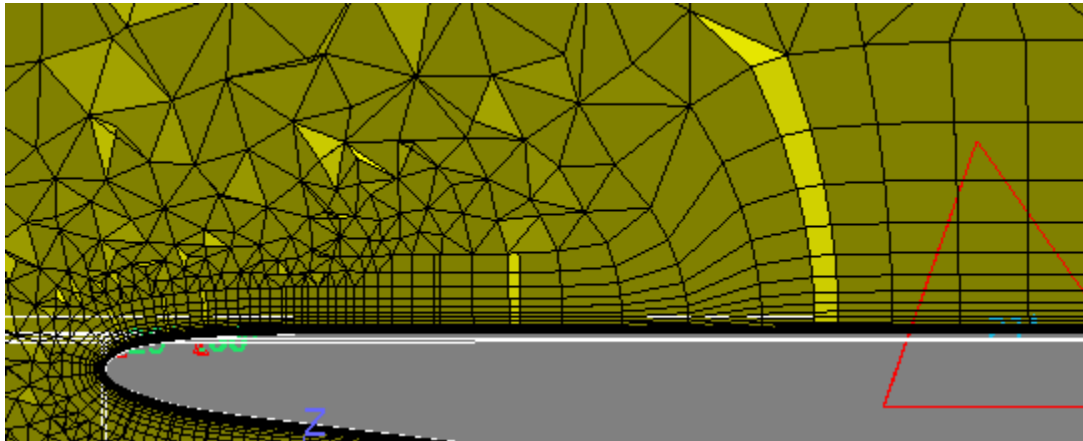


Figure A.2.20  
The prismatic layers aft of the lip of the inlet

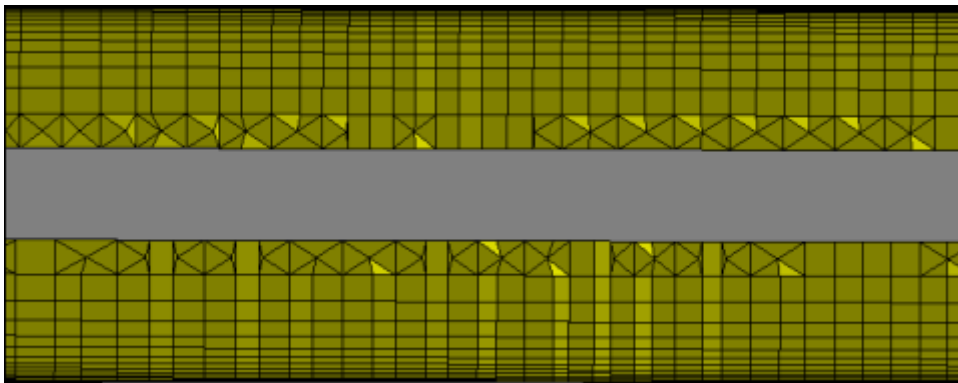


Figure A.2.21  
The prismatic layers in the extension with inviscid walls prior to the outlet  
Tetrahedras in the middle region are not shown

A.2.5 Post Processing

Vorticity plots for an inlet with the variable inlet ramp angle set to 4 degrees

Mass flow: 0.15 kg/s

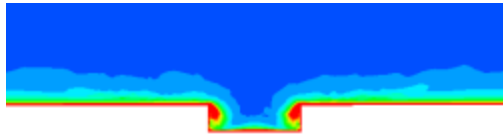


Figure A.2.22  
X-position: 45

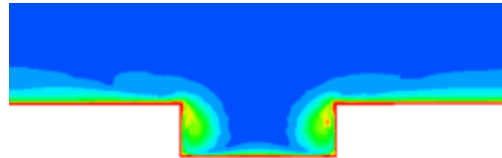


Figure A.2.23  
X-position: 90

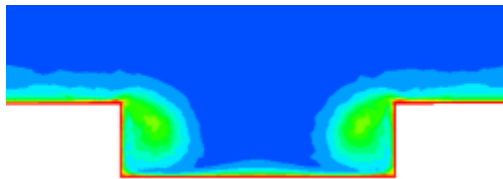


Figure A.2.24  
X-position: 135

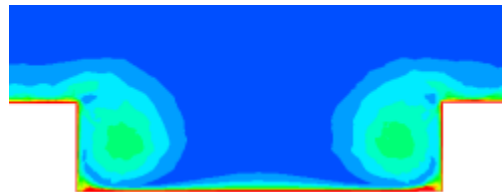


Figure A.2.25  
X-position: 180



Figure A.2.26  
X-position: 225

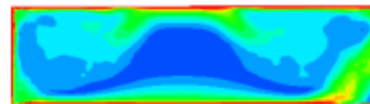


Figure A.2.27  
X-position: 270

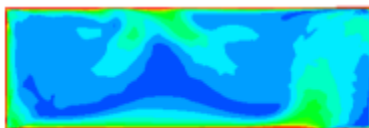


Figure A.2.28  
X-position: 315

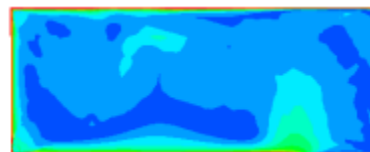


Figure A.2.29  
X-position: 360

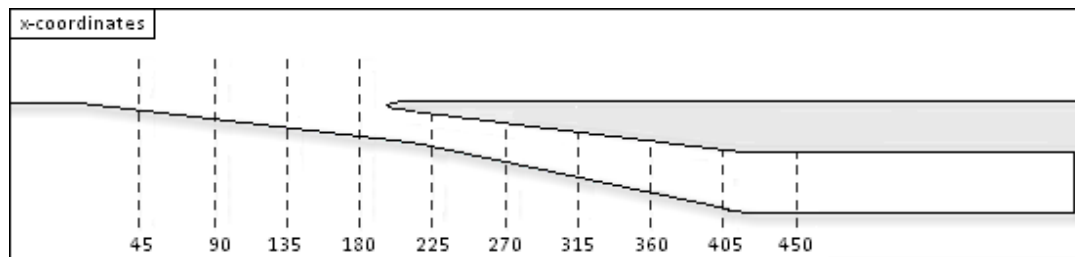


Figure A.2.30  
Sideview of the inlet system with x-positions

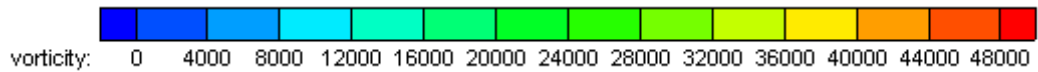


Figure A.2.31  
Inlet vorticity gradient

Vorticity plots for an inlet with the variable inlet ramp angle set to 7 degrees  
 Mass flow: 0.20 kg/s

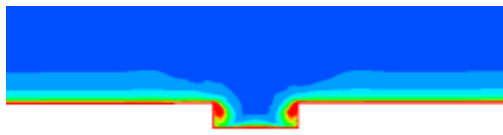


Figure A.2.32  
 X-position: 45

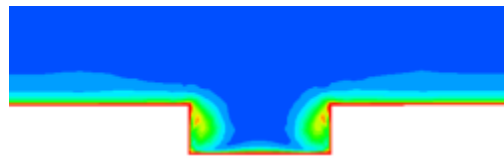


Figure A.2.33  
 X-position: 90

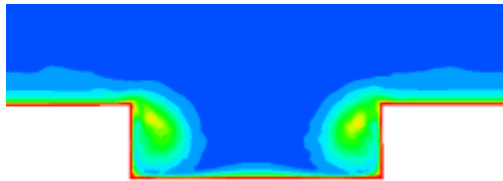


Figure A.2.34  
 X-position: 135

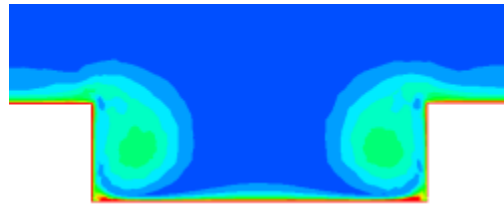


Figure A.2.35  
 X-position: 180



Figure A.2.36  
 X-position: 225

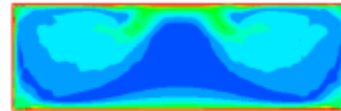


Figure A.2.37  
 X-position: 270

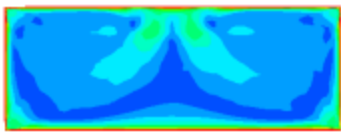


Figure A.2.38  
 X-position: 315

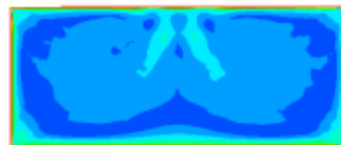


Figure A.2.39  
 X-position: 360

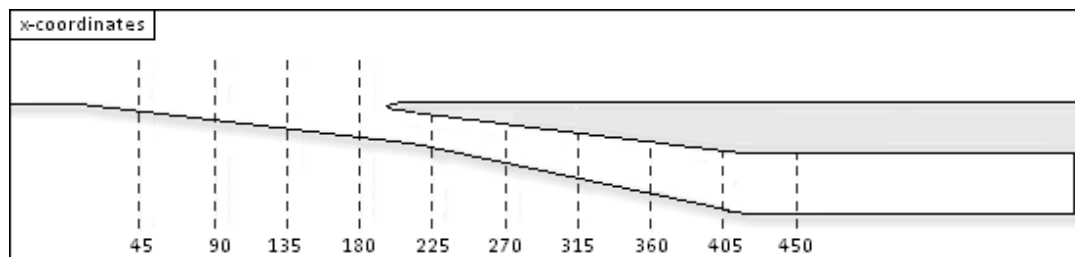


Figure A.2.30  
 Sideview of the inlet system with x-positions

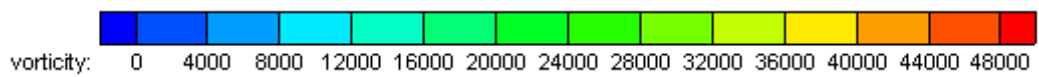


Figure A.2.31  
 Inlet vorticity gradient

Vorticity plots for an inlet with the variable inlet ramp angle set to 10 degrees  
 Mass flow: 0.25 kg/s

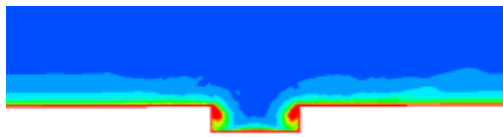


Figure A.2.40  
 X-position: 45

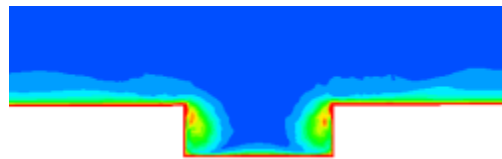


Figure A.2.41  
 X-position: 90

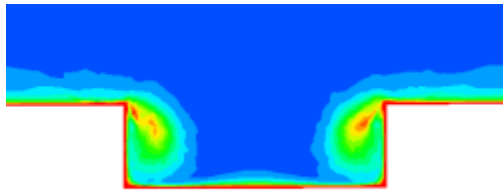


Figure A.2.42  
 X-position: 135

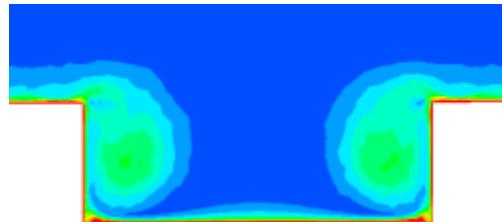


Figure A.2.43  
 X-position: 180

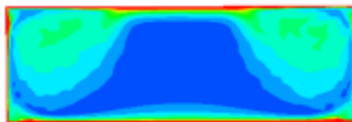


Figure A.2.44  
 X-position: 225

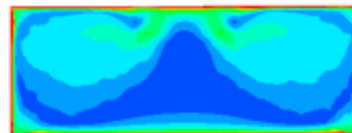


Figure A.2.45  
 X-position: 270

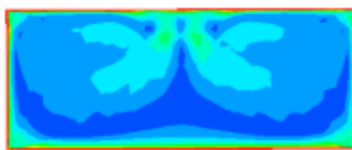


Figure A.2.46  
 X-position: 315



Figure A.2.47  
 X-position: 360

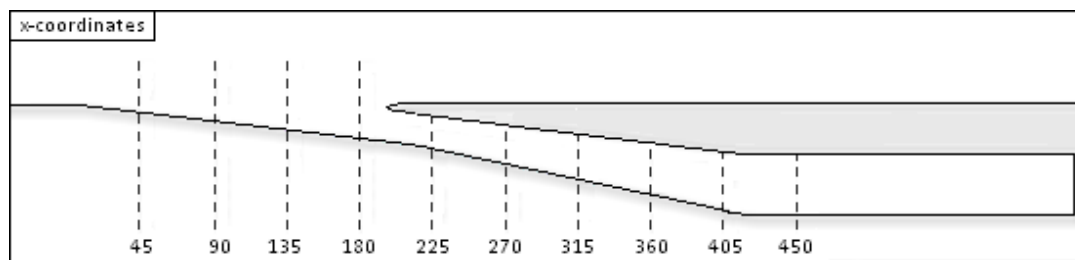


Figure A.2.30  
 Sideview of the inlet system with x-positions

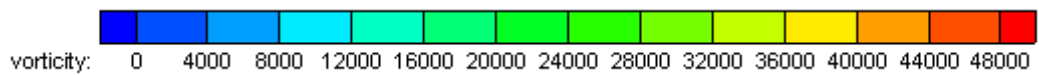


Figure A.2.31  
 Inlet vorticity gradient

Vorticity plots for an inlet with the variable inlet ramp angle set to 15 degrees  
 Mass flow: 0.30 kg/s

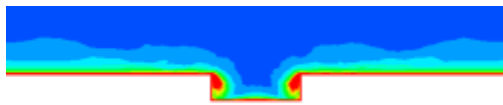


Figure A.2.48  
 X-position: 45

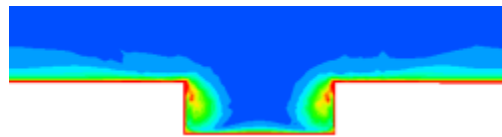


Figure A.2.49  
 X-position: 90

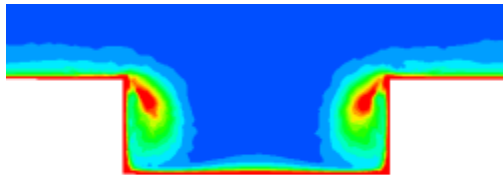


Figure A.2.50  
 X-position: 135

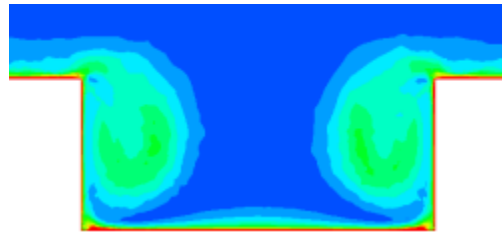


Figure A.2.51  
 X-position: 180

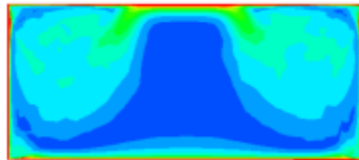


Figure A.2.52  
 X-position: 225

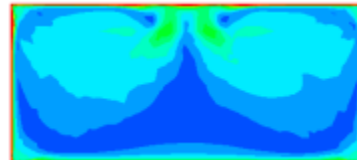


Figure A.2.53  
 X-position: 270

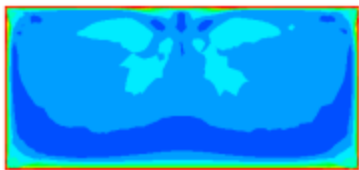


Figure A.2.54  
 X-position: 315

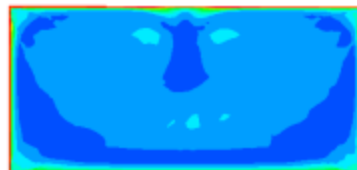


Figure A.2.55  
 X-position: 360

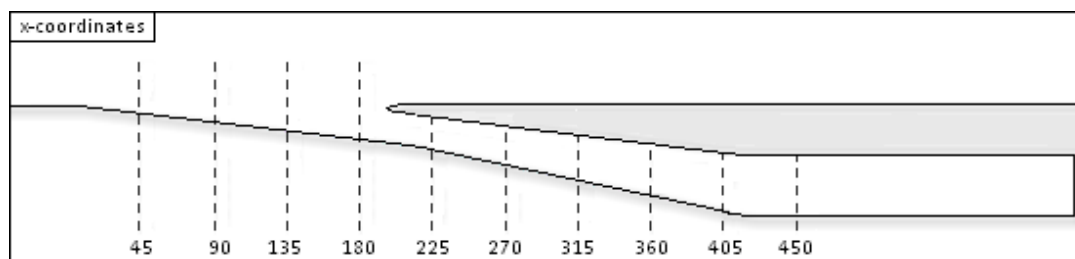


Figure A.2.30

Sideview of the inlet system with x-positions

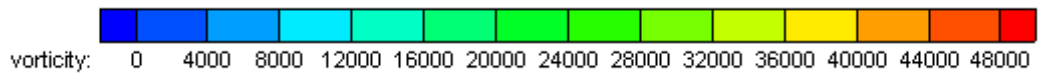


Figure A.2.31

Inlet vorticity gradient

Mach number plots for an inlet with the variable inlet ramp angle set to 4 degrees  
 Mass flow: 0.20 kg/s



Figure A.2.56  
 X-position: 45

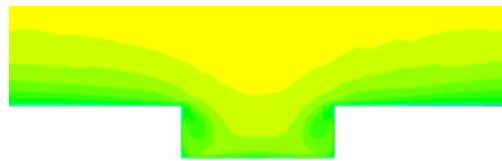


Figure A.2.57  
 X-position: 90

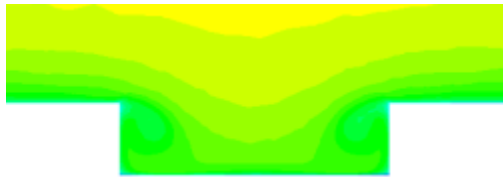


Figure A.2.58  
 X-position: 135

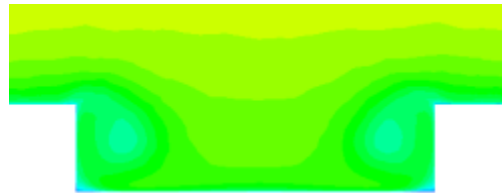


Figure A.2.59  
 X-position: 180



Figure A.2.60  
 X-position: 225

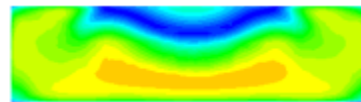


Figure A.2.61  
 X-position: 270

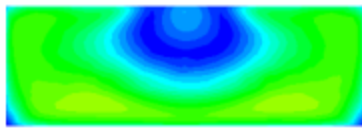


Figure A.2.62  
 X-position: 315

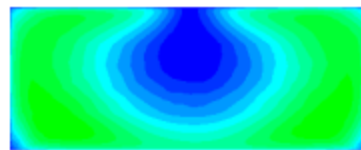


Figure A.2.63  
 X-position: 360

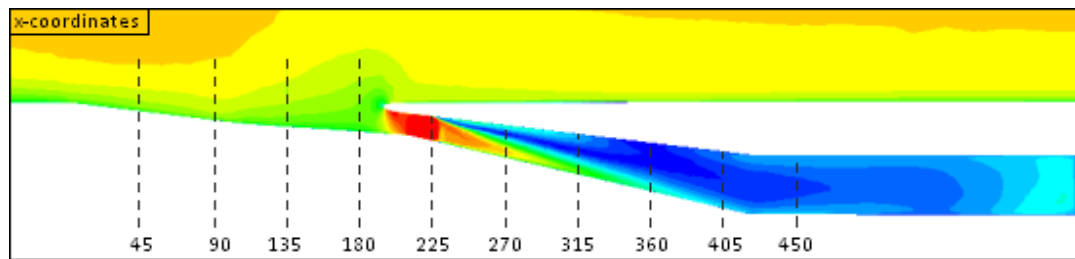


Figure A.2.64  
 Sideview of the inlet system with Mach number and x-positions

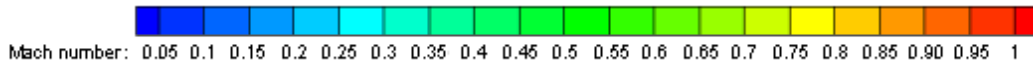


Figure A.2.65  
 Inlet Mach number gradient



Static pressure plots for an inlet with the variable inlet ramp angle set to 4 degrees  
 Mass flow: 0.20 kg/s



Figure A.2.66  
 X-position: 45



Figure A.2.67  
 X-position: 90



Figure A.2.68  
 X-position: 135



Figure A.2.69  
 X-position: 180



Figure A.2.70  
 X-position: 225



Figure A.2.71  
 X-position: 270



Figure A.2.72  
 X-position: 315

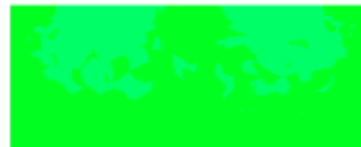


Figure A.2.73  
 X-position: 360

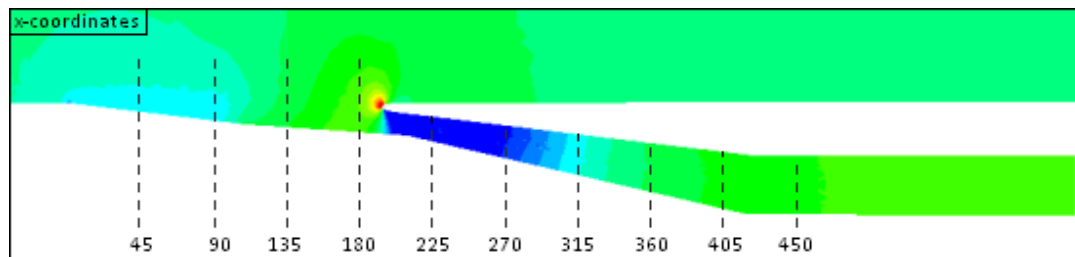


Figure A.2.74

Sideview of the inlet system showing static pressure and x-positions



Figure A.2.75

Inlet static pressure gradient

Mach number plots for an inlet with the variable inlet ramp angle set to 7 degrees  
 Mass flow: 0.20 kg/s

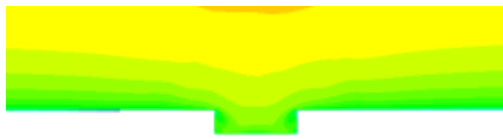


Figure A.2.76  
 X-position: 45

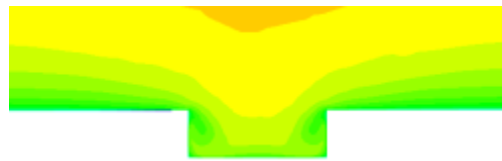


Figure A.2.77  
 X-position: 90

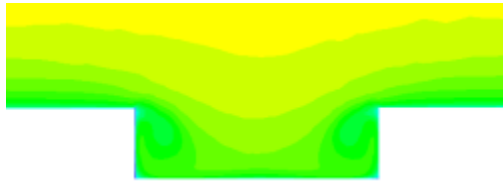


Figure A.2.78  
 X-position: 135

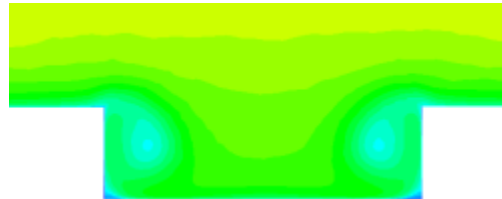


Figure A.2.79  
 X-position: 180



Figure A.2.80  
 X-position: 225

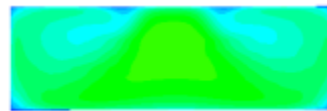


Figure A.2.81  
 X-position: 270

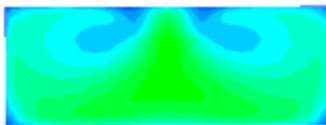


Figure A.2.82  
 X-position: 315

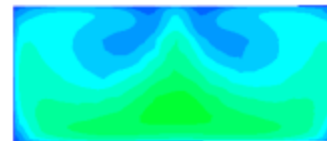


Figure A.2.83  
 X-position: 360

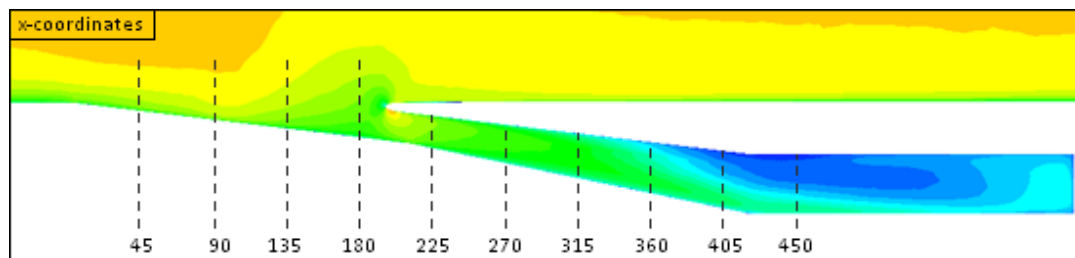


Figure A.2.84

Sideview of the inlet system with Mach number and x-positions

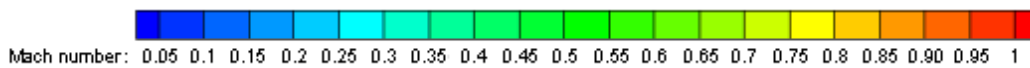


Figure A.2.65

Inlet Mach number gradient

Static pressure plots for an inlet with the variable inlet ramp angle set to 7 degrees  
 Mass flow: 0.20 kg/s



Figure A.2.85  
 X-position: 45



Figure A.2.86  
 X-position: 90

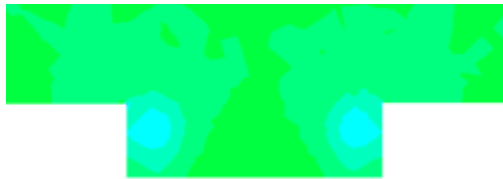


Figure A.2.87  
 X-position: 135



Figure A.2.88  
 X-position: 180



Figure A.2.89  
 X-position: 225



Figure A.2.90  
 X-position: 270



Figure A.2.91  
 X-position: 315



Figure A.2.92  
 X-position: 360

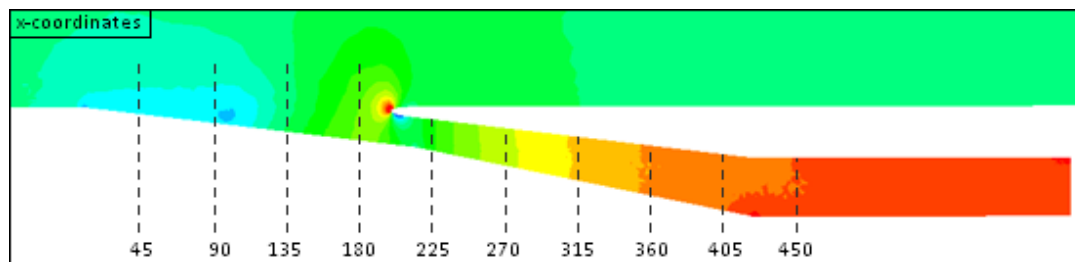


Figure A.2.93

Sideview of the inlet system showing static pressure and x-positions

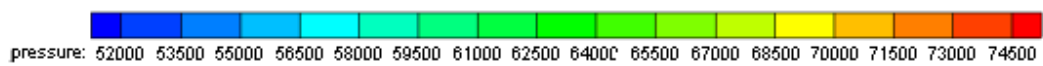


Figure A.2.75  
 Inlet static pressure gradient

A.2.6 Results and Discussion

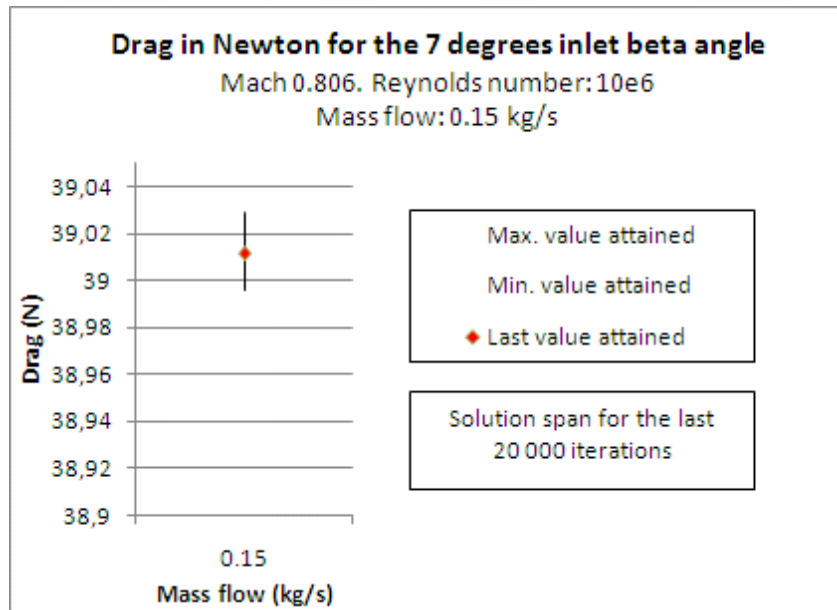


Figure A.2.94

Solution span for the last 20 000 iterations. 7 degrees ramp angle. Mach 0.8. Mass flow: 0.15 kg/s

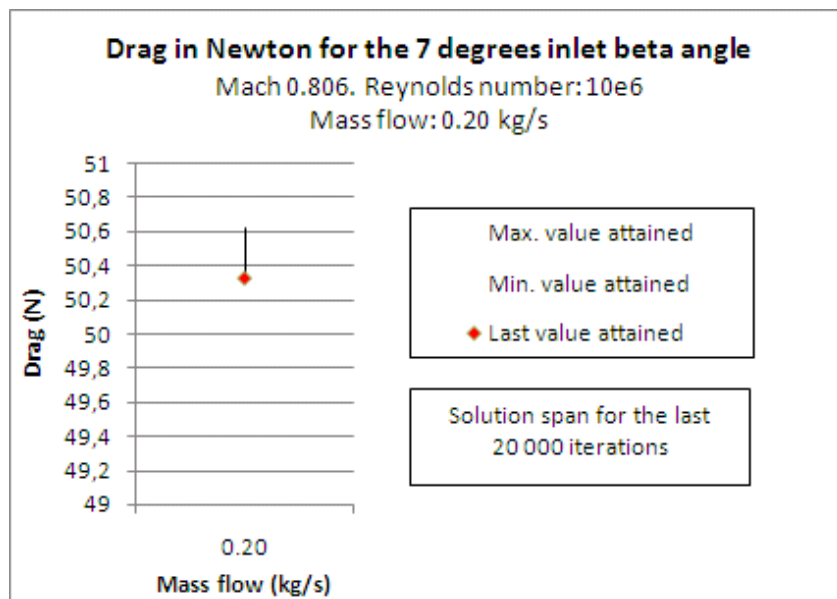


Figure A.2.95

Solution span for the last 20 000 iterations. 7 degrees ramp angle. Mach 0.8. Mass flow: 0.20 kg/s

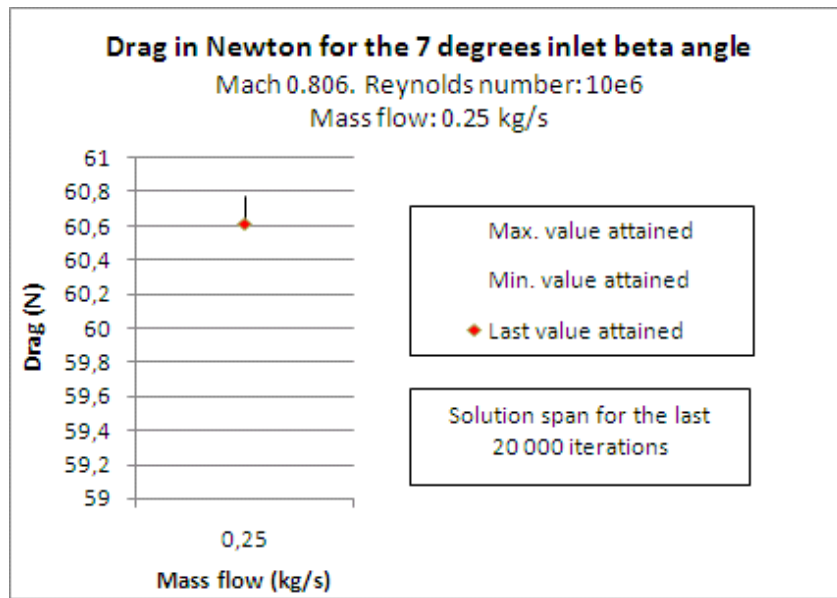


Figure A.2.96

Solution span for the last 20 000 iterations. 7 degrees ramp angle. Mach 0.8. Mass flow: 0.25 kg/s

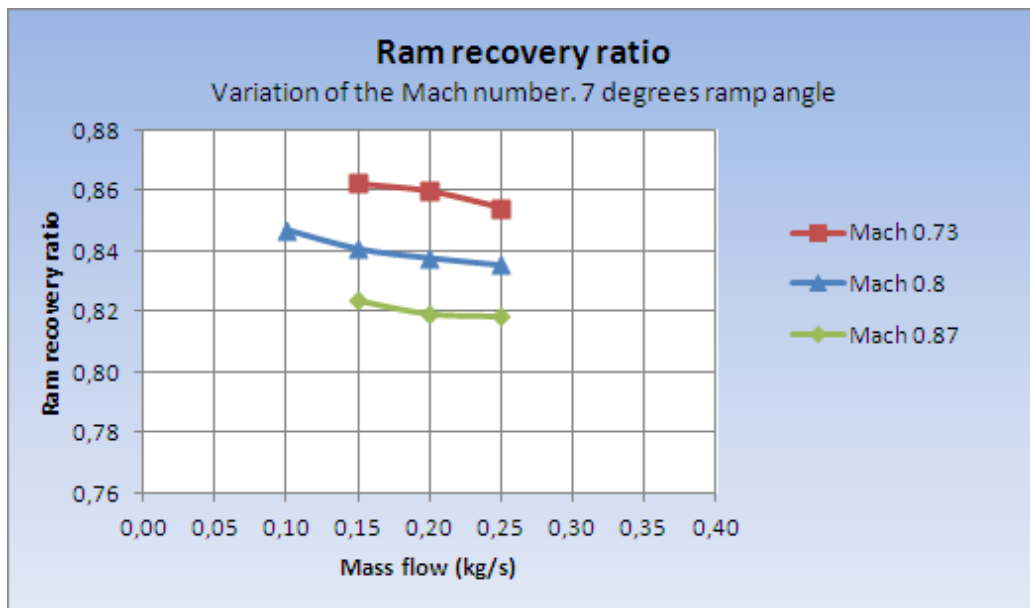


Figure A.2.97

Ram recovery ratio comparison for the 7 degrees ramp angle at different Mach numbers

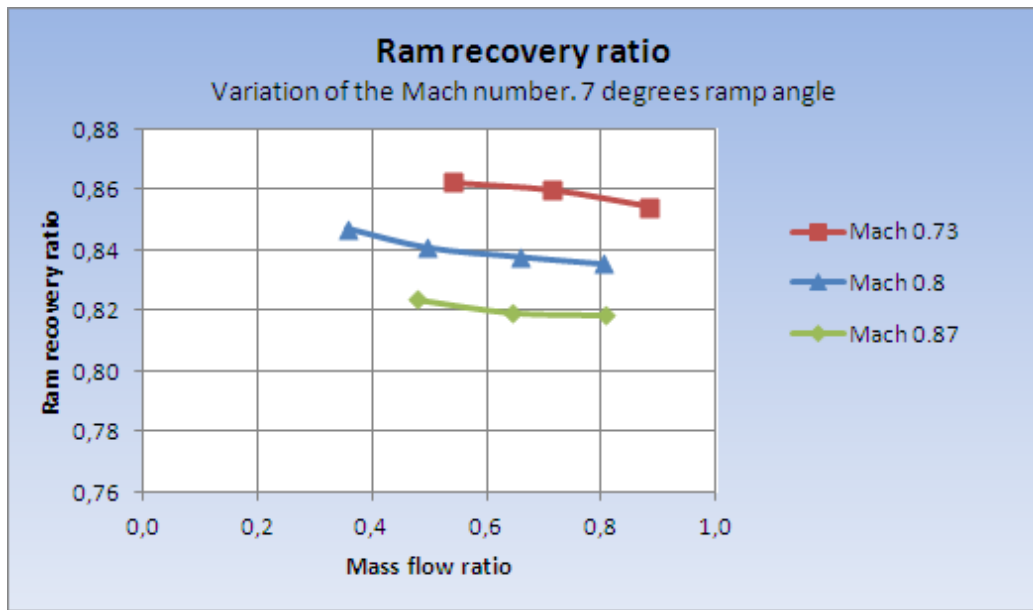


Figure A.2.98

Ram recovery ratio comparison for the 7 degrees ramp angle for different mass flow ratios at different Mach numbers

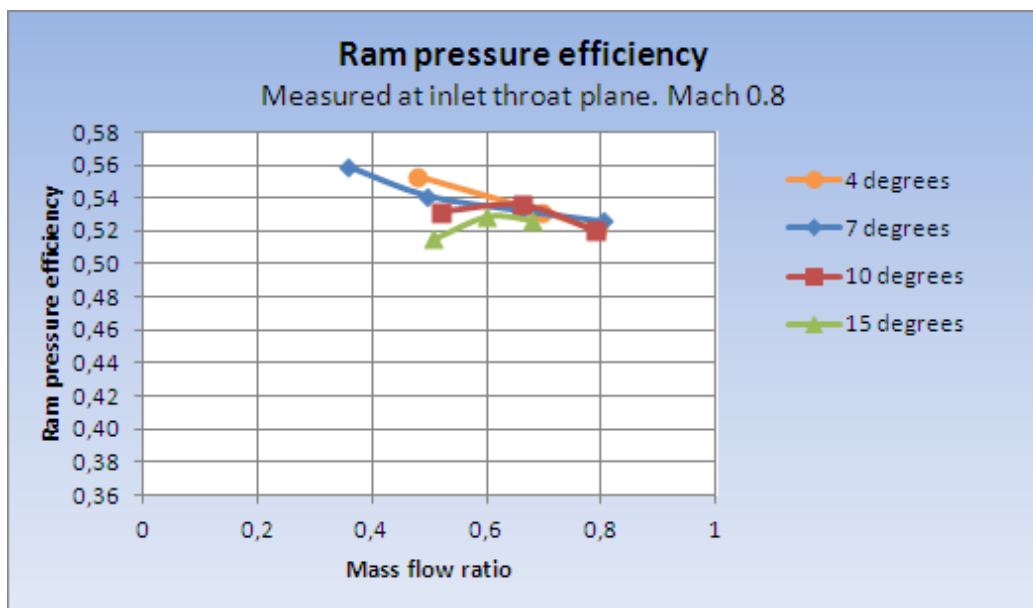


Figure A.2.99

Ram pressure efficiency for different mass flow ratios

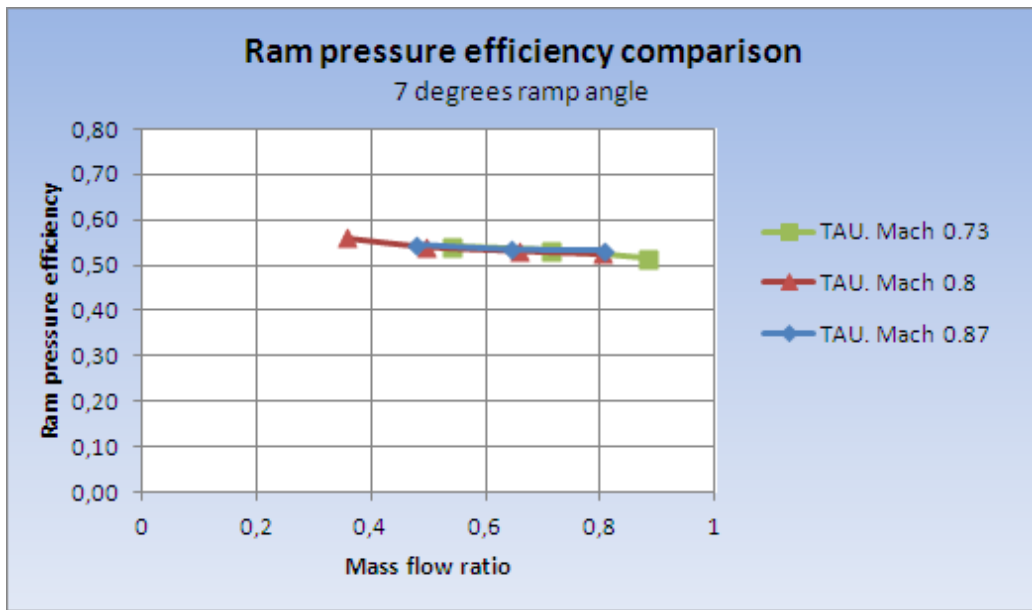


Figure A.2.100  
Ram pressure efficiency for different Mach numbers

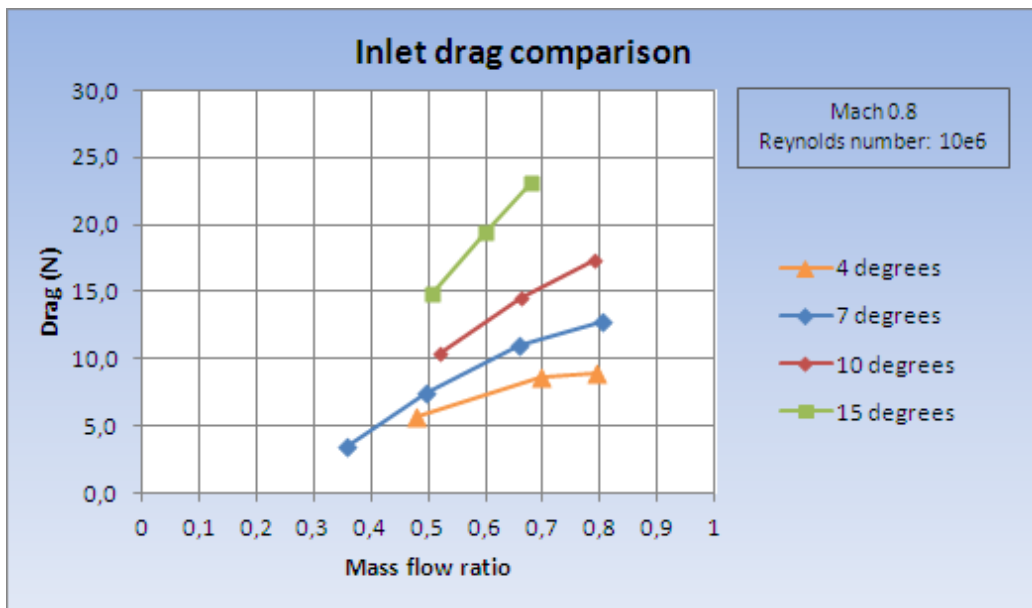


Figure A.2.101  
Drag for the inlet with different ramp angles for different mass flow ratios

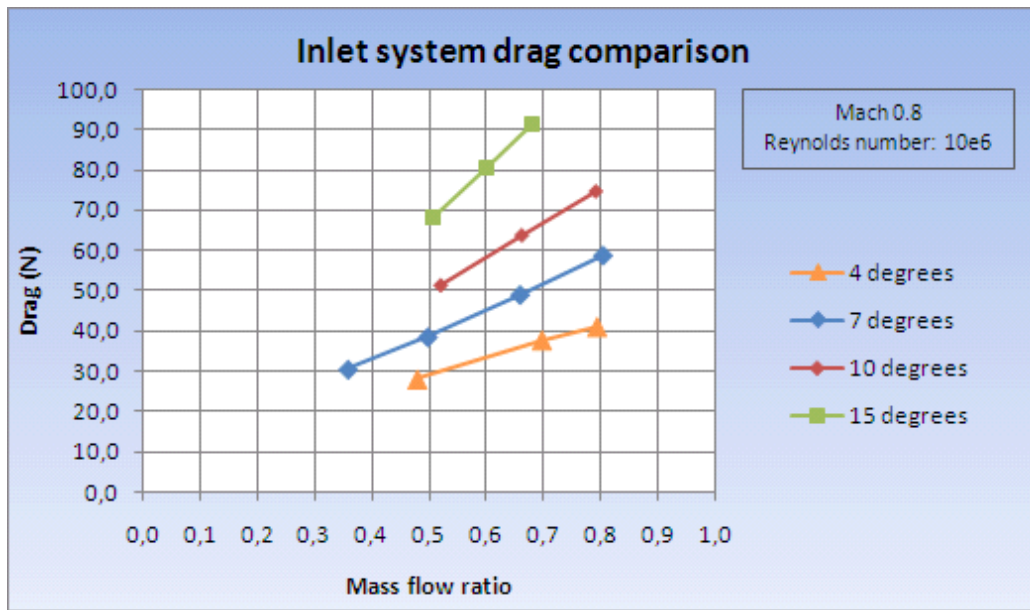


Figure A.2.102

Drag for the inlet system with different inlet ramp angles for different mass flow ratios



## A.3 Lessons Learned and Best Practice Settings

### A.3.1 Mesh Generation

Presented here are the lessons learned during the mesh generation process and the best practice settings used to achieve the end result of a valid mesh for the purpose of investigating an air inlet in a wind tunnel set-up.

#### The Wind Tunnel Floor

Due to irregularities in the prismatic mesh the number of layers was reduced from 35 to 31 prior to the test section. The number of prismatic layers on the wind tunnel floor closest to the inlet was reduced further to 28 layers to achieve a smooth transition into the duct. This could be done without affecting the validity of the solution as Tau<sub>BL</sub> showed that the prismatic layers still covered the boundary layer. Figure A.3.1 - A.3.4 show the prismatic mesh before and after these settings were applied.

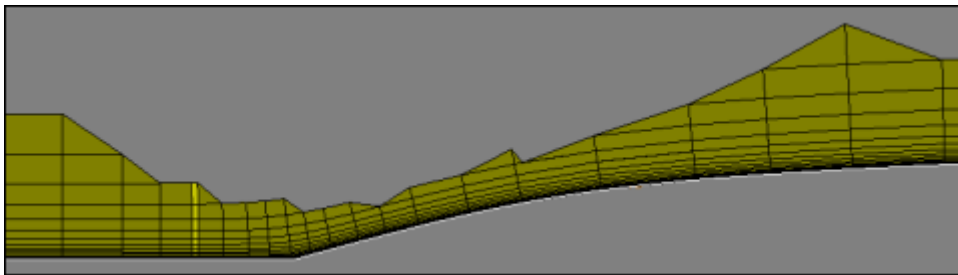


Figure A.3.1

The wind tunnel floor prior to the inlet with 35 prismatic layers

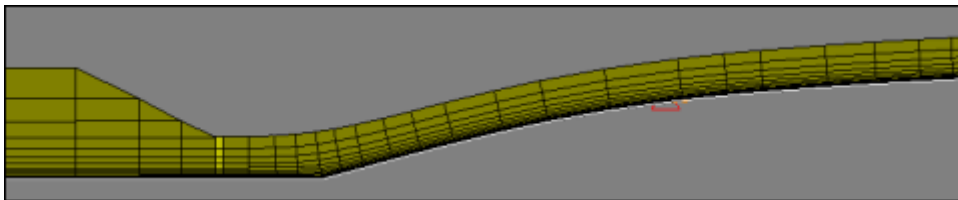


Figure A.3.2

The wind tunnel floor prior to the inlet where 31 prismatic layers transitions to 28 prismatic layers

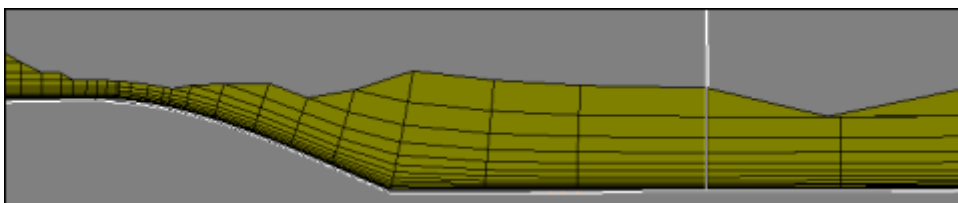


Figure A.3.3

The wind tunnel floor aft of the inlet with 35 prismatic layers

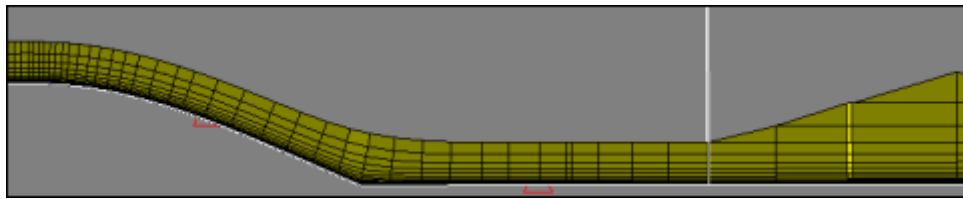


Figure A.3.4

The wind tunnel floor aft of the inlet where 28 prismatic layers transitions to 31 prismatic layers

In addition, three geometrical sources were used at the ramp prior to and aft of the wind tunnel test section. These are shown in Figure A.3.5 below and applies a certain element size at the center of the source and radial stretching. The value of the radial stretching was calculated so that the element size at the outer radius of the source coincide with the surface element size of the affected panels.

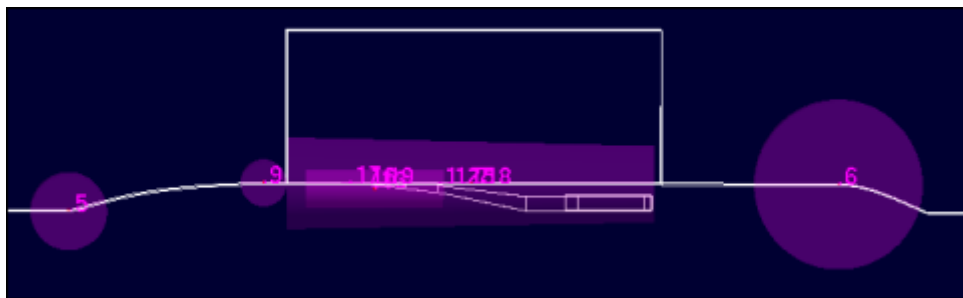


Figure A.3.5

Side view of the geometrical sources at the wind tunnel test section

	Source 5	Source 9	Source 6
Radius (mm):	100	60	220
Surface element size at $r_{min}$ (mm):	8	8	4
Radial stretching:	1.2	1.35	1.11

**Settings Employed for the Inlet**

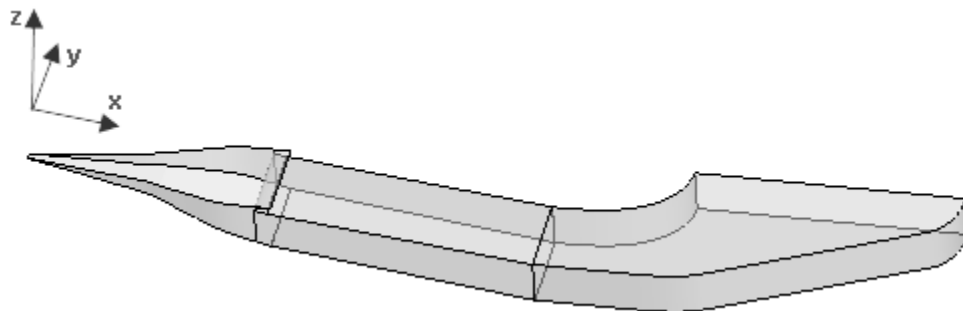


Figure A.3.6

The inlet system with coordinate axis

The surface cell size inside the inlet along the initial ramp was set to 1 millimeters and the number of prismatic layers set to 28. A small distance aft of the entry plane of the inlet the surface size

was increased to 1.5 millimeters and the number of layers to 29. At the start of the plenum where the floor panel of the duct is parallel to the wind tunnel floor, the number of prismatic layers was increased to 30 and remained so for the remainder of the duct. In the inviscid region after the plenum the surface cell size was increased to 3 millimeters. The Stretching ratio used for the prismatic layers inside the duct was 1.31 as this allowed for the recommended number of prismatic layers (28).

### Internal Corners of the Inlet

As described in the Methodology section of this thesis, the internal corners of the inlet proved difficult due unwanted chopping in this area (see Figure A.2.17). This was solved by using the curves defining the inner lower edges of the inlet to create a CAD Source in CENTAUR. The radius used for this source was 5 millimeters and a surface size of 0.3 millimeters. This could be seen in Figure 3.18 shown again below.

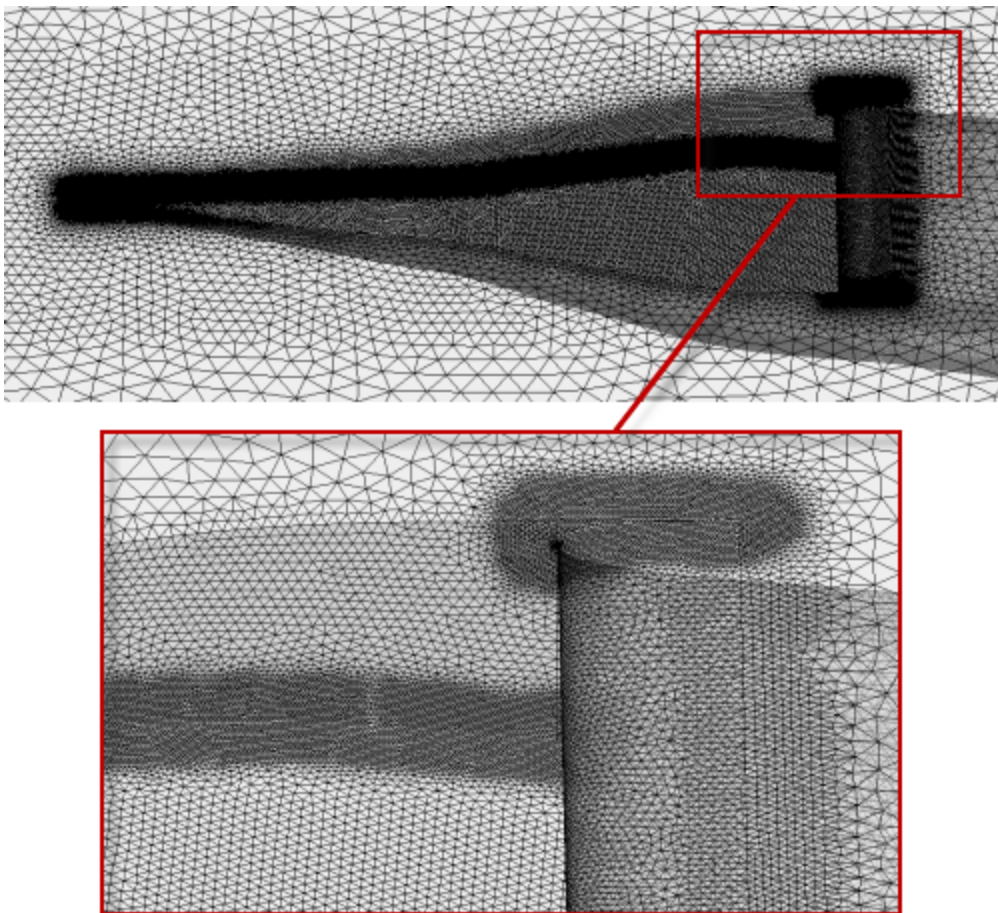


Figure 3.18  
Surface mesh at the inlet

The internal corners of the duct, aft of the initial ramp, were improved in a similar manner by the use of a CAD Source with a radius of 5 millimeters and a surface size of 0.75 millimeters.

### Transition Into the Initial Ramp of the Inlet

The transition of the prismatic layers from the wind tunnel floor into the initial ramp of the inlet was adjusted with two sources. Both applying the same stretching ratio as in the inlet just prior to the ramp and a reduced number of layers inside the inlet to allow for a smoother regrowth of the prismatic layers.

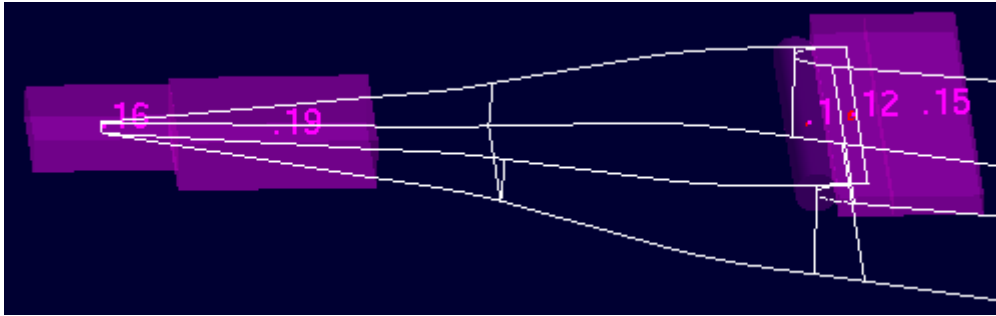


Figure A.3.7

Side view of the sources prior to and aft of the inlet

		Source 16	Source 19
The settings applied are:	No. of layers:	22	26
	Stretching ratio:	1.31	1.31

The initial line that marks the beginning of the inlet was added to the same source as that for the *Internal Corners of the Inlet*. Resulting in a refinement of the surface cell size down to 0.3 millimeters. The countour of the resulting prismatic mesh can be seen below in Figure A.3.8.



Figure A.3.8

Side view of the prismatic layers in the inlet for the 7 degrees constant ramp angle configuration as seen in Tecplot 360

An illustration of the iterative process of trying to find the correct settings to use for the inlet and the inlet transitional sources can be seen in Figure A.3.9. The intention was to capture the boundary layer as much as possible within the prismatic cells. This was best fulfilled by the last shown mesh.

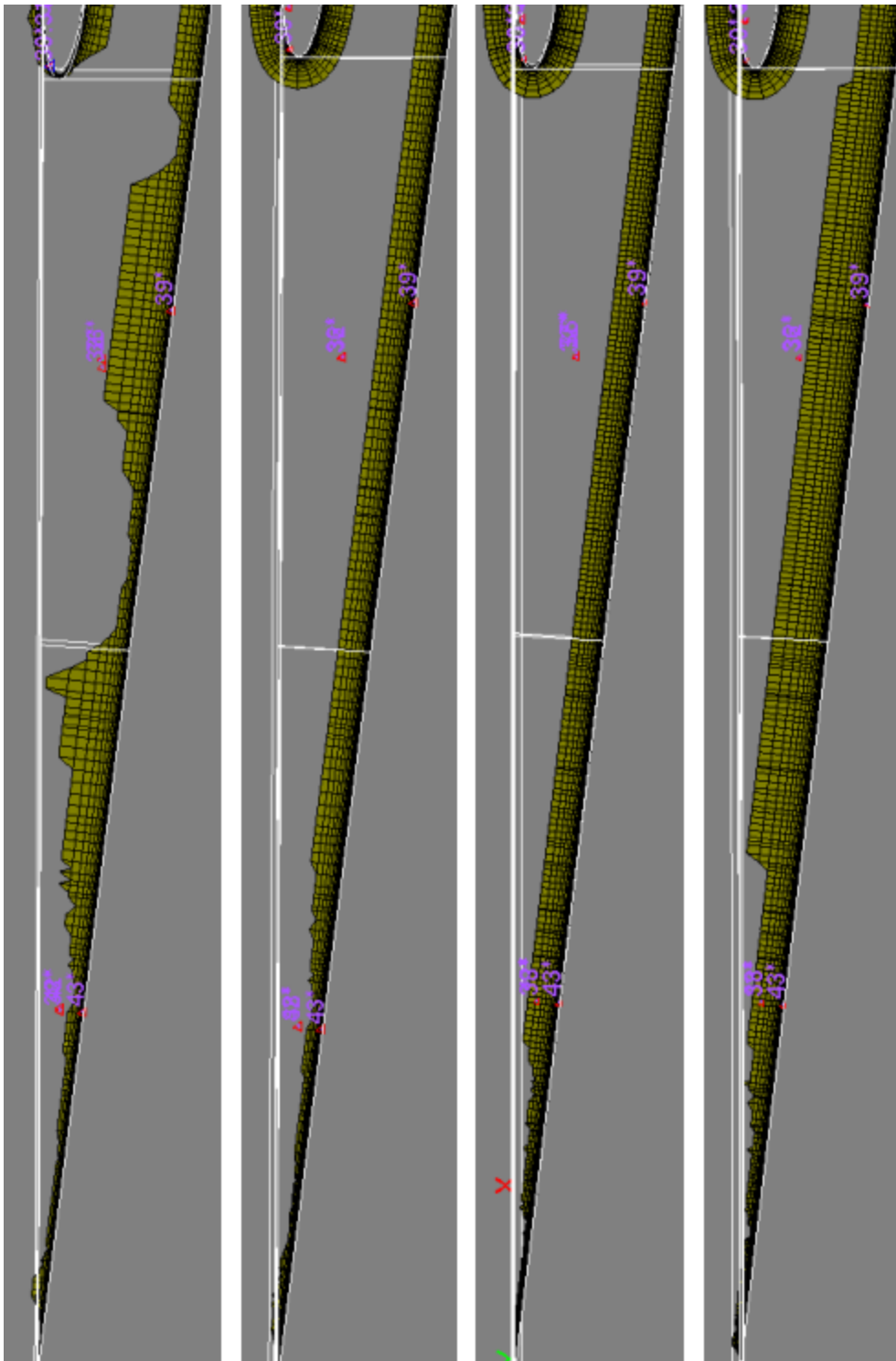


Figure A.3.9

From left to right: The iterative process of attaining the prismatic mesh settings inside the inlet



### Modular Meshing

It proved difficult to reduce the chopping that occurs in the area of the internal bend of the duct. After trying different settings it was at first concluded that a trade-off had to be made. When the source for finer surface elements along the corners of the duct was active (for less chopping in the proximity of the corners), chopping was increased in the middle of the duct. This is clearly seen in Figure A.3.11 - A.3.14.

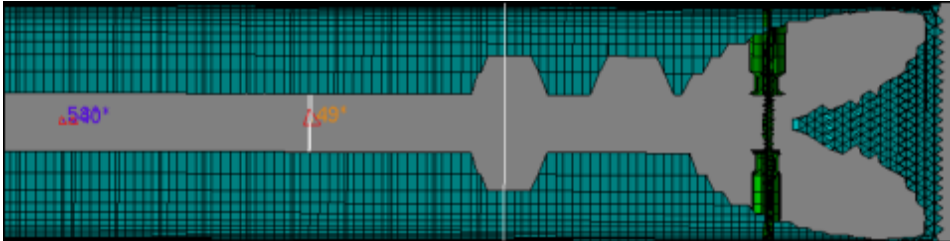


Figure A.3.11  
Side view of the prismatic mesh at the bend of the internal duct.  
CAD Source: inactive.

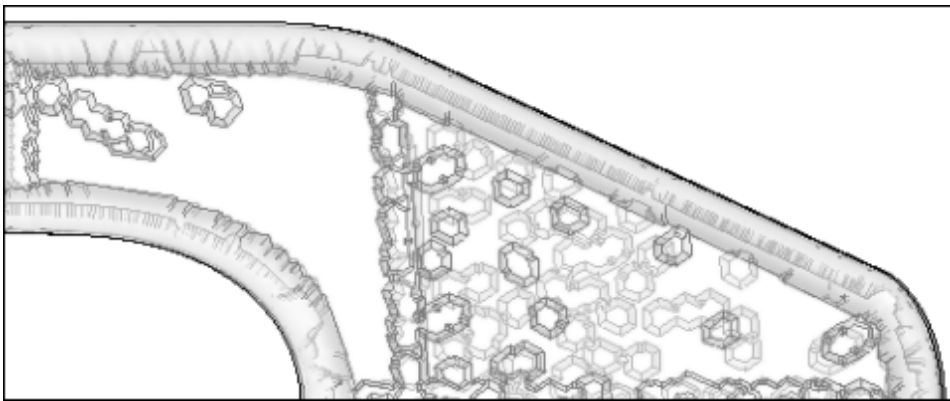


Figure A.3.12  
Bottom view of the prismatic mesh with no surface refinement in the corners as seen in Tecplot 360  
The bumps indicates areas where chopping has occurred.  
CAD Source: inactive.

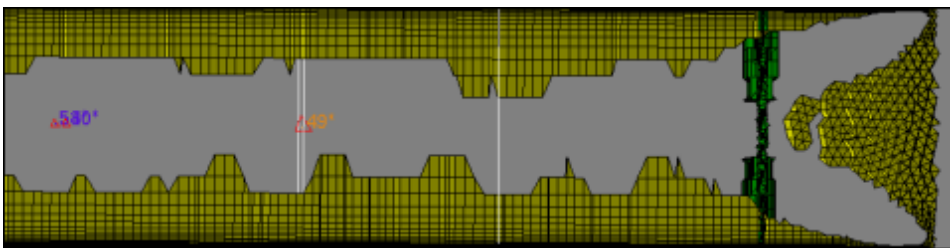


Figure A.3.13  
Side view of the prismatic mesh at the bend of the internal duct.  
CAD Source: active

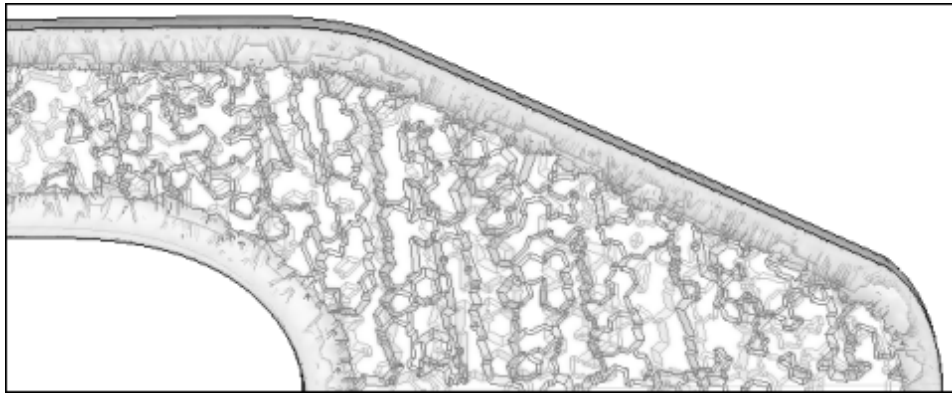


Figure A.3.14

Bottom view of the prismatic mesh with surface refinement in the corners as seen in Tecplot 360  
The bumps indicates areas where chopping has occurred.

CAD Source: active

However, the problem of chopping occurring inside the duct at the bend was avoided completely by the use of modular meshing. By using the modular meshing tool in CENTAUR, where the only the contents of the module is generated, no chopping occurs. It seems that when processing a smaller region, CENTAUR has fewer problems in generating a smooth structured grid. The effect was also seen in other areas such as the inlet. The number of prismatic layers at the transition into the duct earlier described was improved considerably, from 14 layers to 21 layers when modular meshing was used.

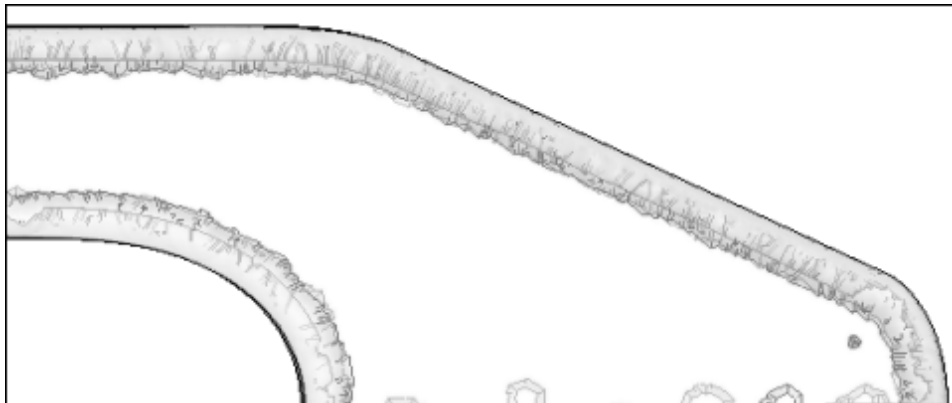


Figure A.3.15

Bottom view of the prismatic mesh with surface refinement in the corners as seen in Tecplot 360 when  
generated with the modular meshing feature



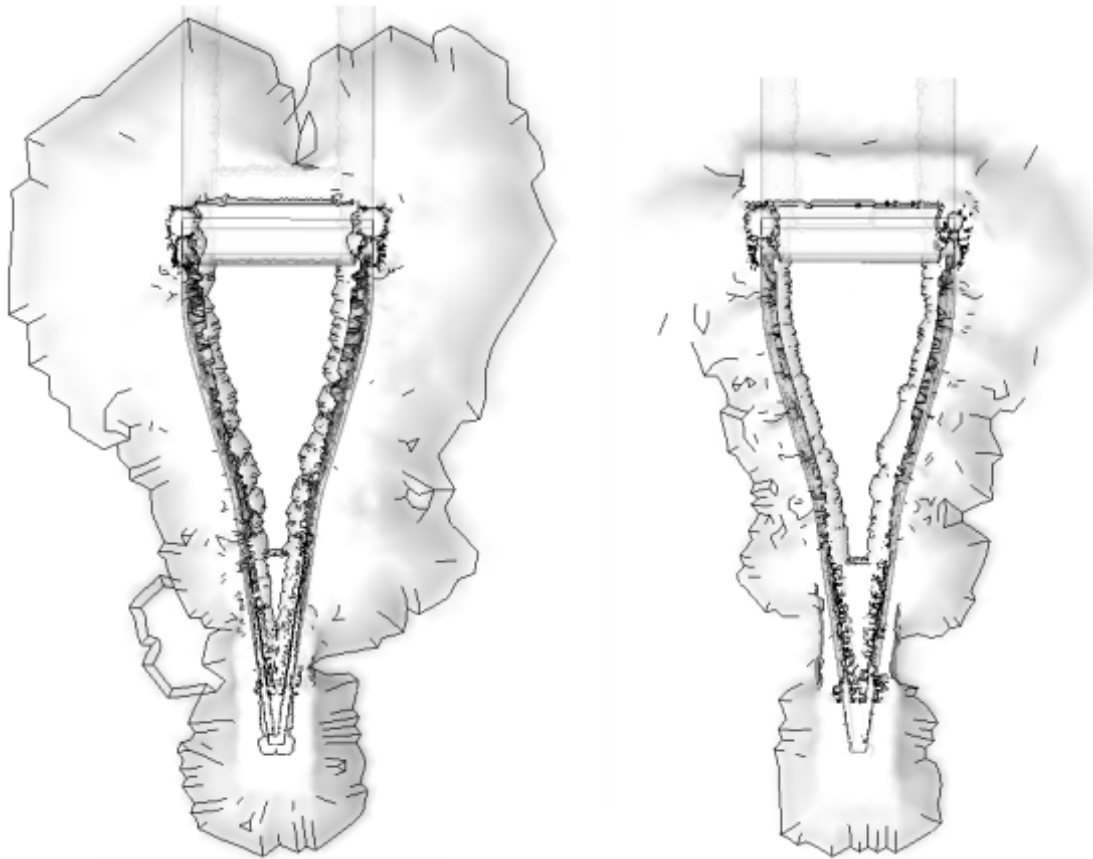


Figure A.3.16

Left: Top view of the inlet in Tecplot when the complete mesh was generated in CEN TAUR in one step  
Right: Top view of the inlet in Tecplot 360 when modular meshing was applied

### Sources and Modular Meshing

When the modular mesh generation process had begun with different geometries of the NACA submerged inlet it was noted that geometrical sources are to be preferred over CAD sources when doing a modular approach. When the geometry inside the modular box is changed, the previous panels and curves are merely hidden from view. This means that all CAD sources has to be connected manually to the panels and curves of the new geometry.

### A.3.2 Numerical Computation

#### Number of Processors

A high number of processors when using TAU is desired to reduce the time needed to attain a solution. This can be restricted by the number of CPUs currently in use, resulting in waiting time if few CPUs are available. Sometimes it might be more time efficient to use a lower number of processors and in effect a shorter waiting time than a high number of CPUs.

The number of processors assigned to successfully perform the calculations of a geometry proved to be of high importance in this thesis. A case which ran fine with 32 processors could crash after just a few hundred iterations with 64 processors. It was suggested by Reference [26] that this might be due to the way the computational mesh is divided into domains for calculation. If by chance the mesh got split in a "troublesome" region it would result in a computational error. Sometimes 64 processors would work fine indicating that the mesh is divided differently each time. This view on the problem was further reinforced when this also occurred for some instances with 32 processors.

## A.4 Calculations

### Calculation of Ram Pressure Efficiency

The ram pressure efficiency estimated by the ESDU method was calculated by hand according to a procedure described in Reference [6]. The calculations will here be presented for the geometry with a constant 7 degrees ramp angle. References will be given to Figures (graphs) found in Reference [6]. Notations can be found in Figure 3.2 in this thesis.

$$\theta = 0.00310781\text{m}$$

$$d_t = 0.01904\text{m}$$

$$d_1 fl = 0.02209\text{m}$$

$$\frac{\text{width}}{\text{depth}} = 3.9$$

$$\frac{\theta}{d_t} = \frac{0.00310781}{0.01904} \approx 0.163$$

For this value of  $\frac{\theta}{d_t}$  Figure 17 in Reference [6] gives:

$$\eta_m = 0.688$$

Which is the maximum ram pressure efficiency for this geometry.

The value of the modified mass flow ratio  $\mu = \frac{\dot{m} d_1 fl}{\dot{m}_0} d_t$  at this ram pressure efficiency can be found in Figure 18 in Reference [6] for the value of  $\frac{\theta}{d_t}$ .

$$\mu_m = 0.345$$

$$\frac{\dot{m}}{\dot{m}_0} = 0.345 \cdot \frac{0.01904}{0.02209} \approx 0.345 \cdot 0.862 \approx 0.297$$

$$\mu - \mu_m = \frac{d_1 fl}{d_t} \left( \frac{\dot{m}}{\dot{m}_0} - 0.297 \right) = \frac{0.02209}{0.01904} \left( \frac{\dot{m}}{\dot{m}_0} - 0.297 \right)$$

The value of  $\eta_{mf}$ , the correction for changes in the modified mass flow ratio, is found in Figure 19a in Reference [6] as a function of  $\mu - \mu_m$ . The mass flow ratios presented for the corresponding mass flow are valid for Mach 0.8.

Mass flow (kg/s)	0.10	0.15	0.20	0.25
$\frac{\dot{m}}{\dot{m}_0}$	0.357	0.497	0.659	0.805
$\mu - \mu_m$	0.070	0.232	0.420	0.589
$\Delta\eta_{mf}$	-0.006	-0.035	-0.050	0.053

Table A.4.1

For  $\frac{\text{width}}{\text{depth}} = 3.9$  and a ramp angle of 7 degrees gives us from Figures 19b and 19c in Reference [6] that:

$$\Delta\eta_\alpha = 0 \text{ and } \Delta\eta_w = 0.$$

The total ram pressure efficiency for the different mass flow ratios are given in Table A.4.2.

Mass flow (kg/s)	0.10	0.15	0.20	0.25
$\frac{\dot{m}}{\dot{m}_0}$	0.357	0.497	0.659	0.805
$\eta_m$	0.688	0.688	0.688	0.688
$\Delta\eta_{mf}$	-0.006	-0.035	-0.050	0.053
$\Delta\eta_\alpha$	0	0	0	0
$\Delta\eta_w$	0	0	0	0
$\eta_{fl}$	<b>0.682</b>	<b>0.653</b>	<b>0.638</b>	<b>0.635</b>

Table A.4.2

Ram pressure efficiency for different mass flow ratios.

### Calculation of Inlet Drag

The inlet drag estimated by the ESDU method was calculated by hand according to a procedure described in Reference [6]. The calculations will here be presented for the geometry with a constant 7 degrees ramp angle. References will be given to Figures (graphs) found in Reference [6]. Notations can be found in Figure 3.2 in this thesis.

$$\theta = 0.00310781\text{m}$$

$$d_t = 0.01904\text{m}$$

$$d_1 fl = 0.02209\text{m}$$

$$d_m fl = 0.02514\text{m}$$

$$\delta = 0.0455912\text{m}$$

$$l_l = 0.01054\text{m}$$

$$\frac{\text{width}}{\text{depth}} = 3.9$$

$$\frac{\delta}{h} = \frac{\delta}{d_1 fl} \approx 2.0639$$

A ramp angle of 7 degrees and Mach 0.8 gives from Figure 10 in Reference [6] gives:

$$k_\psi = 1$$

Figure 2 in Reference [6] gives:

$$\frac{\psi_T}{\psi_0} = 0.62$$

The ram drag component as a function of the mass flow ratio can be seen in Table A.4.3.

Mass flow ratio	0.357	0.497	0.659	0.805
$2K_{fl}$	0.44268	0.0.61628	0.81716	0.9982

Table A.4.3

From Figure 12 in Reference [6]:

$$k_\alpha = 1$$

From Figure 13 in Reference [6]:

$$k_M = 1.7$$

Mass flow ratio	0.357	0.497	0.659	0.805
$k_{spfl}$	0.238	0.1	0	0

Table A.4.4

$C_{Dfl} = 0.159$  (curved, divergent ramp)

Mass flow ratio	0.357	0.497	0.659	0.805
$k_\alpha k_M k_{spfl} C_{Dfl}$	0.064	0.027	0	0

Table A.4.5

Mass flow ratio	0.357	0.497	0.659	0.805
$\Delta C_D$	0	0	0.03	0.11

Table A.4.6

Mass flow ratio	0.357	0.497	0.659	0.805
$2K_{fl}$	0.44268	0.0.61628	0.81716	0.9982
$k_\alpha k_M k_{spfl} C_{Dfl}$	0.064	0.027	0	0
$\Delta C_D$	0	0	0.03	0.11
$C_{Dfl}$	0.50668	0.64328	0.84716	1.1082

Table A.4.7

For a dynamic pressure of 32415 (measured from a TAU solution at Mach 0.8) and a reference area of 0.001414 (Inlet throat area) we can make the following table.

$C_{Dfl}$	0.50668	0.64328	0.84716	1.1082
Drag (N)	<b>23.2</b>	<b>29.5</b>	<b>38.8</b>	<b>50.8</b>

Table A.4.8

A.5 Tables

Variable ramp angle	4°	7°	10°	15°
Initial depth (mm)	13.95	19.04	24.19	33.01
Width/Depth ratio	5.4	3.9	3.1	2.3

Table A.5.1  
Geometry for different ramp angles.

The position where the initial depth is measured can be seen in Figure 3.2, repeated below. It is the measurement denoted as  $d_t$ . The variable ramp angle can be seen in Figure 1.4.

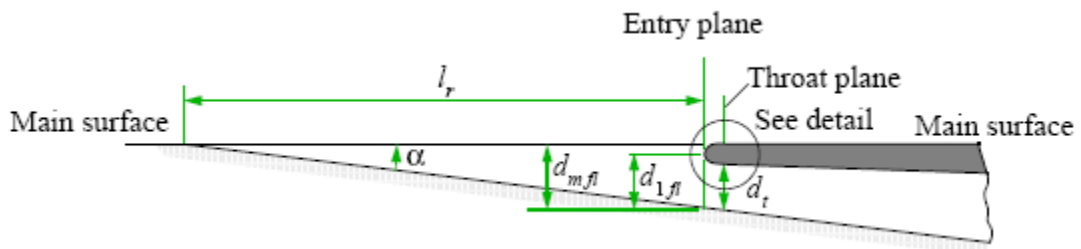


Figure 3.2  
Flush inlet. Figure from Reference [6]

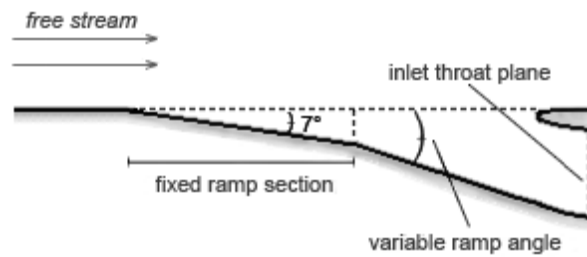


Figure 1.4  
Cross section of an inlet.

Ramp angle	Diffuser angle $\gamma$
4 degrees	6,179 degrees
7 degrees	4,803 degrees
10 degrees	3,415 degrees
15 degrees	1,105 degrees

Table A.5.2  
Diffuser angles for different ramp angles.

The diffuser angle in table A.5.2 is measured between the upper and lower surfaces of the diffuser section of the inlet system referred. This angle is denoted as  $\gamma$  in Figure A.5.1 to illustrate.

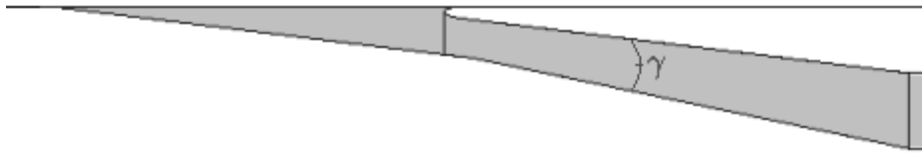


Figure A.5.1  
Cross section of the inlet and diffuser section.

## A.6 Transonic Wind tunnel Göttingen

The following information on the Transonic Wind tunnel Göttingen (TWG) has been cited from Reference [30].

### Type of wind tunnel

The TWG is a closed circuit, continuous, sub-, trans- and supersonic wind tunnel with three exchangeable test sections

### Main features

#### Test sections

- 1 m x 1 m with adaptive walls
- 1 m x 1 m with perforated walls
- 1 m x 1 m with flexible Laval nozzle

#### Operating range

- $0.3 \leq Ma \leq 2.2$
- $30 \text{ kPa} \leq P \leq 150 \text{ kPa}$
- $Re_{lref=0.1m} \leq 1.8 \times 10^6$
- $293 \text{ K} \leq T \leq 315 \text{ K}$

#### Model support

- Sword with integrated roll support
- Remotely controlled roll adapters
- Dynamic roll adapter
- Remotely controlled static and dynamic 2D/half-model supports

#### Auxiliary systems

- Vacuum system
- Pressurized air supply

#### Typical tests

- 2D airfoil tests with flow control devices (e.g. vortex generators, suction, blowing, ventilation, trailing edge devices, MEMs), helicopter blades
- Configuration studies, data set determination of 3D models (missiles, fighters, spacecraft).
- Air intake surveys for fighters and missiles
- Drag bookkeeping with through-flow ducts
- Dynamic tests: free and forced pitch oscillation of dynamically scaled flexible 2D and half-models; flutter and limit cycle oscillation; dynamically linked substructures (nacelle, flap); forced and free-to-roll maneuvers
- Air data system and probe calibration



## A.7 Input Files

### A.7.1 CENTAUR

#### Global surface input file for CENTAUR

```

2 ! Output Level(0-none, 1-normal, 2-detailed)
0 ! Desired number of surface triangles (0=off)
1.8 ! Stretching ratio (1.5-2.1)
1 ! Scaling parameter (0.25-4.0)
F ! Use constant spacing
40 ! Initial/Constant spacing value
80 ! Length Scale in absence of any features
8 ! Minimum Length scale for analytic curvature clustering
T ! Activate interpanel curvature clustering
100 8 ! Angle and factor for interpanel curvature clustering
6 ! Factor for analytic curvature clustering interior to panels
2 ! Factor for proximity clustering
2 ! Factor for CAD clustering

```

#### Global prismatic input file for CENTAUR

```

2 ! Output Level (0-none, 1-normal, 2-detailed)
F ! Read in prismatic gap/cavity detection file (T/F)
0.4 ! Proportion of gaps to be filled by tets (0.2 - 0.8)
0 ! No. of passes for extending cavity area (0-4)
T ! Automatic curve pullback activation(T/F)
100 0.33 ! Min. angle(degrees) at curve for activation; ratio
5 ! Ramp angle(deg)- growth rate on final layer (5-30)
35 ! No. of prismatic layers to be generated (5-30)
0.00535997 ! Initial layer thickness (case dependent)
1.384 ! Stretching factor (1.1-1.5)
T ! Chop prismatic layers (T/F)
0.00134 ! Minimum layer thickness (case dependent)
F ! Use Enhanced Convex Area Treatment (T/F)

```

#### Global tetrahedral input file for CENTAUR

```

2 ! Output Level(0-none, 1-normal, 2-detailed)
F ! Restarting (T/F)?
2 ! Stretching ratio (1.5-2.1)
1 ! Scaling parameter (0.25-4.0)
F ! Limit maximum tetrahedral size
721.189 ! Maximum tet. length scale (if limit is True)
0.5 ! Thickness matching ratio(0.-1.)
1.5 ! Tet./prism interface ratio(1.-3.)
5 ! Tet. Grid Quality (1-lowest - 10-highest)

```

**Module prismatic input file for CENTAUR**

```

2 ! Output Level (0-none, 1-normal, 2-detailed)
F ! Read in prismatic gap/cavity detection file (T/F)
0.2 ! Proportion of gaps to be filled by tets (0.2 - 0.8)
0 ! No. of passes for extending cavity area (0-4)
T ! Automatic curve pullback activation(T/F)
100 0.33 ! Min. angle(degrees) at curve for activation; ratio
5 ! Ramp angle(deg)- growth rate on final layer (5-30)
35 ! No. of prismatic layers to be generated (5-30)
0.00535997 ! Initial layer thickness (case dependent)
1.384 ! Stretching factor (1.1-1.5)
T ! Chop prismatic layers (T/F)
0.00134 ! Minimum layer thickness (case dependent)
F ! Use Enhanced Convex Area Treatment (T/F)

```

**A.7.2 TAU****\*.input file for first 25000 iterations**

```

#-----
#--Main job parameter-----
TITLE: "ecocents_d29_*deg_d05_v05_Ma0.719_Re10.0e6_m0.10_tau2010.2.0_p32"
SUBTITLE: "SAE Turbulence Model, Tau 2010.2.0"
GRID: /h/e2schu/ts2717/home/tau/primgrid_d29_*deg_b05/ecocents_d29_*degrees_b05_S1.000.grid
PARA: ecocents_d29_*deg_d05_v05_Ma0.719_Re10.0e6_m0.10_tau2010.2.0_p32.para
WORK_DIR: .
# RESTART:
#-----
#--LSF specific values (valid for all jobs)-----
JOB.QUEUE: rem_all_loio
JOB.PROJECT: C_RT_ecocents
JOB.GROUP: ug_aerofust
JOB.TAU_VERSION: 2010.2.0
#-----
#--Space for global Tau parameter (valid for all jobs)-----
Preconditioning: (none)
Cut-off value: 3
MG description filename: 5w
Turbulence model version: SAE
Output files prefix: sol/ecocents_d29_*deg_d05_v05_Ma0.719_Re10.0e6_m0.10_tau2010.2.0_p32
PHYSICAL_MODELING: turb1eq
PRIMGRID_HANDLING: run_spart_prep_solv
#-----
#--Job example 3: parameter variation-----
JOB_DIR: .
JOB_PREPARE: 1
JOB_SUBMIT: 1
JOB_NOMAIL: 1
JOB_NAME: t_eco_d29_*deg_d05_v05_Ma0.719_Re10.0e6_m0.10_tau2010.2.0_p32.para

```

```
JOB_CPU: 32
JOB_KEEP_STAGE_SOL: 1
JOB_KEEP_ALL_LOGFILES: 1
#-----
#—Job example 3: parameter variation-----
Maximal time step number: 1000 : 4000 : 5000 : 5000 : 5000 : 5000
Inviscid flux discretization type: Upwind : Central : Central : Central : Central : Central
Order of upwind flux (1-2): 1 : 2 : 2 : 2 : 2 : 2
Order of additional equations (1-2): 1 : 2 : 2 : 2 : 2 : 2
CFL number: 2.0 : 3.0 : 3.0 : 4.0 : 4.0 : 4.0
CFL number (coarse grids): 1.0 : 1.0 : 1.0 : 1.0 : 1.0 : 1.0
Type of mass coupling [14]: None : None : None : None : Fixed_massflow : Fixed_massflow
END
```

### **\*.para file for first 25000 iterations**

```
# TAU Input File (release 2006.1.0-p3)
# for 3D Navier-Stokes Calculation
```

---

#### BOUNDARY MAPPING

---

```
Markers: 1
Type: reservoir-pressure inflow
Subtype: turbulent
Name: Tunnel_In
Monitor mass flow (0/1): 1
Monitor pressure (0/1): 1
Monitor forces (0/1): 1
Write surface data (0/1): 1
Inflow condition type: Fixed_pressure
Fixed/initial pressure: 65000.00
block end
```

---

```
Markers: 2
Type: viscous wall
Subtype: turbulent
Name: entry_section
Monitor forces (0/1): 1
Write surface data (0/1): 1
block end
```

---

```
Markers: 3
Type: viscous wall
Subtype: turbulent
Name: nozzle
Monitor forces (0/1): 1
Write surface data (0/1): 1
block end
```

---

Markers: 4  
Type: exit-pressure outflow  
Subtype: turbulent  
Name: Tunnel\_Out  
Monitor forces (0/1): 1  
Monitor pressure (0/1): 1  
Monitor mass flow (0/1): 1  
Write surface data (0/1): 1  
Outflow condition type: Fixed\_pressure  
Fixed/initial pressure: 40000.00  
Measurement coordinates: 0.0 0.0 0.465  
block end

---

Markers: 5  
Type: viscous wall  
Subtype: turbulent  
Name: exit\_section  
Monitor forces (0/1): 1  
Write surface data (0/1): 1  
block end

---

Markers: 6  
Type: viscous wall  
Subtype: turbulent  
Name: test\_section  
Monitor forces (0/1): 1  
Write surface data (0/1): 1  
block end

---

Markers: 8  
Type: viscous wall  
Subtype: turbulent  
Name: test\_section\_floor  
Monitor forces (0/1): 1  
Write surface data (0/1): 1  
block end

---

Markers: 9  
Type: viscous wall  
Subtype: turbulent  
Name: test\_section\_aft\_ramp  
Monitor forces (0/1): 1  
Write surface data (0/1): 1  
block end

---

Markers: 10  
Type: viscous wall  
Subtype: turbulent

Name: module8\_bend  
Monitor forces (0/1): 1  
Write surface data (0/1): 1  
block end

---

Markers: 11  
Type: viscous wall  
Subtype: turbulent  
Name: module8\_2nd\_ramp  
Monitor forces (0/1): 1  
Write surface data (0/1): 1  
block end

---

Markers: 12  
Type: viscous wall  
Subtype: turbulent  
Name: module8\_tunnel\_floor  
Monitor forces (0/1): 1  
Write surface data (0/1): 1  
block end

---

Markers: 13  
Type: euler wall  
Name: module8\_outlet\_hexa\_inviscid  
Monitor forces (0/1): 1  
Write surface data (0/1): 1  
block end

---

Markers: 14  
Type: engine inflow  
Name: module8\_outlet  
Engine number: 1  
Engine inflow direction: 0 -1 0  
Inflow condition type: Fixed\_pressure  
Fixed/initial pressure: 50000.  
# Inflow condition type: Fixed\_massflow  
Type of mass coupling: Fixed\_massflow  
Fixed massflow: 0.10  
Match measured pressure (0/1): 0  
Relaxation factor: 0.1  
Regulator (0/1): 1  
Massflow convergence residual: 0.01  
Extrapolation type simple/characteristic (0/1): 1  
Matching iteration period: 3  
Measurement coordinates: 0.64146 0.0975 -0.051768  
Monitor mass flow (0/1): 1  
Monitor pressure (0/1): 1  
Monitor forces (0/1): 1  
Monitor impulse (0/1): 1

Write surface data (0/1): 1  
 Cutting plane allowed (0/1): 0  
 block end

---

Markers: 15  
 Type: viscous wall  
 Subtype: turbulent  
 Name: module8\_intake  
 Monitor forces (0/1): 1  
 Write surface data (0/1): 1  
 block end

---

Markers: 16  
 Type: viscous wall  
 Subtype: turbulent  
 Name: module8\_tunnel\_wall  
 Monitor forces (0/1): 1  
 Write surface data (0/1): 1  
 block end

---

Surface output	
Surface output values:	xyz_rho_v_mach_cp_p_Ptot_temp_cf_cfxyz_fxyz_massflux_eddy _vxyzedge_bldatasw_bldatacf_ltflag_blinfo_bldelta_yplus
Surface output period:	100000

---

Extra field pointdata output	
Field output description file:	(thisfile)
Field output values:	xyz_cp_Ptot_vxyzgeod_mach_macht_temp_gradrho_gradp_ _gradu_gradv_gradw_vort_tu_Nk_vort_visc_wdist

---

PREPROCESSING	
Number of multigrid levels:	5
Cache-coloring (0/max_faces in color):	50000
Bandwidth optimisation (0/1):	1
Point fusing reward:	1.2
Structured grid coarsening:	0
Sharp edge angle (degrees):	0
Output level:	20
Partitioning _____:	-
Number of primary grid domains:	1
Number of domains:	32
Type of partitioning (name):	private
Additional _____:	-
2D offset vector (0 / x=1,y=2,z=3):	0
Compute lugs mapping (0/1):	1
Files/IO _____:	-
Primary grid filename:	primgrid/ecocents_d29_7degrees_b05_S1.000.grid
# Restart-data prefix:	sol/
Grid prefix:	dua/ecocents_d29_*degrees_b05_S1.000.grid
Output files prefix:	sol/ecocents_d29_07deg_d05_v05_ _Ma0.719_Re10.0e6_m0.10_tau2010.2.0_p32

```

Boundary mapping filename: (thisfile)
Plane output description file: (thisfile)
Surface output description file: (thisfile)
Field output description file: (thisfile)
: -
Automatic parameter update (0/1): 1
Write pointdata dimensionless (0/1): 0
Timestepping Start/Stop -----: -
      Output period: 200000
      Current time step number: -1
      Maximal time step number: 1000
      Minimum residual: 1e-16
      # Matching period: 150
Viscous -----: -
      Viscous calculation (0/1): 1
Geometry -----: -
      Grid scale: 0.001
      Reference relation area: 1000000.
Reference length (pitching momentum): 1000.
Reference length (rolling/yawing momentum): 1000.
      Origin coordinate x: 0.
      Origin coordinate y: 0.
      Origin coordinate z: 0.
Monitoring -----: -
      Monitor history (0/1): 1
      Residual monitoring type (0/1): 1
      Monitoring values: Residual_Max-res.drk/dt.drk2/dt.dnue/dt.C-drag-
                        _C-sidef.C-lift.C-mx.C-my.C-mz.Fx.Fy.Fz.Mx_
                        _My.Mz_Angle-a_Angle-b_Max-y+_Max-eddyv_
                        _X-max-res_Y-max-res_Z-max-res
Memory management -----: -
      Increase memory (0/1): 1
Variables -----: -
      Fix negative values (0/1): 0
Flux -----: -
      Inviscid flux discretization type: Central
      Central dissipation scheme: Scalar_dissipation
      2nd order dissipation coefficient: 0.5
Inverse 4th order dissipation coefficient: 64
      Coarse grid upwind flux: Van_Leer
      Upwind flux: AUSMDV
      Order of upwind flux (1-2): 2
      Order of additional equations (1-2): 2
      Mach number limit for limiter: 0
      AUSMDV shock fix (0/1): 0
      Asum scheme dissipation: 0.25
      Relaxation solver: Backward_Euler
Limiter -----: -
      Limiter freezing convergence: 0
Flowfield initialization -----: -
      Init total conditions (0/1): 0
Runge Kutta -----: -
      Number of Runge-Kutta stages: 3

```

```

Multigrid -----: -
      MG description filename: 5w
      SG start up steps (fine grid): 500
Full multigrid -----: -
      Multigrid start level: 1
Maximal time step number (coarse grids): 1000
      Minimum residual (coarse grids): 1e-05
Timestepsize -----: -
      CFL number: 2.0
      CFL number (coarse grids): 2.0
      CFL number (large grad p): -1
Smoother -----: -
      Residual smoother: Point_explicit
      Correction smoother: Point_explicit
      Correction smooth epsilon: -1
      Residual smooth epsilon: -1
      Correction smoothing steps: 2
      Residual smoothing steps: 2
      # Smoothing relaxation steps: 2
Turbulence -----: -
Turbulence equations use multigrid (0/1): 0
Perfect gas thermodynamic -----: -
      Gas constant R: 287
      Gas constant gamma: 1.4
Transport coefficients -----: -
      Prandtl number: 0.72
      Sutherland constant: 110.4
      Sutherland reference viscosity: 1.98586834062e-05
      Sutherland reference temperature: 271.88
References -----: -
      Reference velocity: 237.71
      Reference temperature: 271.88
      Reference pressure: 65000.00
      Reynolds length: 1000.
      Updates
-----

```

### \*.input file for the next 30000 iterations

The settings used for the last iteration steps defined in this input file are used for all additional iterations.

```

#-----
#--Main job parameter-----

TITLE: "ecocents_d29_*deg_d05_v05_Ma0.739_Re10.0e6_m0.10_tau2010.2.0_p32restart"
SUBTITLE: "SAE Turbulence Model, Tau 2010.2.0"
GRID: /h/e2schu/ts2717/home/tau/primgrid_d29_*deg_b05/ecocents_d29_*degrees_b05_S1.000.grid
PARA: ecocents_d29_*deg_d05_v05_Ma0.739_Re10.0e6_m0.10_tau2010.2.0_p32.para
WORK_DIR: .
RESTART: /h/e2schu/ts2717/home/tau/eco_d29_*deg_d05_v04_Ma0.739_Re10.0e6_m0.05_
_tau2010.2.0_p32restart/sol/ecocents_d29_*deg_d05_v02_Ma0.719_Re10.0e6_m0.40_
_tau2010.2.0_p32.pval.25000

#-----
#--LSF specific values (valid for all jobs)-----

JOB_QUEUE: rem_all_loio

```



JOB\_PROJECT: C\_RT\_ecocents  
JOB\_GROUP: ug\_aerofust  
JOB\_TAU\_VERSION: 2010.2.0

#-----  
#—Space for global Tau parameter (valid for all jobs)-----

Preconditioning: (none)  
Cut-off value: 3  
MG description filename: 5w  
Turbulence model version: SAE  
Output files prefix: sol/ecocents.d29.\*deg.d05.v05\_Ma0.739\_Re10.0e6\_m0.10\_tau2010.2.0\_p32  
PHYSICAL\_MODELLING: turb1eq  
PRIMGRID\_HANDLING: run\_spart\_prep\_solv

#-----  
#—Job example 3: parameter variation-----

JOB\_DIR: .  
JOB\_PREPARE: 1  
JOB\_SUBMIT: 1  
JOB\_NOMAIL: 1  
JOB\_NAME: t\_eco.d29.\*deg.d05.v05\_Ma0.739\_Re10.0e6\_m0.10\_tau2010.2.0\_p32.para  
JOB\_CPU: 32  
JOB\_KEEP\_STAGE\_SOL: 1  
JOB\_KEEP\_ALL\_LOGFILES: 1

#-----  
#—Job example 3: parameter variation-----

Maximal time step number: 5000 : 5000 : 5000 : 5000 : 5000 : 5000  
Inviscid flux discretization type: Central : Central : Central : Central : Central : Central  
Order of upwind flux (1-2): 2 : 2 : 2 : 2 : 2 : 2  
Order of additional equations (1-2): 2 : 2 : 2 : 2 : 2 : 2  
CFL number: 2.0 : 3.0 : 3.2 : 3.5 : 3.8 : 4.0  
CFL number (coarse grids): 1.0 : 1.0 : 1.0 : 1.0 : 1.0 : 1.0  
Type of mass coupling [14]: None : None : Fixed\_massflow : Fixed\_massflow : Fixed\_massflow : Fixed\_massflow  
END

### **\*.para file for the next 75000 iterations**

# TAU Input File (release 2006.1.0-p3)  
# for 3D Navier-Stokes Calculation

-----  
BOUNDARY MAPPING

-----  
Markers: 1  
Type: reservoir-pressure inflow  
Subtype: turbulent  
Name: Tunnel\_In

Monitor mass flow (0/1): 1  
Monitor pressure (0/1): 1  
Monitor forces (0/1): 1  
Write surface data (0/1): 1  
Inflow condition type: Fixed\_pressure  
Fixed/initial pressure: 65000.00  
block end

---

Markers: 2  
Type: viscous wall  
Subtype: turbulent  
Name: entry\_section  
Monitor forces (0/1): 1  
Write surface data (0/1): 1  
block end

---

Markers: 3  
Type: viscous wall  
Subtype: turbulent  
Name: nozzle  
Monitor forces (0/1): 1  
Write surface data (0/1): 1  
block end

---

Markers: 4  
Type: exit-pressure outflow  
Subtype: turbulent  
Name: Tunnel\_Out  
Monitor forces (0/1): 1  
Monitor pressure (0/1): 1  
Monitor mass flow (0/1): 1  
Write surface data (0/1): 1  
Outflow condition type: Fixed\_pressure  
Fixed/initial pressure: 40000.00  
Measurement coordinates: 0.0 0.0 0.465  
block end

---

Markers: 5  
Type: viscous wall  
Subtype: turbulent  
Name: exit\_section  
Monitor forces (0/1): 1  
Write surface data (0/1): 1  
block end

---

Markers: 6  
Type: viscous wall  
Subtype: turbulent  
Name: test\_section

---

Monitor forces (0/1): 1  
Write surface data (0/1): 1  
block end

---

Markers: 8  
Type: viscous wall  
Subtype: turbulent  
Name: test\_section\_floor  
Monitor forces (0/1): 1  
Write surface data (0/1): 1  
block end

---

Markers: 9  
Type: viscous wall  
Subtype: turbulent  
Name: test\_section\_aft\_ramp  
Monitor forces (0/1): 1  
Write surface data (0/1): 1  
block end

---

Markers: 10  
Type: viscous wall  
Subtype: turbulent  
Name: module8\_bend  
Monitor forces (0/1): 1  
Write surface data (0/1): 1  
block end

---

Markers: 11  
Type: viscous wall  
Subtype: turbulent  
Name: module8\_2nd\_ramp  
Monitor forces (0/1): 1  
Write surface data (0/1): 1  
block end

---

Markers: 12  
Type: viscous wall  
Subtype: turbulent  
Name: module8\_tunnel\_floor  
Monitor forces (0/1): 1  
Write surface data (0/1): 1  
block end

---

Markers: 13  
Type: euler wall  
Name: module8\_outlet\_hexa\_inviscid  
Monitor forces (0/1): 1  
Write surface data (0/1): 1

block end

---

Markers: 14  
Type: engine inflow  
Name: module8\_outlet  
Engine number: 1  
Engine inflow direction: 0 -1 0  
Inflow condition type: Fixed\_pressure  
Fixed/initial pressure: 50000.  
# Inflow condition type: Fixed\_massflow  
Type of mass coupling: Fixed\_massflow  
Fixed massflow: 0.10  
Match measured pressure (0/1): 0  
Relaxation factor: 0.001  
Regulator (0/1): 1  
Massflow convergence residual: 0.001  
Extrapolation type simple/characteristic (0/1): 1  
Matching iteration period: 3  
Measurement coordinates: 0.64146 0.0975 -0.051768  
Monitor mass flow (0/1): 1  
Monitor pressure (0/1): 1  
Monitor forces (0/1): 1  
Monitor impulse (0/1): 1  
Write surface data (0/1): 1  
Cutting plane allowed (0/1): 0  
block end

---

Markers: 15  
Type: viscous wall  
Subtype: turbulent  
Name: module8\_intake  
Monitor forces (0/1): 1  
Write surface data (0/1): 1  
block end

---

Markers: 16  
Type: viscous wall  
Subtype: turbulent  
Name: module8\_tunnel\_wall  
Monitor forces (0/1): 1  
Write surface data (0/1): 1  
block end

---

Surface output

---

Surface output values: xyz\_rho\_v\_mach\_cp\_p\_Ptot\_temp\_cf\_cxyz\_  
\_fxyz\_massflux\_eddy\_vxyzedge\_bldatasw\_bldatacf\_  
\_lflag\_blinfo\_bldelta\_yplus

Surface output period: 100000

---

Extra field pointdata output

---

Field output description file: (thisfile)  
Field output values: xyz\_cp\_Ptot\_vxyzgeod\_mach\_macht\_temp\_gradrho\_gradp\_  
\_gradu\_gradv\_gradw\_vort\_tu\_Nk\_vort\_visc\_wdist

---

PREPROCESSING

---

Number of multigrid levels: 5  
Cache-coloring (0/max\_faces in color): 50000  
Bandwidth optimisation (0/1): 1  
Point fusing reward: 1.2  
Structured grid coarsening: 0  
Sharp edge angle (degrees): 0  
Output level: 20

Partitioning -----: -  
Number of primary grid domains: 1  
Number of domains: 32  
Type of partitioning (name): private

Additional -----: -  
2D offset vector (0 / x=1,y=2,z=3): 0  
Compute lugs mapping (0/1): 1

Files/IO -----: -  
Primary grid filename: primgrid/ecocents\_d29\_\*.degrees\_b05\_S1.000.grid  
# Restart-data prefix: sol/  
Grid prefix: dua/ecocents\_d29\_\*.degrees\_b05\_S1.000.grid  
Output files prefix: sol/ecocents\_d29\_\*deg\_d05\_v05\_  
\_Ma0.739\_Re10.0e6\_m0.10\_tau2010.2.0\_p32  
Boundary mapping filename: (thisfile)  
Plane output description file: (thisfile)  
Surface output description file: (thisfile)  
Field output description file: (thisfile)  
: -  
Automatic parameter update (0/1): 1  
Write pointdata dimensionless (0/1): 0

Timestepping Start/Stop -----: -  
Output period: 200000  
Current time step number: -1  
Maximal time step number: 1000  
Minimum residual: 1e-16  
# Matching period: 150

Viscous -----: -  
Viscous calculation (0/1): 1

```

Geometry -----: -
      Grid scale: 0.001
      Reference relation area: 1000000.
      Reference length (pitching momentum): 1000.
Reference length (rolling/yawing momentum): 1000.
      Origin coordinate x: 0.
      Origin coordinate y: 0.
      Origin coordinate z: 0.
Monitoring -----: -
      Monitor history (0/1): 1
      Residual monitoring type (0/1): 1
      Monitoring values: Residual_Max-res.drk/dt_drk2/dt_dnue/dt_C-drag-
                        _C-sidef_C-lift_C-mx_C-my_C-mz_Fx_Fy_Fz_Mx_
                        _My_Mz_Angle-a_Angle-b_Max-y+_Max-eddyv_
                        _X-max-res_Y-max-res_Z-max-res
Memory management -----: -
      Increase memory (0/1): 1
Variables -----: -
      Fix negative values (0/1): 0
Flux -----: -
      Inviscid flux discretization type: Central
      Central dissipation scheme: Scalar_dissipation
      2nd order dissipation coefficient: 0.5
      Inverse 4th order dissipation coefficient: 64
      Coarse grid upwind flux: Van_Leer
      Upwind flux: AUSMDV
      Order of upwind flux (1-2): 2
      Order of additional equations (1-2): 2
      Mach number limit for limiter: 0
      AUSMDV shock fix (0/1): 0
      Ausm scheme dissipation: 0.25
      Relaxation solver: Backward_Euler
Limiter -----: -
      Limiter freezing convergence: 0
Flowfield initialization -----: -
      Init total conditions (0/1): 0
Runge Kutta -----: -
      Number of Runge-Kutta stages: 3
Multigrid -----: -
      MG description filename: 5w
      SG start up steps (fine grid): 500
Full multigrid -----: -
      Multigrid start level: 1
Maximal time step number (coarse grids): 1000
      Minimum residual (coarse grids): 1e-05
Dual time -----: -
      Unsteady time stepping: (none)
      Unsteady show pseudo time steps (0/1): 0
      Unsteady physical time step size: 0.001
      Unsteady physical time steps: 1
      Unsteady inner iterations per time step: 40
Timestepsize -----: -
      CFL number: 2.0
      CFL number (coarse grids): 2.0
      CFL number (large grad p): -1

```

```

Smoother -----: -
      Residual smoother: Point_explicit
      Correction smoother: Point_explicit
      Correction smooth epsilon: -1
      Residual smooth epsilon: -1
      Correction smoothing steps: 2
      Residual smoothing steps: 2
      # Smoothing relaxation steps: 2
Turbulence -----: -
Turbulence equations use multigrid (0/1): 0
Perfect gas thermodynamic -----: -
      Gas constant R: 287
      Gas constant gamma: 1.4
Transport coefficients -----: -
      Prandtl number: 0.72
      Sutherland constant: 110.4
      Sutherland reference viscosity: 2.0358e-05
      Sutherland reference temperature: 271.88
References -----: -
      Reference velocity: 244.40
      Reference temperature: 271.88
      Reference pressure: 65000.00
      Reynolds length: 1000.
      Updates
-----
setup_taujob in stage number <6>
solver in stage number <6>
Restart-data prefix: /h/e2schu/ts2717/home/tau/eco_d29_*deg_d05_
_v04_Ma0.739_Re10.0e6_m0.05_tau2010.2.0_p32restart/
/sol/ecocents_d29_*deg_d05_v02_Ma0.719_Re10.0e6_
_m0.40_tau2010.2.0_p32.pval.25000
Surface output filename: /h/e2schu/ts2717/home/tau/eco_d29_*deg_d05_
_v04_Ma0.739_Re10.0e6_m0.05_tau2010.2.0_p32restart/
/sol/ecocents_d29_*deg_d05_v02_Ma0.719_Re10.0e6_
_m0.40_tau2010.2.0_p32.surface.pval.25000
LOG_FILES_OFFSET: 6

```

### A.7.3 Others

#### bl\_prism\_layer\_parameters\_v2.py Input

Input file and the result for bl\_prism\_layer\_parameters\_v2.py, a script made at Airbus for determining settings to use in CENTAUR.

```

Reference Reynolds number > 5e6
Reference Length > 1.0
BL thickness multiplier > 71
Desired yplus value > 1.0
P, T, rho : 53528.1521404 240.125 0.776517079908
muT, V : 2.07822394511e-05 103.911197256
a, Ma : 310.655922123 0.334489671227
Cfo : 0.00280051128785
Initial Marching Step : 5.35997436045e-06
Reference BL thickness : 1.20134037141
Number of BL prism layers desired > 35
Stretching Factor : 1.38371178747

```